SLAC-R-712

Study of the Rare Charmless Hadronic B Meson Decays $B^0 \to \phi K^0$ and $B \to K^{*+}\pi^-$.*

A. Anjomshoaa

Stanford Linear Accelerator Center
Stanford University
Stanford, CA 94309

SLAC-Report-712
August 2000

Prepared for the Department of Energy
under contract number DE-AC03-76SF00515

Printed in the United States of America. Available from the National Technical Information Service, U.S. Department of Commerce, 5285 Port Royal Road, Springfield, VA 22161.

*Ph.D. thesis, The University of Edinburgh, UK

Study of the Rare Charmless Hadronic B Meson Decays $B^0 \to \phi K^0$ and $B^0 \to K^{*+}\pi^-$

Ali Anjomshoaa

School of Physics
The University of Edinburgh

Thesis submitted for the degree of Doctor of Philosophy

August 2002

Abstract

This thesis describes the analyses of the rare charmless hadronic B meson decays $B^0 \to \phi K^0$ and $B^0 \to K^{*+}\pi^-$, using 20.58 fb^{-1} of e^+e^- data taken at the $\Upsilon(4S)$ resonance. The data were taken with the *BABAR* detector during its first run at the PEP-II asymmetric e^+e^- collider. Measurements of these modes using a counting technique are presented with the branching fractions $\mathcal{B}(B^0 \to \phi K^0) = (9.3 \pm 3.4(\text{stat.}) \pm 1.1(\text{syst.})) \times 10^{-6}$ with a significance of 4.9σ, and $\mathcal{B}(B^0 \to K^{*+}\pi^-) = (20.8 \pm 9.3(\text{stat.}) \pm 2.1(\text{syst.})) \times 10^{-6}$ with a significance of 3.0σ. For the latter, an upper limit of $\mathcal{B}(B^0 \to K^{*+}\pi^-) < 38.9 \times 10^{-6}$ was calculated at 90 % confidence limit. The branching fraction of a calibration mode was measured using the same method, $\mathcal{B}(B^0 \to D^-\pi^+) = (3.59 \pm 0.29(\text{stat.}) \pm 0.35(\text{syst.})) \times 10^{-3}$.

Declaration

This work represents the effort of many members of the *BABAR* collaboration at the Stanford Linear Accelerator Center in California, USA. The analyses and final results presented in this thesis, however, are entirely my own work, which was undertaken while I was a member of the Charmless Hadronic B Decays Analysis Working Group. The writing of this thesis is also entirely my own work.

Ali Anjomshoaa

Acknowledgements

It has been with the perpetual support of my family that I have been able to successfully undertake adventure after adventure. Thus it has been with the successful completion of this endeavour. Most of all, I thank my mother and father for their continued support and optimism. It is they who continue to inspire me, and who have taught me never to give up and to believe in myself. I also thank my sister and brother-in-law, who have taught me much and whose personal values I hold so dear.

I thank both my supervisor, Dr. Steve Playfer, and my teacher Alan Walker, for accepting me for this Ph.D. and giving me the opportunity to undertake my research as part of the prestigious *BABAR* collaboration. I should also acknowledge the help and support of the rest of the Particle Physics Experiments group, especially, Dr. Roland Bernet, Dr. Francesca Di Lodovico, and James Swain. I am most grateful to my dear friend and mentor, Dr. Roberto Sacco, for his continued friendship, tutoring and discussions, and his remarkable patience and wisdom.

It was, of course, the High Energy Physics group at University College London, with whom I undertook part of my M.Res. degree, whose members inspired me to study particle physics. I am indebted to my supervisor there, Dr. Jenny Thomas, who continued to give me her support while I was working at Edinburgh University. Jenny once wrote to me, "Don't be too introspective, just have a good time and do some work.". She also wrote, "Keep your chin up!". I tried my best Jenny.

This acknowledgement would not be nearly complete without a mention of the members of the Three-Body Charmless Hadronic B Decays Working Group, and the wider Charmless Hadronic B Decays Working Group, to whom I am extremely grateful for their teachings, discussions, reviewing, and company. I am indebted to my friend and mentor, Dr. Paul Harrison, who took me under his wing and allowed me the privilege to work with the group from Queen Mary College, University of London. Working with Paul was inspirational and I look forward to his continued friendship. I should also like to acknowledge the help of my friend and mentor, Dr. John Back, whose

company I enjoyed enormously during my stay at the SLAC.

I received my studentship from the PPARC, to whom I am most grateful for their continued support throughout this Ph.D. and my placements at the SLAC in California. In addition, PPARC funded me in order to attend two extremely educational summer schools, for which I am also thankful.

I thank the SLAC who hosted me as a member of the *BABAR* collaboration, and for making me feel welcome and making my stay most comfortable. The administrative staff at the SLAC were some of the most helpful and caring that I have had the pleasure of meeting.

I should like to express my appreciation to the *BABAR* group at RAL, who hosted my short visit in the summer of 1999.

I thank my peers at the SLAC for their friendship. In particular, I would like to thank Dr. Nicole Chevalier for her patience in helping me with my work, and would like to wish her every success.

This Ph.D. would not have been the same valuable learning experience if it had not been for the RAL and NATO ASI summer schools that I attended. I'd like to thank the organisers, the tutors, and my peers, for the stimulating events of both.

I am extremely grateful to all of the friends whom I met during this Ph.D. while at both Edinburgh and Stanford Universities. They include my friends both inside and outside the universities. My friends were my allies in this venture. I cannot thank them enough for their continued support and friendship. They are the spice of my life.

Contents

List of Figures

List of Tables

Chapter 1

Introduction

The study of the phenomenon of CP violation is currently one of the most active areas in experimental particle physics. Since its initial discovery in the 1960s, it has been a subject of intrigue. CP violation has been postulated as one of the phenomena that is required in order to explain the observed matter dominant universe.

One of the difficulties in the observation of CP violation is the relatively small size of this effect. According to the Standard Model (SM) of particle physics, CP violation only occurs in interactions involving the weak force. Until recently, CP violation was only observed in the neutral K meson system. It has been predicted, however, that CP violation also occurs in the B meson system, mechanisms for the generation of which exist in the SM.

The number of B mesons required in order to observe CP violation in the B meson system, is of the order $\mathcal{O}(10^7)$. With the advent of B meson production experiments known as *B-factories*, which are dedicated to producing large quantities of B mesons, it has become possible to study and observe CP violation in B meson decays.

The initial goal of the *BABAR* experiment at the PEP-II e^+e^- collider was to study and observe one type of CP violation in the neutral B meson system. This CP violation effect arises as a result of the interference between the decays of neutral B mesons

with and without mixing, to a final state that is common to both the B^0 and $\bar{B}^0$ mesons. The so-called *Golden Mode* for the measurement of this effect is the decay $B^0 \to J/\psi K^0_S$. This goal has now been achieved, and measurements of this effect are being refined by the *BABAR* [1] and Belle [2] experiments using larger data-sets.

Other types of CP violation in the B meson system are now being studied at the *BABAR* experiment. These studies involve the measurement of rare B meson decays with branching fractions that are of the order $\mathcal{O}(10^{-5})$. The success of the PEP-II e^+e^- collider in achieving record high luminosities, and of the *BABAR* detector at highly efficient data acquisition, has resulted in the availability of abundant data from B meson events for these measurements.

This thesis presents the study of two rare charmless hadronic B meson decays at the *BABAR* experiment, which are thought to involve two different types of CP violation effects. The first of these, the decay $B^0 \to \phi K^0_S$, was observed by the *BABAR* experiment in 2001, during the studies presented here. Evidence for the second, the decay $B^0 \to K^{*+}\pi^-$, is presented in this thesis, and confirms the results previously found by the CLEO and Belle experiments. The data used for these studies, were taken by the *BABAR* detector during the first year of the experiment, between October 1999 and October 2000. More data is required in order to allow studies of the possible CP violation effects in these decays.

The phenomenon of CP violation is introduced in Chapter 2, with a brief explanation of the three types of CP violation that can occur in the K and B meson systems. The use of the two rare charmless hadronic modes presented here, for the study of CP violation effects, is also motivated. Chapter 3 describes the *BABAR* experiment and its sub-detectors. Data acquisition and the preparation of data are described in Chapter 4, along with a brief introduction to the *BABAR* software environment. Data analysis techniques for the reconstruction and selection of the two modes studied are detailed in Chapter 5. The final results of the analyses are given in Chapter 6, with a description of the treatment of systematic errors. Finally, Chapter 7 presents conclusions drawn from the results obtained and a comparison with other results. Charge conjugate decay modes are implied throughout this thesis.

Chapter 2

Introduction to CP Violation

2.1 Introduction

The operations of charge-conjugation (C), parity-inversion (P), and time-reversal (T), are three discrete symmetries of the quantum field theories of *quantum electro-dynamics* (QED) and *quantum chromo-dynamics* (QCD). The operations P and T are space-time symmetries and result in the transformations $\boldsymbol{P}(t, \vec{x}) \rightarrow (t, -\vec{x})$ and $\boldsymbol{T}(t, \vec{x}) \rightarrow (-t, \vec{x})$, respectively. Thus, the operations P and T cause the reversal of the handedness and the interchanging of the forward and backward light-cones, respectively. The charge-conjugation operation C, replaces a particle q with its antiparticle $\bar{q}$. The joint operation CP, therefore, results in the replacement of q with $\bar{q}$, and the reversing of the momentum and helicity of that particle.

While the C, P, and T symmetries are all individually conserved in strong and electromagnetic processes, the C and P operations are both maximally violated in weak interactions. The combined operation CPT is invariant for all local quantum field theories, so that any violation of the operation CP would signify a violation of the T symmetry.

In 1967, Sakharov postulated that one of the requirements for the matter-antimatter asymmetry that is observed in the universe, is the process of CP violation [3]. Within

the Standard Model (SM) of particle physics containing three fermion generations, it is possible to produce CP violation in a number of charged-current weak decays. This phenomenon was first observed in the decays of neutral K mesons by Christenson *et al.* in 1964 [4].

The first observation of CP violation in the decays of neutral B mesons was by the *BABAR* experiment in 2002 [5]. This observation was manifested in a time-dependent decay rate asymmetry between the B^0 meson and its antiparticle the $\bar{B}^0$ meson, in decays to charmonium final states common to both. Although the SM predicts that the effect of CP violation in the B meson sector is much larger than that in the kaon sector [6], the overall effect attributed to this mechanism is still too small to explain the baryon asymmetry of the universe [7, 8].

With the advent of B-factories, which are providing large numbers of B meson decays, the prospects are good for the precise measurement of time-dependent CP asymmetries, and for the observation of other CP violating effects. This chapter introduces the phenomenon of CP violation, before motivating the use of rare charmless hadronic B meson decays for its study.

2.2 The Cabibbo-Kobayashi-Maskawa (CKM) Matrix and the Unitarity Triangle

The Cabibbo-Kobayashi-Maskawa (CKM) matrix [9] is shown in Equation 2.1. Its elements, represented by $V_{qq'}$, give the couplings for the flavour changing processes $q \to q'$ for the three quark generations, where q represents the up type quarks u, c, and t, and q' represents the down type quarks d, s, and b.

$$V_{qq'} = \begin{pmatrix} V_{ud} & V_{us} & V_{ub} \\ V_{cd} & V_{cs} & V_{cb} \\ V_{td} & V_{ts} & V_{tb} \end{pmatrix} . \tag{2.1}$$

The unitarity of the CKM matrix, given by $VV^\dagger = \mathbf{1}$, leads to a number of relations

between its elements [10]. Three of these relations, shown in Equations 2.2, 2.3, and 2.4, are very useful in describing the predictions of the SM.

$$V_{ud}V_{us}^* + V_{cd}V_{cs}^* + V_{td}V_{ts}^* = 0\,. \tag{2.2}$$

$$V_{us}V_{ub}^* + V_{cs}V_{cb}^* + V_{ts}V_{tb}^* = 0\,. \tag{2.3}$$

$$V_{ud}V_{ub}^* + V_{cd}V_{cb}^* + V_{td}V_{tb}^* = 0\,. \tag{2.4}$$

An excellent approximation of the CKM matrix is given by the Wolfenstein parametrisation [11] in terms of the four real parameters, λ, A, ρ, and η. This parametrisation of the CKM matrix is accurate to order $\mathcal{O}(\lambda^3)$. It is given by,

$$V = \begin{pmatrix} 1-\frac{\lambda^2}{2} & \lambda & A\lambda^3(\rho - i\eta) \\ -\lambda & 1-\frac{\lambda^2}{2} & A\lambda^2 \\ A\lambda^3(1-\rho-i\eta) & -A\lambda^2 & 1 \end{pmatrix} + \mathcal{O}(\lambda^4)\,, \tag{2.5}$$

where $\lambda = \sin\theta_{\mathrm{C}} \approx 0.22$, and θ_{C} is the Cabibbo mixing angle [12].

A comparison of Equations 2.1 and 2.5 shows that,

$$V_{us} = \lambda\,, \tag{2.6}$$

$$V_{cb} = A\lambda^2\,. \tag{2.7}$$

Using Equations 2.6 and 2.7, the parameters λ and A can be experimentally determined by the measurement of the branching fractions for the semileptonic decays of K and B mesons, respectively. In these decays, the quark flavour changing processes $s \to u$ and $b \to c$ take place. Both flavour changing processes are charged-current weak interactions involving the exchange of a W boson, and are described by the *tree level* processes shown in Figure 2.1.

The relation in Equation 2.4 is represented in a complex plane by the *Unitarity Triangle* shown in Figure 2.2 [13]. Of the four parameters of the Wolfenstein parametrisation, ρ and η define the real axis and the complex axis of this complex plane, respectively. The Unitarity Triangle is by convention normalised to $|V_{cd}V_{cb}^*| = |A\lambda^3|$ on the

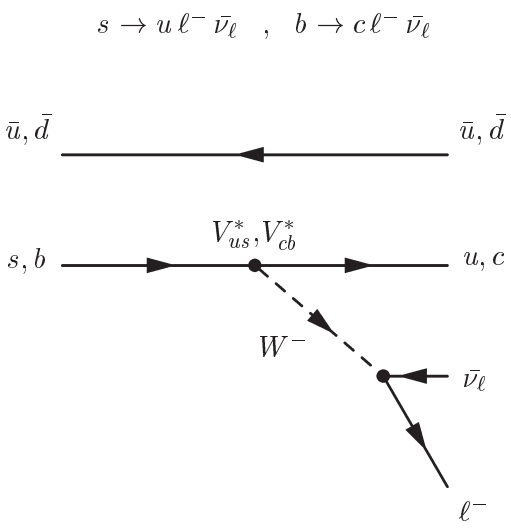

Figure 2.1: *Tree level Feynman diagram for the semileptonic decays* $s \to u\,\ell^-\,\bar{\nu}_\ell$ *and* $b \to c\,\ell^-\,\bar{\nu}_\ell$.

real axis. The area represented by this triangle is a measure of the size of the effect of CP violation, and if non-zero, would lead to the conclusion that there exist processes that are not invariant under the combined charge-conjugation and parity-inversion operations CP [14].

The accuracy of the Wolfenstein parametrisation can be improved to order $\mathcal{O}(\lambda^6)$ [16]. This results in,

$$V_{us} = \lambda\,, \tag{2.8}$$

$$V_{cb} = A\lambda^2\,, \tag{2.9}$$

$$V_{ub} = A\lambda^3(\rho - i\eta)\,, \tag{2.10}$$

$$V_{td} = A\lambda^3(1 - \bar{\rho} - i\bar{\eta})\,, \tag{2.11}$$

$$\text{Im}\; V_{cd} = -A^2\lambda^5\eta\,, \tag{2.12}$$

$$\text{Im}\; V_{ts} = -A\lambda^4\eta\,, \tag{2.13}$$

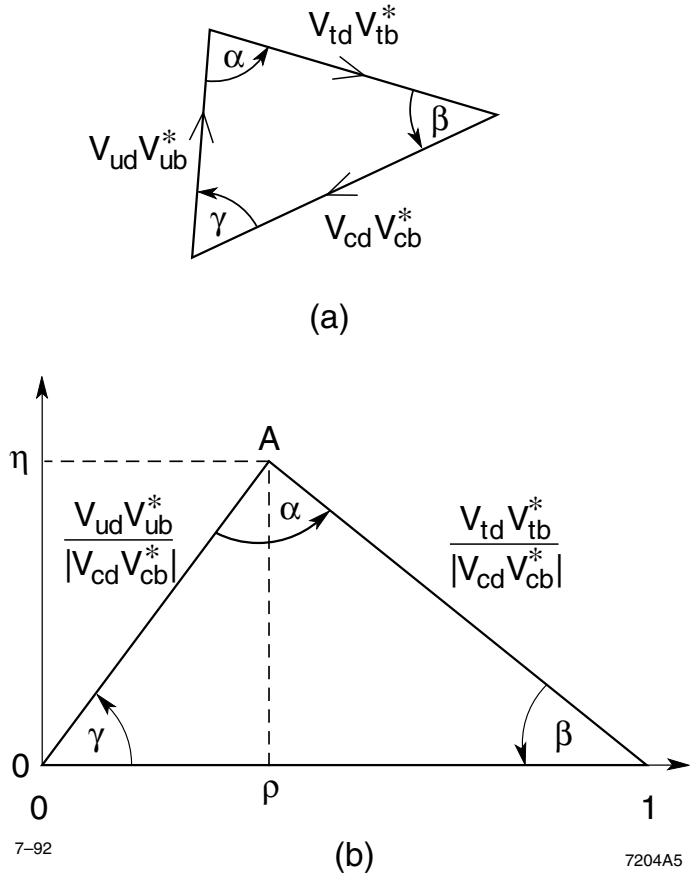

Figure 2.2: *(a) The Unitarity Triangle representing the relationship expressed in Equation 2.4, (b) normalised to $|V_{cd}V_{cb}^*|$ on the real axis. (From [15])*

where,

$$\bar{\rho} = \rho(1 - \lambda^2/2)\,, \tag{2.14}$$

$$\bar{\eta} = \eta(1 - \lambda^2/2)\,. \tag{2.15}$$

The Unitarity Triangle is then rescaled in the $\bar{\rho}$-$\bar{\eta}$ plane. The three angles of the Unitarity Triangle, α, β, and γ, are defined by Equations 2.16, 2.17, and 2.18, respectively.

Table 2.1: *The measured values of a subset of the parameters that are used to constrain the apex of the Unitarity Triangle in the $\bar{\rho}$-$\bar{\eta}$ plane [17]. Also shown are the experimental observations used for these measurements. (CL - confidence limit)*

Parameter	Experimental Observation	Measurement
$\lvert V_{ub}\rvert$	semileptonic B decays, $b \to u\,\ell^-\,\bar{\nu}_\ell$	$(3.6 \pm 0.7) \times 10^{-3}$
$\lvert\epsilon_K\rvert$	CP violation in $K_L^0 \to \pi\pi$	$(2.282 \pm 0.017) \times 10^{-3}$
Δm_{B_s}	$B_s^0 - \bar{B}_s^0$ mixing	> 13.1 ps^{-1} at 95 % CL
Δm_{B_d}	$B_d^0 - \bar{B}_d^0$ mixing	0.489 ± 0.008 ps^{-1}
$\sin 2\beta$	CP violation in $B^0 \to J/\psi K_S^0$	0.78 ± 0.08

$$\alpha \equiv \arg\left[-\frac{V_{td}V_{tb}^*}{V_{ud}V_{ub}^*}\right], \tag{2.16}$$

$$\beta \equiv \arg\left[-\frac{V_{cd}V_{cb}^*}{V_{td}V_{tb}^*}\right], \tag{2.17}$$

$$\gamma \equiv \arg\left[-\frac{V_{ud}V_{ub}^*}{V_{cd}V_{cb}^*}\right] \equiv \pi - \alpha - \beta\,. \tag{2.18}$$

These angles, which may be determined from studies of K and B mesons, help to impose constraints on the Wolfenstein parameters $\bar{\rho}$ and $\bar{\eta}$. A subset of the parameters that are used to constrain the apex of the normalised Unitarity Triangle is listed in Table 2.1 and shown as limits on the $\bar{\rho}$-$\bar{\eta}$ plane in Figure 2.3.

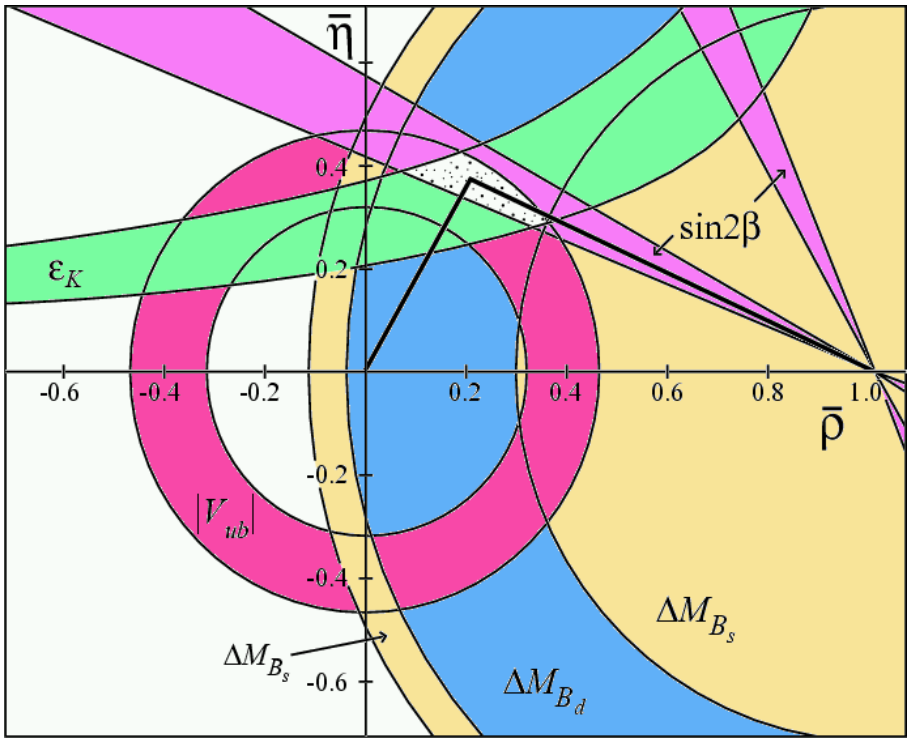

Figure 2.3: *The complex $\bar{\rho}$-$\bar{\eta}$ plane showing the constraints listed in Table 2.1. The dotted region shows these constraints imposed on the position of the apex of the normalised Unitarity Triangle, which is rescaled in the $\bar{\rho}$-$\bar{\eta}$ plane. (From [17])*

2.3 CP Violation in Neutral K Meson Decays

Neutral K mesons are produced in strong interactions. Their quark contents and CP transformations are given in Equations 2.19 and 2.20, respectively.

$$K^0 = (d\bar{s}) \quad , \qquad \bar{K^0} = (s\bar{d})\,. \tag{2.19}$$

$$\boldsymbol{CP}|K^0\rangle = (-1)|\bar{K^0}\rangle \quad , \qquad \boldsymbol{CP}|\bar{K^0}\rangle = (-1)|K^0\rangle\,. \tag{2.20}$$

The $|K^0\rangle$ and $|\bar{K^0}\rangle$ states are the *flavour* eigenstates of the neutral kaon system. They are linear combinations of the two CP eigenstates $|K_1\rangle$ and $|K_2\rangle$, and are given by,

$$|K^0\rangle = \frac{1}{\sqrt{2}}(|K_1\rangle + |K_2\rangle)\,, \tag{2.21}$$

$$|\bar{K^0}\rangle = \frac{1}{\sqrt{2}}(|K_2\rangle - |K_1\rangle)\,. \tag{2.22}$$

In the absence of CP violation, the CP eigenstates would decay to the final states,

$$K_1 \to \pi\pi \quad (\boldsymbol{CP} = +1)\,, \quad K_2 \to \pi\pi\pi \quad (\boldsymbol{CP} = -1)\,. \tag{2.23}$$

The CP transformations of these CP eigenstates are given by,

$$\boldsymbol{CP}|K_1\rangle = (+1)|K_1\rangle\,, \quad \boldsymbol{CP}|K_2\rangle = (-1)|K_2\rangle\,. \tag{2.24}$$

The kinetic energy released from the decay $K_1 \to \pi\pi$ is much larger than that released from the decay $K_2 \to \pi\pi\pi$, so that the former has a much shorter lifetime. Thus, in the absence of CP violation, the states $|K_1\rangle$ and $|K_2\rangle$ could be referred to as $|K_S\rangle$ and $|K_L\rangle$, respectively, where the S and L subscripts refer to the *short* and the *long* lifetimes that they possess. The respective lifetimes of the $|K_S\rangle$ and $|K_L\rangle$ states are, $\tau_{K_S} = 89.35 \pm 0.08$ ps, and $\tau_{K_L} = 51.7 \pm 0.4$ ns [17].

Due to the presence of CP violation, however, the observable decay eigenstates that are represented by $|K_S\rangle$ and $|K_L\rangle$, are admixtures of the two CP eigenstates $|K_1\rangle$ and $|K_2\rangle$. A small fraction of K_L particles actually decay to a two pion final state, while the same fraction of K_S particles should decay to a three pion final state, although the latter is suppressed by the differential lifetime of the $|K_S\rangle$ and $|K_L\rangle$ states. The decay eigenstates, therefore, are properly represented by,

$$|K_S\rangle = \frac{1}{\sqrt{1+|\bar{\epsilon}|^2}}(|K_1\rangle + \bar{\epsilon}|K_2\rangle)\,, \tag{2.25}$$

$$|K_L\rangle = \frac{1}{\sqrt{1+|\bar{\epsilon}|^2}}(|K_2\rangle + \bar{\epsilon}|K_1\rangle)\,, \tag{2.26}$$

where the quantity $\bar{\epsilon}$ parametrises the small fraction of CP violating decays.

The eigenstates $|K_S\rangle$ and $|K_L\rangle$ represent the observed mesons K_S^0 and K_L^0, respectively. In 1964, Christenson *et al.* discovered that a small fraction of K_L^0 mesons decay

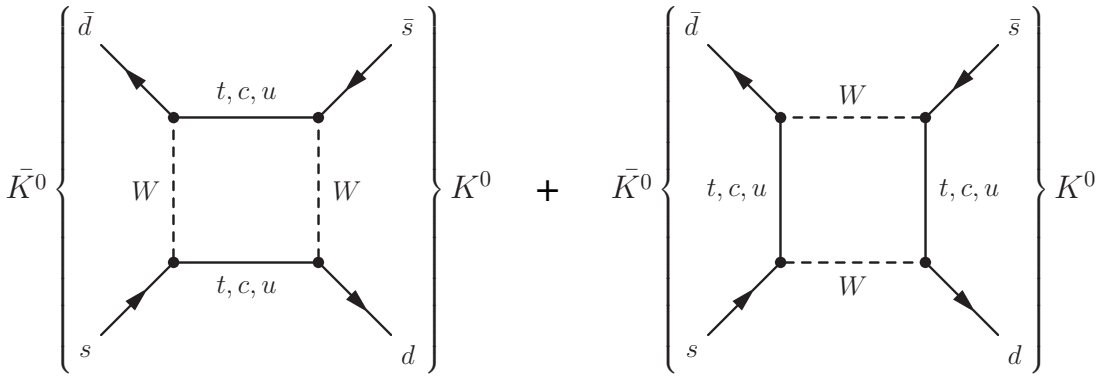

Figure 2.4: *The two Feynman box diagrams that contribute to $K^0 - \bar{K}^0$ mixing.*

to a two pion final state [4], showing for the first time that CP violation occurs in the neutral kaon system.

There are, in fact, three different types of CP violation that occur in the neutral kaon system. The first of these is *indirect* CP violation. This effect occurs in the *mixing* between the K^0 meson and its antiparticle the $\bar{K}^0$ meson. This mixing is manifested in weak interactions via the two Feynman *box diagrams* shown in Figure 2.4. The flavour eigenstates $|K^0\rangle$ and $|\bar{K}^0\rangle$ decay via the observable decay eigenstates $|K_S\rangle$ and $|K_L\rangle$, each of which is an admixture of the two CP eigenstates $|K_1\rangle$ and $|K_2\rangle$. This results in a small fraction of the K_S^0 and K_L^0 mesons decaying to CP violating final states.

The second type of CP violation is known as *direct* CP violation, or CP *violation in the decay amplitude*. This phenomenon is evident when the amplitude $A_f = \langle f|H|K\rangle$ for a process involving a K meson decaying to a final state f, is not equal to the amplitude $\bar{A}_{\bar{f}} = \langle \bar{f}|H|\bar{K}\rangle$ for its conjugate process, where a $\bar{K}$ meson decays to the charge conjugate final state $\bar{f}$, so that,

$$\left|\frac{A_f}{\bar{A}_{\bar{f}}}\right| \neq 1\,. \tag{2.27}$$

Finally, there is a CP violating effect in the interference between decays with and without mixing. In the neutral kaon system, measurements of the effects of indirect

and direct CP violation, intrinsically have a contribution from CP violation in the interference between decays with and without mixing.

The parameter $\bar{\epsilon}$ in Equations 2.25 and 2.26 is related to the parameter ϵ, which is measured in experiments. ϵ parametrises the effect of indirect CP violation and includes a contribution from CP violation in the interference between decays with and without mixing.

Another parameter ϵ', measures the size of a combination of the effects of direct CP violation and CP violation in the interference between decays with and without mixing. The real part of ϵ', Re (ϵ'), depends entirely on direct CP violation. Having measured ϵ, ϵ' can be determined from the two amplitude ratios η_{+-} and η_{00}, where,

$$\eta_{+-} = \frac{A(K_L^0 \to \pi^+\pi^-)}{A(K_S^0 \to \pi^+\pi^-)} = \epsilon + \epsilon' , \tag{2.28}$$

$$\eta_{00} = \frac{A(K_L^0 \to \pi^0\pi^0)}{A(K_S^0 \to \pi^0\pi^0)} = \epsilon - 2\epsilon' . \tag{2.29}$$

The effect of direct CP violation in the neutral K meson system is experimentally determined by the measurement of a double ratio R. This ratio is related to the ratio Re (ϵ'/ϵ) by,

$$R = \frac{\Gamma(K_L^0 \to \pi^0\pi^0)}{\Gamma(K_S^0 \to \pi^0\pi^0)} \Big/ \frac{\Gamma(K_L^0 \to \pi^+\pi^-)}{\Gamma(K_S^0 \to \pi^+\pi^-)} \approx 1 - 6 \text{ Re } (\epsilon'/\epsilon) . \tag{2.30}$$

A non-zero measurement of Re $(\epsilon'/\epsilon) = (15.3 \pm 2.6) \times 10^{-4}$ was made in 2001 [18], proving that there is a component of direct CP violation in the decays of neutral K mesons.

2.4 CP Violation in B Meson Decays

The SM predicts CP violating effects in the B meson sector that are analogous to those observed in the K meson sector. In the neutral B meson sector, there is an expected CP violating effect as a result of the same mixing effect observed in neutral

kaons. Asymmetries in the direct decays of B and $\bar{B}$ mesons to charge conjugate final states are also expected. CP violating effects in the interference between decays with and without mixing are present, and are the cause for the time-dependent decay rate asymmetries observed in neutral B meson decays by the *BABAR* experiment [5, 19] and the Belle experiment [20], where the final state is a CP eigenstate common to both the B^0 and $\bar{B}^0$ mesons.

2.4.1 Direct CP Violation in B Meson Decays

As discussed in Section 2.3 and shown in Equation 2.27, direct CP violation will be manifest in an asymmetry between the number of decays of B mesons to a final state f, and the number of decays of $\bar{B}$ mesons to the charge conjugate final state $\bar{f}$. This asymmetry is given by,

$$a_f = \frac{\Gamma(B \to f) - \Gamma(\bar{B} \to \bar{f})}{\Gamma(B \to f) + \Gamma(\bar{B} \to \bar{f})}\,. \tag{2.31}$$

This effect is predicted in the decays of both neutral and charged B mesons, although the need to establish the flavour of the reconstructed B meson from its final state, means that charged B mesons provide a more favourable environment for its study [6].

If A_f is the amplitude for the decay of B mesons to a final state f, and $\bar{A}_{\bar{f}}$ is the amplitude for the decay of $\bar{B}$ mesons to the charge conjugate final state $\bar{f}$, then,

$$\left|\frac{A_f}{\bar{A}_{\bar{f}}}\right| = \left|\frac{\sum_i A_i e^{i(\delta_i+\phi_i)}}{\sum_i A_i e^{i(\delta_i-\phi_i)}}\right|, \tag{2.32}$$

where A_i are the magnitudes, $e^{i\phi_i}$ represent the weak phase terms, and $e^{i\delta_i}$ represent the strong phase terms, of the contributions to the amplitude for the decays. Direct CP violation would occur as a result of the interference between two different amplitudes contributing to a decay, which have different weak phases ϕ_i, and strong phases δ_i, and is implied by,

$$\left|\frac{A_f}{\bar{A}_{\bar{f}}}\right| \neq 1\,. \tag{2.33}$$

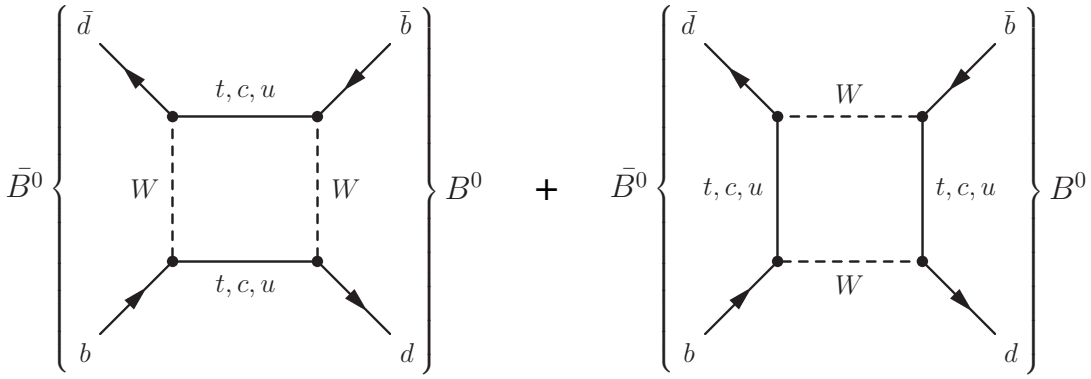

Figure 2.5: *The two Feynman box diagrams that contribute to $B^0 - \bar{B}^0$ mixing.*

Since charged B mesons cannot mix due to charge conservation, CP asymmetries in charged B meson decays are solely due to direct CP violation.

2.4.2 CP Violation in $B^0 - \bar{B}^0$ Mixing

Mixing in the neutral B meson system is directly analogous to that in the neutral K meson system. It is represented by the sum of the two Feynman box diagrams shown in Figure 2.5. The contribution of the top quark to these mixing diagrams is dominant due to its high mass relative to the other up type quarks. The flavour eigenstates of the neutral B_d meson, $|B^0\rangle$ and $|\bar{B}^0\rangle$, have definite quark contents given by,

$$B^0 = (d\bar{b})\,, \quad \bar{B}^0 = (b\bar{d})\,. \tag{2.34}$$

Since its observation in 1987 [21, 22], $B^0 - \bar{B}^0$ mixing has been comprehensively studied [17]. The $B^0 - \bar{B}^0$ oscillation frequency is the difference in mass, Δm_{B_d}, between the two neutral B_d meson mass eigenstates. The probability for $B^0 - \bar{B}^0$ mixing is a function of Δm_{B_d} and the time difference Δt, between the decays of two coherently produced neutral B_d mesons. This probability is given by [5],

$$\text{Prob}(B^0\bar{B}^0 \to B^0B^0 \;\text{ or }\; \bar{B}^0\bar{B}^0) = \frac{\Gamma}{4}e^{-\Gamma|\Delta t|}(1 \mp \cos(\Delta m_{B_d}\Delta t))\,, \tag{2.35}$$

where $\Gamma = 1/\tau_{B^0}$, and $\tau_{B^0} = 1.542 \pm 0.016$ ps [17] is the B^0 lifetime.

Measurement of the $B^0 - \bar{B}^0$ oscillation frequency Δm_{B_d}, is an integral part of the measurement of the CP violation parameter $\sin 2\beta$, which is described in Section 2.5. The latest measurement made by the *BABAR* experiment is $\Delta m_{B_d} = 0.493 \pm 0.012(\text{stat.}) \pm 0.009(\text{syst.})$ ps^{-1} [23]. The value presented by the Particle Data Group is $\Delta m_{B_d} = 0.489 \pm 0.008(\text{total})$ ps^{-1} [17].

The Hamiltonian used to describe $B^0 - \bar{B}^0$ mixing in terms of the mass M and the width Γ of the neutral B meson, is given by,

$$\langle B^0|H|\bar{B}^0\rangle = M_{B^0\bar{B}^0} - \frac{i}{2}\Gamma_{B^0\bar{B}^0}\,, \tag{2.36}$$

where M and Γ are both 2×2 matrices. As a result of CPT invariance, $H_{11} = H_{22} = M - i\Gamma/2$, so that,

$$H \equiv \begin{pmatrix} M - i\Gamma/2 & M_{12} - i\Gamma_{12}/2 \\ M^*_{12} - i\Gamma^*_{12}/2 & M - i\Gamma/2 \end{pmatrix}. \tag{2.37}$$

In order for mixing to take place, the off-diagonal terms in Equation 2.37 must be non-zero. In addition, if CP is violated then the off-diagonal terms are not equal, so that $M^*_{12} \neq M_{12}$ or $\Gamma^*_{12} \neq \Gamma_{12}$, or both.

As in the neutral kaon system, the flavour eigenstates $|B^0\rangle$ and $|\bar{B}^0\rangle$ are a linear combination of the two CP eigenstates $|B_1\rangle$ and $|B_2\rangle$. The observable neutral B meson mass (or decay) eigenstates are an admixture of these CP eigenstates. These mass eigenstates are given by [24],

$$|B_L\rangle \;=\; p|B^0\rangle + q|\bar{B}^0\rangle \;=\; \frac{1}{\sqrt{1+|\tilde{\epsilon}|^2}}(|B_2\rangle + \tilde{\epsilon}|B_1\rangle)\,, \tag{2.38}$$

$$|B_H\rangle \;=\; p|B^0\rangle - q|\bar{B}^0\rangle \;=\; \frac{1}{\sqrt{1+|\tilde{\epsilon}|^2}}(|B_1\rangle + \tilde{\epsilon}|B_2\rangle)\,, \tag{2.39}$$

where $|B_L\rangle$ and $|B_H\rangle$ are the *light* and *heavy* neutral B meson mass eigenstates, respectively, and p and q are complex coefficients that obey,

$$|p|^2 + |q|^2 = 1\,. \tag{2.40}$$

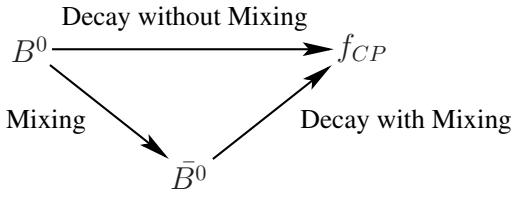

Figure 2.6: *B^0 meson decaying to a final CP eigenstate, f_{CP}, with and without mixing.*

The quantity $\tilde{\epsilon}$ in Equations 2.38 and 2.39 represents the amount of CP violation in mixing. If CP is conserved, $\tilde{\epsilon}$ is zero, which makes the mass eigenstates identical to the CP eigenstates. The relation [6],

$$\left|\frac{q}{p}\right|^2 = \left|\frac{M_{12}^* - i\Gamma_{12}^*/2}{M_{12} - i\Gamma_{12}/2}\right|, \tag{2.41}$$

implies CP violation if,

$$\left|\frac{q}{p}\right| \neq 1\,. \tag{2.42}$$

2.4.3 *CP* Violation From the Interference Between *B* Meson Decays With and Without Mixing

This type of CP violation occurs in neutral B meson decays, where the final state is a CP eigenstate that is common to both the B^0 and $\bar{B}^0$ mesons. In these decays, therefore, it is not possible to distinguish the flavour of the neutral B meson from the final CP eigenstate alone. Figure 2.6 shows that a B^0 meson can decay to a final CP eigenstate after oscillating to a $\bar{B}^0$ meson, *decay with mixing*, or directly, *without mixing*. The interference between these two processes results in CP violation known as CP violation from the interference between decays with and without mixing.

At the $\Upsilon(4S)$ resonance, $B\bar{B}$ meson pairs are produced coherently. The flavour of one of the neutral B mesons may be determined from its final state decay products at

some time t_0. This process is known as *tagging* the flavour of that B meson, which is then known as the *tagging B meson*. The other neutral B meson, the *tagged B meson*, then needs to be fully reconstructed into a final CP eigenstate at some time t later, or earlier. An asymmetry between the number of decays of the two time evolved charge conjugate states, as a function of the time difference $\Delta t = |t - t_0|$, would signify CP violation as a result of interference between decays with and without mixing.

The quantity of interest for the study of this effect is the complex parameter λ, which is defined by,

$$\lambda = \frac{q}{p}\frac{\bar{A}_{f_{CP}}}{A_{f_{CP}}}\,. \tag{2.43}$$

The complex coefficients p and q were introduced in Section 2.4.2, and A and $\bar{A}$ were defined in Section 2.4.1. The subscript f_{CP} represents the final CP eigenstate that is common to both the B^0 and $\bar{B^0}$ mesons.

CP violation in this regime is implied by,

$$|\lambda| \neq 1\,, \tag{2.44}$$

if there is direct CP violation, from Equation 2.33, or if there is indirect CP violation, from Equation 2.42. Alternatively,

$$|\lambda| = 1\,, \quad \mathrm{Im}\,(\lambda) \neq 0\,. \tag{2.45}$$

implies the absence of direct and indirect CP violation, in which case there is CP violation due to the interference between decays with and without mixing.

2.5 Measurement of $\sin 2\beta$ with $B^0 \to J/\psi K^0_S$

The Golden Mode for the determination of the angle β of the Unitarity Triangle is the decay $B^0 \to J/\psi K^0_S$, where $J/\psi \to l^+l^-$ and $K^0_S \to \pi\pi$. The CP violation effect

$$B^0 \to J/\psi K_S^0$$

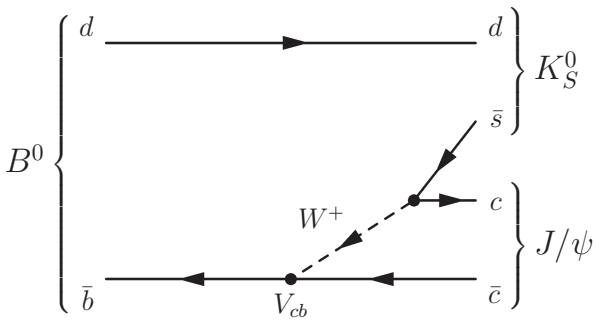

Figure 2.7: *Tree level diagram for the decay* $B^0 \to J/\psi K_S^0$.

studied with this mode is that from the interference between B meson decays with and without mixing. This effect was described in Section 2.4.3, and its measurement by the *BABAR* experiment is described in reference [5].

The amplitude for $B^0 \to J/\psi K_S^0$ has a dominant contribution from the tree level diagram shown in Figure 2.7. Any other contributing processes to this final state are heavily Cabibbo suppressed, so that any interference between different contributions that may result in direct CP violation, is negligible. This effective single contribution means that this is a clean mode for the measurement of CP violation as a result of the interference between decays with and without mixing. This case is true for any neutral B meson decay to a CP eigenstate that has a single contribution to its amplitude.

The time-dependent CP violating asymmetry $a_{CP}(\Delta t)$ is given by [5],

$$a_{CP}(\Delta t) = \frac{\mathrm{f}_+(\Delta t) - \mathrm{f}_-(\Delta t)}{\mathrm{f}_+(\Delta t) + \mathrm{f}_-(\Delta t)}\,, \tag{2.46}$$

where $\mathrm{f}_+(\Delta t)$ and $\mathrm{f}_-(\Delta t)$ are the distributions of the time-dependent decay rate for the final CP eigenstate, when the tagging B meson is a B^0 or a $\bar{B}^0$ meson, respectively. Neglecting time resolution and mistagging rates, a_{CP} is given by [5],

$$a_{CP}(\Delta t) = -\eta_{f_{CP}} \sin 2\beta \sin(\Delta m_{B_d} \Delta t)\,, \tag{2.47}$$

where $\eta_{f_{CP}}$ is the CP eigenvalue of the final CP eigenstate. The mass difference Δm_{B_d} and time difference Δt were introduced in Section 2.4.2.

The flavour of the tagging B meson is determined from the charge of highly energetic electrons, muons, and kaons, or from soft-pions from D^* meson decays. The observed asymmetry is reduced by a *dilution factor* $D = (1 - 2w)$, where w is the mistag fraction. The vertex of the tagging B meson is determined by fitting all of the tracks that were not used in the reconstruction of the tagged B meson to the CP eigenstate, to a common vertex. The uncertainty of the position of this vertex dominates the Δt resolution.

A value of $\sin 2\beta$ that is significantly different from zero would prove the existence of CP violation in the B meson system. The *BABAR* experiment was the first to make this measurement [5] and the value obtained, $\sin 2\beta = 0.59 \pm 0.14(\text{stat.}) \pm 0.05(\text{syst.})$, established the existence of CP violation in the neutral B meson system. This measurement was made using the mode $B^0 \to J/\psi K^0_S$ and other modes including, $B^0 \to \psi(2S)K^0_S$, $B^0 \to J/\psi K^0_L$, $B^0 \to \chi_{c1} K^0_S$, and $B^0 \to J/\psi K^{*0}$ (where $K^{*0} \to K^0_S \pi^0$). The latest result from the *BABAR* experiment is $\sin 2\beta = 0.741 \pm 0.067(\text{stat.}) \pm 0.033(\text{syst.})$ [19].

2.6 *CP* Violation in Rare Charmless Hadronic *B* Meson Decays

Rare charmless hadronic B meson decays with a one-loop Feynman diagram contribution, such as that shown in Figure 2.8 for $B^0 \to \phi K^0_S$, provide a rich environment for the study of CP violation in the B meson system [25]. These one-loop diagrams are commonly known as *penguin* diagrams [25, 26]. They are particularly interesting for the study of direct CP violation effects, which are expected from the interference between penguin and tree level contributions to the same mode, especially if these contributions have comparable amplitudes.

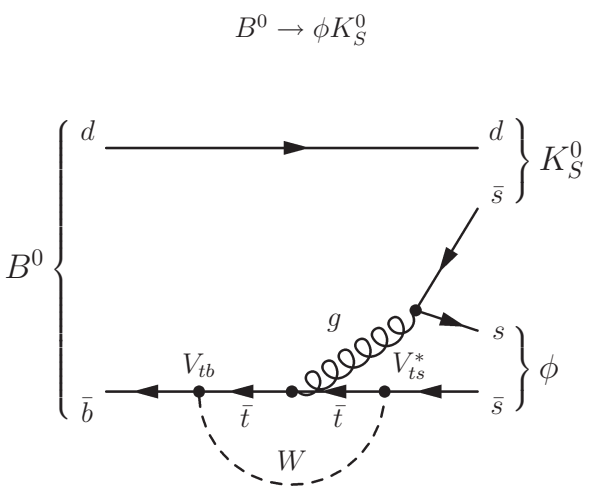

Figure 2.8: *Penguin diagram for the decay* $B^0 \to \phi K_S^0$.

2.6.1 Measurement of $\sin 2\beta$ with $B^0 \to \phi K_S^0$

An alternative mode for the measurement of $\sin 2\beta$ is $B^0 \to \phi K_S^0$ [27], where $\phi \to K^+K^-$ and $K_S^0 \to \pi^+\pi^-$. The only contribution to the amplitude of this CP eigenstate is from the gluonic penguin diagram shown in Figure 2.8 [28, 29]. Having a single contribution to its amplitude, this final state provides an interesting cross-check of the measurement made using the decay $B^0 \to J/\psi K_S^0$, which only has a tree level contribution to its amplitude. Such a comparison may yield an insight into any internal processes of the penguin loop, such as hidden Higgs or supersymmetric processes, which may lead to new physics [30, 31].

The procedure for the measurement of $\sin 2\beta$ using $B^0 \to \phi K_S^0$ is the same as that outlined in Section 2.5 for the Golden Mode $B^0 \to J/\psi K_S^0$ [5].

2.6.2 Direct CP Violation in $B^0 \to K^{*+}\pi^-$

Decays of B mesons to final states that have contributions from both penguin and tree level diagrams, may exhibit direct CP violation as a result of the interference between the respective weak and strong phases of these contributions [32, 33]. Theoretically,

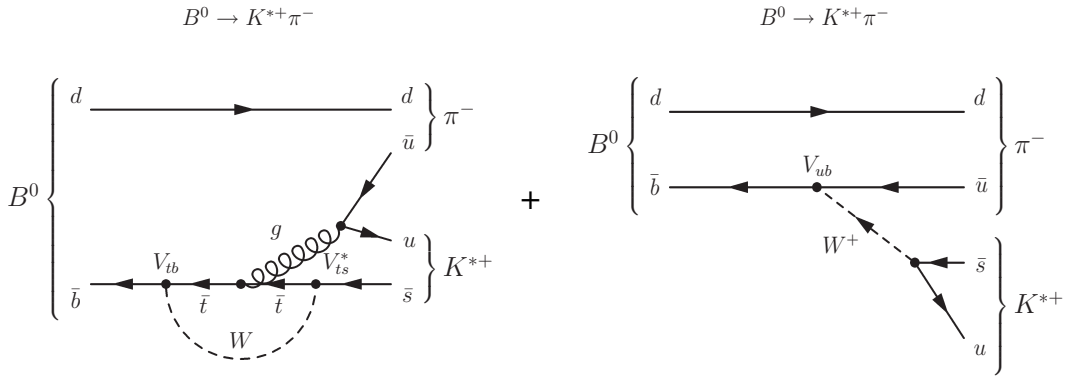

Figure 2.9: *Penguin (left) and tree level (right) diagrams for the decay* $B^0 \to K^{*+}\pi^-$.

these effects are difficult to estimate due to hadronic uncertainties in determining strong phases. Measurements of such modes would contribute to the study of direct CP violation and help in understanding the relative magnitudes of the different contributions.

Recent measurements of the branching fractions of B meson decays to $K\pi$ and $\pi\pi$ final states [34, 35, 36] may indicate considerable gluonic penguin contributions to $B \to K\pi$ decays, and that the penguin and tree level contributions to these modes may be comparable in amplitude. This means that these modes may exhibit large direct CP violation effects as a result of interference between the phases of the penguin and tree level contributions. If this is true, the mode $B^0 \to K^{*+}\pi^-$ may be suitable for the measurement of direct CP violation effects. This mode has contributions from both the penguin and tree level diagrams shown in Figure 2.9. Though model dependent, direct CP violation effects in this mode are predicted to be large [33].

Chapter 3

The *BABAR* Experiment

3.1 The PEP-II Asymmetric e^+e^- Collider

The *BABAR* experiment is based at the PEP-II asymmetric B-factory [37]. PEP-II is an upgrade of the original PEP (Positron-Electron Project) facility at the Stanford Linear Accelerator Center (SLAC). This high luminosity e^+e^- collider stores 9.0 GeV electrons and 3.1 GeV positrons in two storage rings, which are positioned approximately one metre apart and placed one above the other. The SLAC linear accelerator is used as the injector for both beams. Figure 3.1 shows the position of the *BABAR* detector with respect to the PEP-II storage rings and the linear accelerator (linac).

The e^+e^- beams collide head-on at the interaction point (IP) within the *BABAR* detector. The beams are tuned, so that the centre-of-mass energy of the collisions is at the $\Upsilon(4S)$ resonance mass, nominally 10.58 GeV [17]. The $\Upsilon(4S)$ meson is assumed to decay exclusively to equal amounts of $B^0\bar{B}^0$ and B^+B^- meson pairs. The production of B mesons is coherent, resulting in correlated $B\bar{B}$ pairs. In addition to generating no combinatorial backgrounds from unwanted fragmentation products, B meson production at the $\Upsilon(4S)$ resonance gives rise to kinematic constraints on the B meson system, which help in suppressing continuum backgrounds.

The collision events are Lorentz boosted forward in the laboratory frame, in the di-

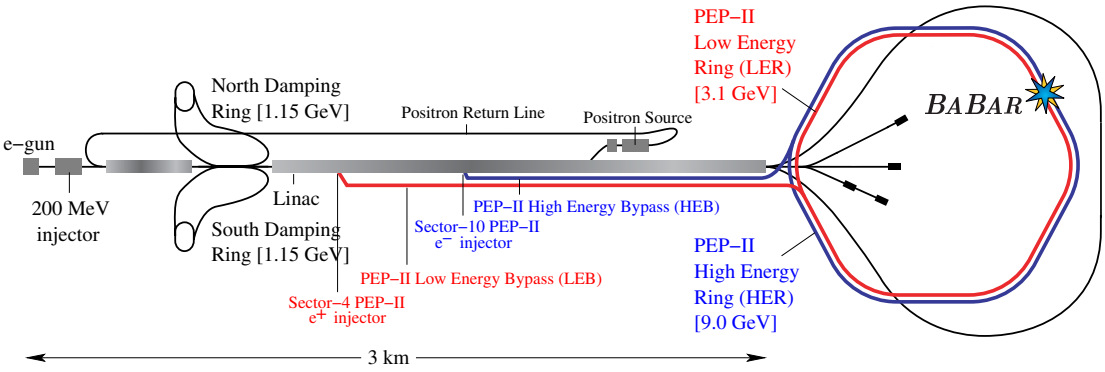

Figure 3.1: *The SLAC linear accelerator (linac), PEP-II storage rings, and the location of the BABAR detector.*

rection of the e^- beam, with a boost factor of $\beta\gamma = 0.56$. Since in the centre-of-mass system the $B\bar{B}$ mesons would be produced essentially at rest, the boost is crucial in order to separate the decay vertices of the B and $\bar{B}$ mesons for the measurement of time-dependent decay rate asymmetries.

Approximately 13% of the recorded data is taken at a centre-of-mass energy that is 40 MeV below the threshold for $B\bar{B}$ production at the $\Upsilon(4S)$ resonance. This is to provide real data for studies of continuum backgrounds from $u\bar{u}$, $d\bar{d}$, $c\bar{c}$, and $s\bar{s}$ production. These continuum backgrounds are the major contributors to the background in studies of rare charmless hadronic B meson decays.

The absolute luminosity of PEP-II is calculated by measuring the production rate of lepton pairs. This is done by selecting e^+e^- and $\mu^+\mu^-$ pair events, and then normalising the number observed to the selection efficiencies obtained for these events from Monte Carlo data. To ensure that data is taken with a large $e^+e^- \to \Upsilon(4S)$ cross-section, the centre-of-mass energy is monitored by observing the rate of hadronic $B\bar{B}$ events and normalising this to the measured luminosity and the Monte Carlo efficiency for the selection of these events.

With a peak instantaneous luminosity of 3.1×10^{33} cm^{-2} s^{-1}, PEP-II surpassed its design luminosity of 3.0×10^{33} cm^{-2} s^{-1} and broke the world luminosity record for an e^+e^- collider during the first run of the *BABAR* experiment. The maximum daily

integrated luminosity recorded by the *BABAR* detector during its first run, between October 1999 and the end of October 2000, was 152.5 pb^{-1}. The data used in the analyses presented here were acquired during this period. These data consist of 20.58 fb^{-1} of data taken near the $\Upsilon(4S)$ resonance mass, and 2.61 fb^{-1} of data acquired below the $\Upsilon(4S)$ resonance mass for the study of continuum backgrounds.

The future goal for the PEP-II machine is to increase its instantaneous luminosity to 1.5×10^{34} cm^{-2} s^{-1}, by increasing both the beam currents and the number of bunches in the beams. It is expected that by the end of the year 2005, a projected 500 fb^{-1} of $\Upsilon(4S)$ data will be available for analysis.

A detailed description of the design of PEP-II and an account of its performance, are given in references [38] and [39].

3.2 Overview of the *BABAR* Detector

In order to obtain maximum coverage of the boosted $\Upsilon(4S)$ events in the laboratory frame, the *BABAR* detector has an asymmetric design along the direction of the beams. For example, the electromagnetic calorimeter only has a forward end-cap, and the read-out electronics of the drift chamber are placed at the backward end of the detector. In addition, Figure 3.2 shows that the centre of the *BABAR* detector is shifted by 370 mm from the IP, in the direction of the more energetic e^- beam.

Apart from the forward-backward asymmetry of the detector, it has the conventional *onion shell* design used for colliding beam experiments. In this scheme, layers of active sub-detectors are arranged concentrically around the IP for particle detection and identification (ID).

BABAR's innermost sub-system is the Silicon Vertex Tracker (SVT). The SVT is a dedicated five layer system for the precision reconstruction of decay vertices. This detector also provides the main information for the measurement and reconstruction of low momentum tracks.

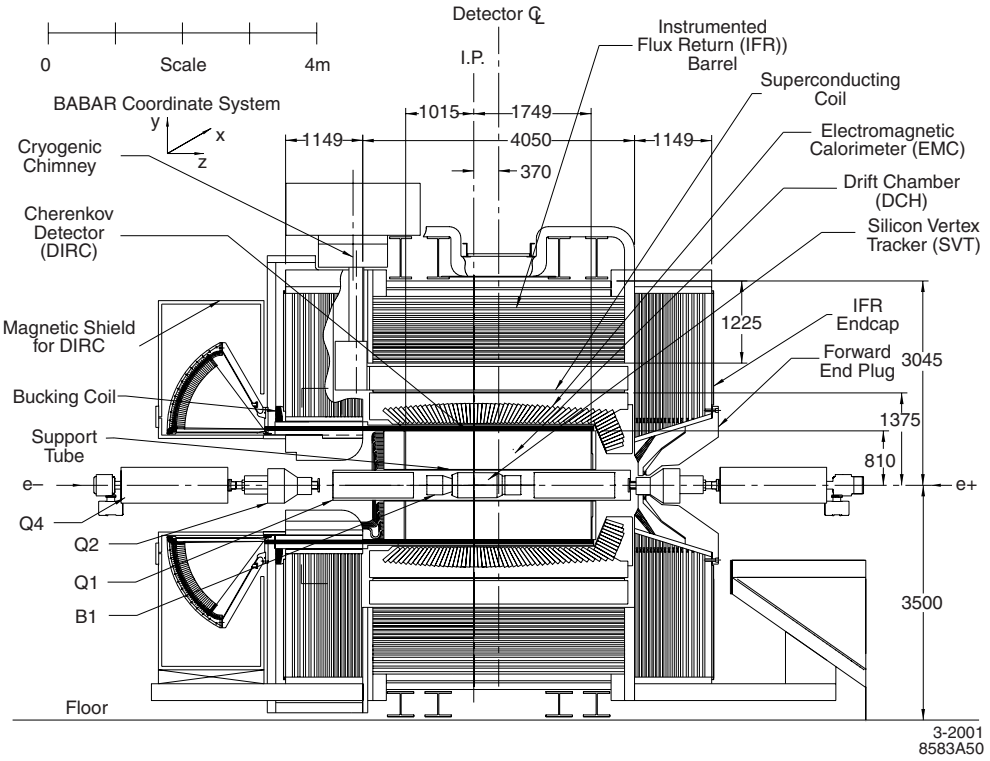

Figure 3.2: *Longitudinal cross-section through the BABAR detector. All dimensions are in millimetres. (From [1])*

The Drift Chamber (DCH), which surrounds the SVT, is the main tracking system of the *BABAR* detector. All of the tracking information necessary for the reconstruction of the decay modes presented here, is provided by the SVT and the DCH. In addition, these sub-detectors provide dE/dx measurements, which are the only means by which to obtain particle ID for tracks with transverse momenta below 700 MeV/c.

A unique feature of the *BABAR* detector is its dedicated particle ID sub-system, which is known as the Detector of Internally Reflected Cherenkov Light (DIRC). This system provides a separation between kaons and pions of better than 4σ for track momenta between 700 MeV/c and 3 GeV/c, and better than 2.5σ for track momenta of up to 4.5 GeV/c. This separation is approximately 10σ for tracks with momenta of 2 GeV/c. The DIRC is vital for the study of rare charmless hadronic B meson decays, where combinatorial backgrounds due to misidentified tracks are high.

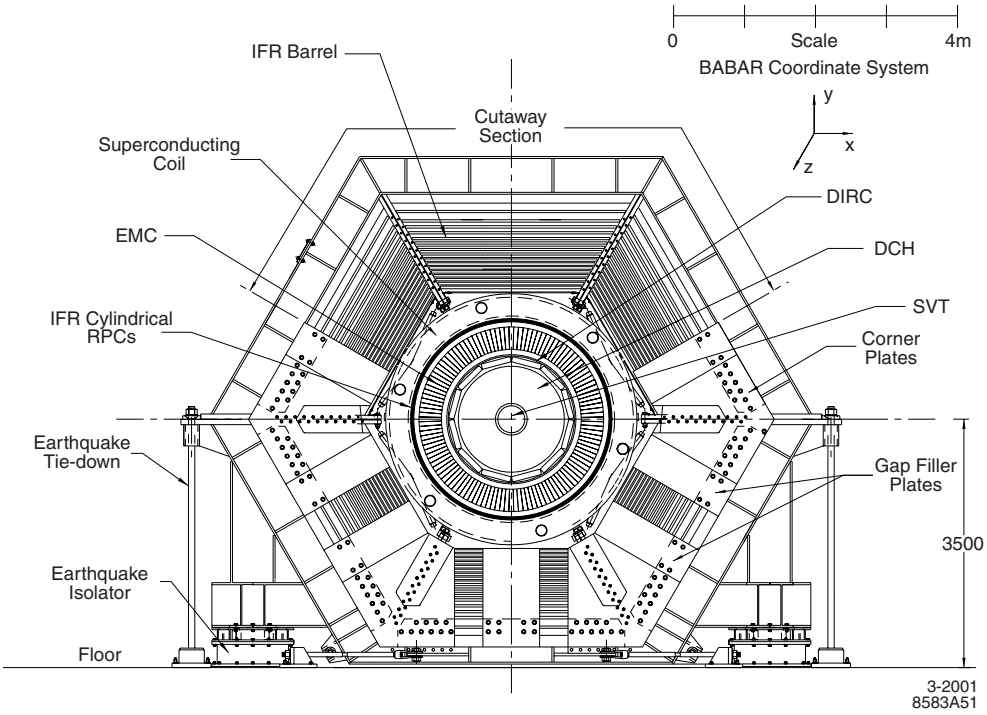

Figure 3.3: *Forward end view of the BABAR detector with the electromagnetic calorimeter's forward end-cap removed. All dimensions are in millimetres. (From [1])*

The Electromagnetic Calorimeter (EMC) is composed of Thallium-doped Caesium Iodide (CsI(Tl)) scintillator crystals in a barrel section and a forward end-cap section. Photon energies are measured and electrons are detected and identified in the EMC.

The Instrumented Flux Return (IFR) is the outermost sub-system of the *BABAR* detector. The IFR uses thin, planar, gas filled resistive plate chambers (RPC) for its active detector elements. The IFR is *BABAR*'s muon detector. It also provides signatures for neutral hadrons such as K_L^0 mesons. The RPCs are interleaved with the segmented steel flux return of the *BABAR* magnet, which consists of a barrel and forward and backward end-cap sections.

A full account of the *BABAR* detector with performance details of its individual sub-systems, up to the end of the 1999-2000 run, is given in reference [1]. The same reference was used in addition to references [15] and [40], for the descriptions given in Sections 3.3 through 3.9.

3.3 The Silicon Vertex Tracker (SVT)

The SVT serves the dual purposes of vertexing and tracking. It provides the only means by which to reconstruct tracks with transverse momenta of less than 120 MeV/c. For tracking, where any precision of information obtained far from the IP is compromised by multiple scattering, the SVT plays a crucial role in providing the required resolution for the angle of the tracks with respect to the IP.

During the first run of the *BABAR* experiment, an SVT hit reconstruction efficiency of 97% was obtained using $\mu^+\mu^-$ pair events. This was done by comparing the number of hits observed in each module, to that of the tracks passing through it. The longitudinal (z) and azimuthal (ϕ) spatial resolution of SVT hits is shown in microns in Figure 3.4. The spatial resolutions are obtained by measuring the distance between SVT hits and track trajectories in the plane of the SVT modules, after subtracting uncertainties in the track trajectories.

As a vertex detector, the SVT needs to provide vertex resolutions of better than 80 μm along the beam axis, and of the order of 100 μm perpendicular to the beam direction. These limits are necessary for the precise measurement of the relative decay lengths of the B^0 and $\bar{B}^0$ mesons for studies of time-dependent CP asymmetries. Further, good vertexing resolution of the SVT will enable precise determination of secondary decay vertices, and therefore, the measurement of the flight lengths of secondary decay products, which is crucial for their identification in the decay chain. For the measurement of the branching fractions presented here, where K^0_S mesons decay to two charged pions, the precision determination of the flight length of the K^0_S meson resulted in a significant reduction of combinatorial backgrounds.

The SVT can make up to ten dE/dx measurements for each track. This information can be used to achieve a 2σ separation between kaons and pions with momenta up to 500 MeV/c.

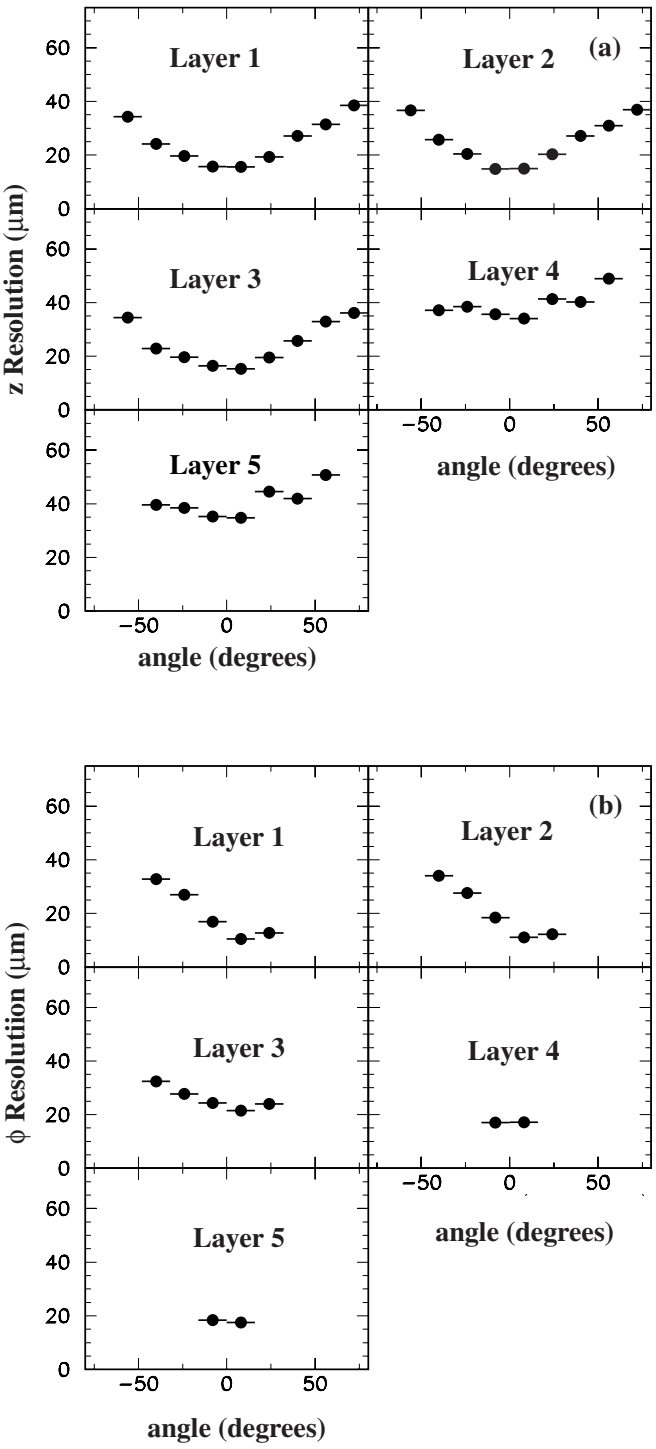

Figure 3.4: *a) The longitudinal (z) and b) azimuthal (ϕ) spatial resolutions of SVT hits in microns. The track incidence angle in the ϕ coordinate is smaller for layers 4 and 5, resulting in fewer points. (From [1])*

3.3.1 The SVT Design

The layout of the SVT is shown in Figure 3.5. It consists of five concentrically arranged cylindrical layers, each with double-sided active silicon sensors. The silicon strips on opposite sides of each layer are arranged orthogonally to provide z and ϕ readout. There are approximately 150,000 readout channels in the SVT.

This sub-detector is mounted within a tube on the support structure of the PEP-II beam pipe, and is independent from the rest of the *BABAR* detector. This arrangement requires careful monitoring of the movement of the SVT with respect to the rest of the detector, in particular, the DCH. Alignment data are required to correct for the relative movement of the SVT, to enable precision track matching with the rest of the *BABAR* detector. The movement of the SVT with respect to the B1 magnets, which are shown in Figure 3.2, and the position of the support tube with respect to the DCH, are monitored using a system of capacitive sensors and by reconstructing e^+e^- and $\mu^+\mu^-$ pair events.

The three innermost SVT layers, which are the most important for vertexing, are straight sections, while the outer two layers are arch shaped. The latter allow maximum possible coverage while minimising the track incidence angles at the edges of the SVT's acceptance. The solid angle coverage of this sub-detector is limited in the forward and backward directions by the beam's B1 steering dipole magnets. In order to satisfy the design of the five layers, six different types of silicon sensors were employed. Each layer is divided into forward and backward halves that are read out by front-end electronics (FEE) at each end, respectively.

3.4 The Drift Chamber (DCH)

BABAR's DCH is sandwiched between the support tube that houses the SVT, and the quartz radiator bars of the DIRC particle ID sub-detector. Longitudinally, it is positioned asymmetrically with respect to the IP to maximise event coverage in

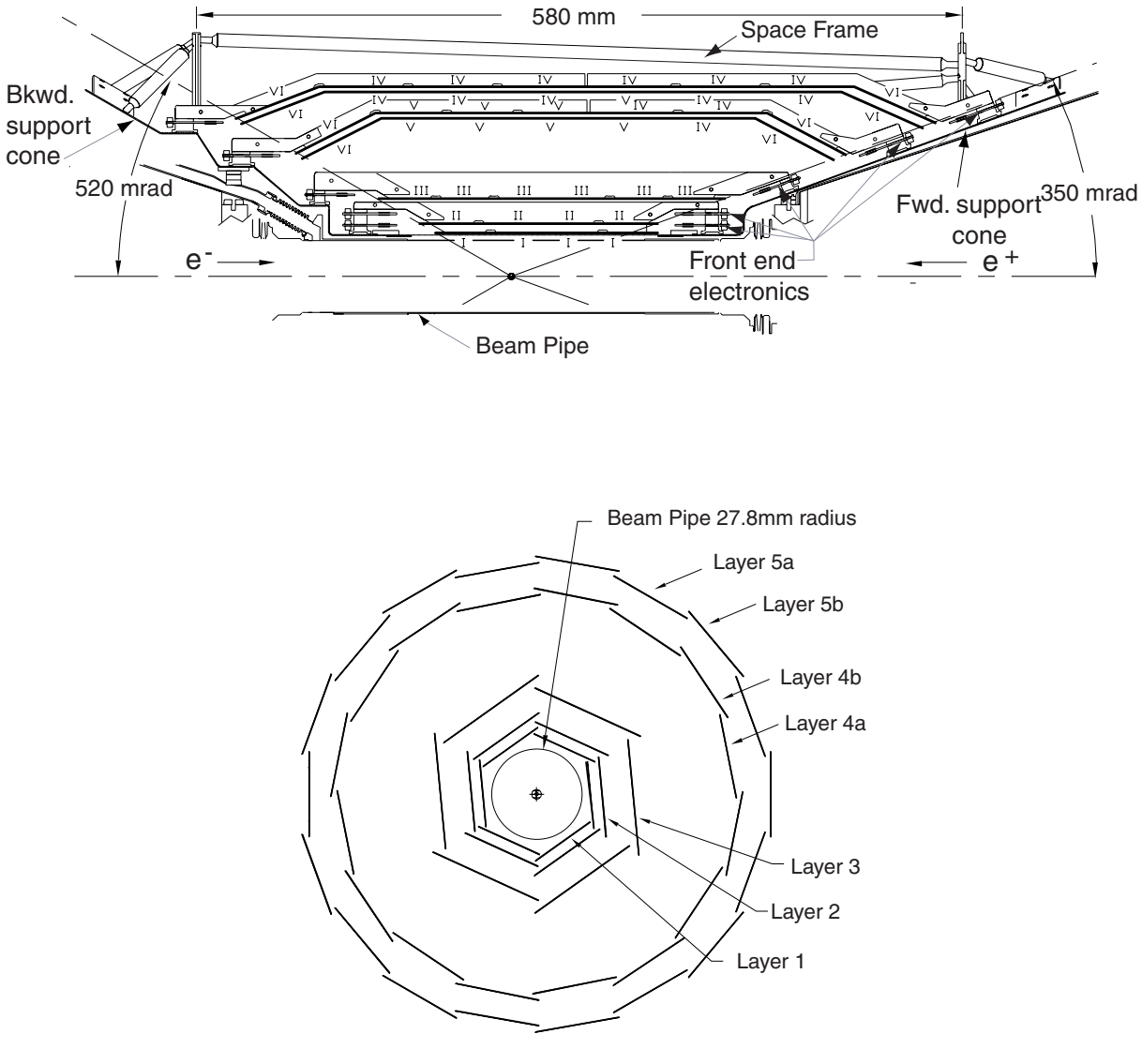

Figure 3.5: *Top half of a longitudinal cross-section (top) and schematic of a transverse cross-section (bottom) through the SVT. The Roman numerals indicate the six different types of silicon sensors employed. (From [1])*

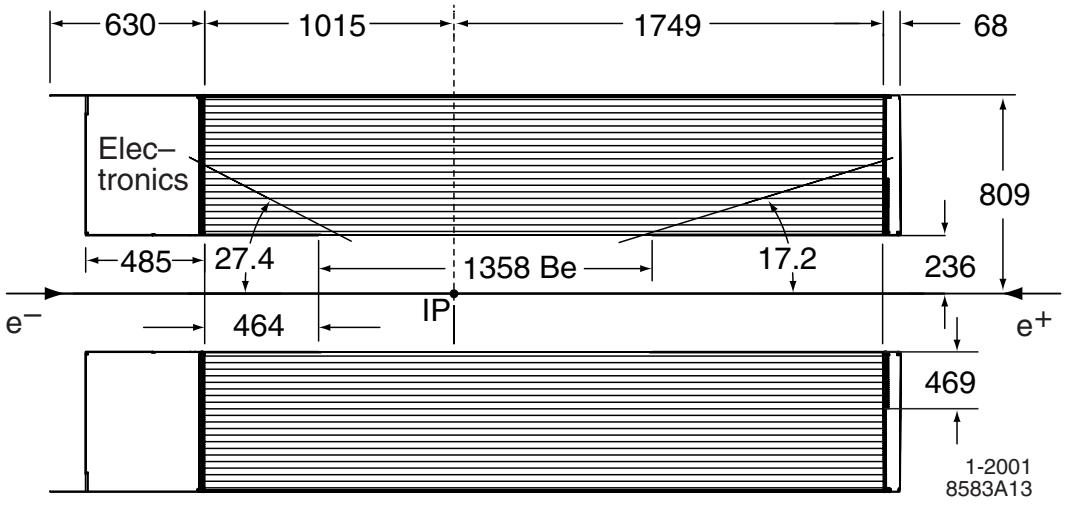

Figure 3.6: *Longitudinal cross-section through the DCH, showing the main dimensions in millimetres and the forward-backward asymmetry with respect to the IP. (From [1])*

the centre-of-mass frame. Figure 3.6 shows the dimensions of this sub-detector in millimetres.

The DCH is the main tracking system of the *BABAR* detector and provides transverse momentum measurements for charged particles. In addition, it is used to determine track angles at the entrance to the DIRC, which are needed for the measurement of the Cherenkov angle for particle ID. The DCH allows reconstruction of vertices outside the SVT by determining the longitudinal position of tracks using *stereo* layers of *sense* wires. These stereo layers are positioned at varying angles with respect to the detector's longitudinal axis. The determination of the decay vertices of K^0_S mesons by the DCH, supplements that from the SVT, for their identification using flight length measurement information.

Two track parameters, d_0 and z_0, measured at the point of closest approach to the z-axis, represent the distance of a track from the origin of the coordinate system in the x-y plane and along the z-axis, respectively. The difference between these parameters and the coordinates of the vertex of the remaining tracks in the event, is used as the resolution on these parameters. These resolutions are dependent on the transverse momentum $p_{\rm t}$ of the tracks. At $p_{\rm t}$ = 3 GeV/c, resolutions of σ_{d_0} = 25 μm and

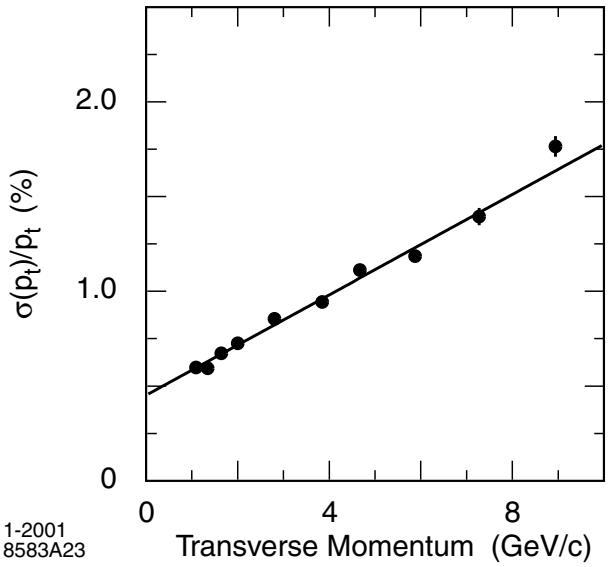

Figure 3.7: *Resolution of the measured transverse momentum, σ_{p_t}/p_t, as a function of the transverse momentum p_t in the DCH. (From [1])*

$\sigma_{z_0} = 40$ μm were measured for hadronic events.

The resolution of the measured transverse momentum, σ_{p_t}/p_t, is determined using cosmic ray muons that traverse both the DCH and the SVT. For p_t measured in GeV/c, this resolution is shown in Figure 3.7 and is given by,

$$\frac{\sigma_{p_t}}{p_t} = (0.13 \pm 0.01)\% \cdot p_t + (0.45 \pm 0.03)\% \,. \tag{3.1}$$

By measuring dE/dx for tracks, the DCH provides particle ID in the barrel region in conjunction with the DIRC. For the extreme forward and backward tracks, however, the DCH is the main sub-detector for particle ID. Figure 3.8 shows the measured dE/dx, which has been corrected for a number of physical effects, as a function of track momentum. The difference between the measured and the expected dE/dx for electrons from Bhabha scattering is shown in Figure 3.9. An rms resolution of approximately 7.5% was achieved for the data from the first run of the *BABAR* experiment.

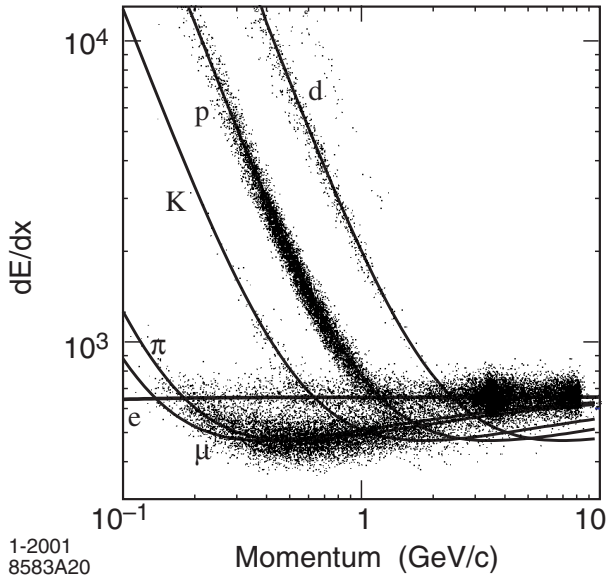

Figure 3.8: *Corrected DCH dE/dx measurements as a function of momentum, for a sample of data obtained using beam background triggers. The Bethe-Bloch fits are derived from various control samples from data. (From [1])*

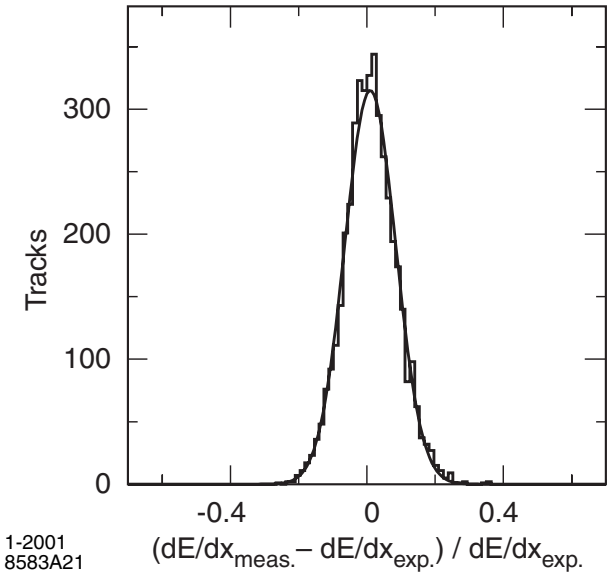

Figure 3.9: *The difference between the measured and expected dE/dx for electrons from Bhabha scattering, with the DCH operating at a sense wire voltage of 1900 V. (From [1])*

3.4.1 The DCH Design

The DCH has 7,104 hexagonal cells corresponding to the same number of readout channels. Each hexagonal cell has a sense wire in the middle of the cell, which is surrounded by six *field-shaping* wires. Figure 3.10 shows the arrangement of these cells into 40 concentric layers, which are divided into ten concentric super-layers. The boundaries of the super-layers are divided by field-shaping *guard* wires, so that the cells on the edges of the super-layers have one regular field-shaping wire replaced by two guard wires. There are four axial (A) super-layers and six stereo (U and V) super-layers that are longitudinally arranged at varying angles with respect to the A layers. This setup allows the longitudinal position of tracks to be ascertained to within 1 mm.

The design and choice of components for the DCH have been optimised to reduce multiple scattering. In particular, an 80:20 mixture of helium:isobutane gas is used in the chamber in order to improve momentum resolution and to obtain the best match to SVT tracks. In addition, the mechanical components have been chosen in order to reduce the amount of material in front of the DIRC, the EMC, and the IFR subsystems. Part of the forward end-plate, which covers the acceptance of the EMC's end-cap, is made thinner, and the inside and outside cylindrical walls are made of 1 mm beryllium and a carbon-composite material, respectively. The front-end readout electronics and high voltage (HV) supply are mounted on the backward end-plate of the DCH.

Although the DCH was designed to work with a sense wire operating voltage of 1960 V, this voltage was reduced to 1900 V for the first part of the data acquired during the first run of the experiment. This measure was taken out of concern for a small region of the chamber that was damaged during the commissioning phase of the detector. The damage affects 10.4% of superlayer 5 and 4.2% of superlayer 6. At the design voltage of 1960 V, an average track reconstruction efficiency of $98 \pm 1\%$ was obtained for tracks with $p_t \geq 200$ MeV/c and polar angle $\theta > 500$ mrad. For tracks at normal incidence, a 5% drop in efficiency was observed for the reduced operating voltage of 1900 V.

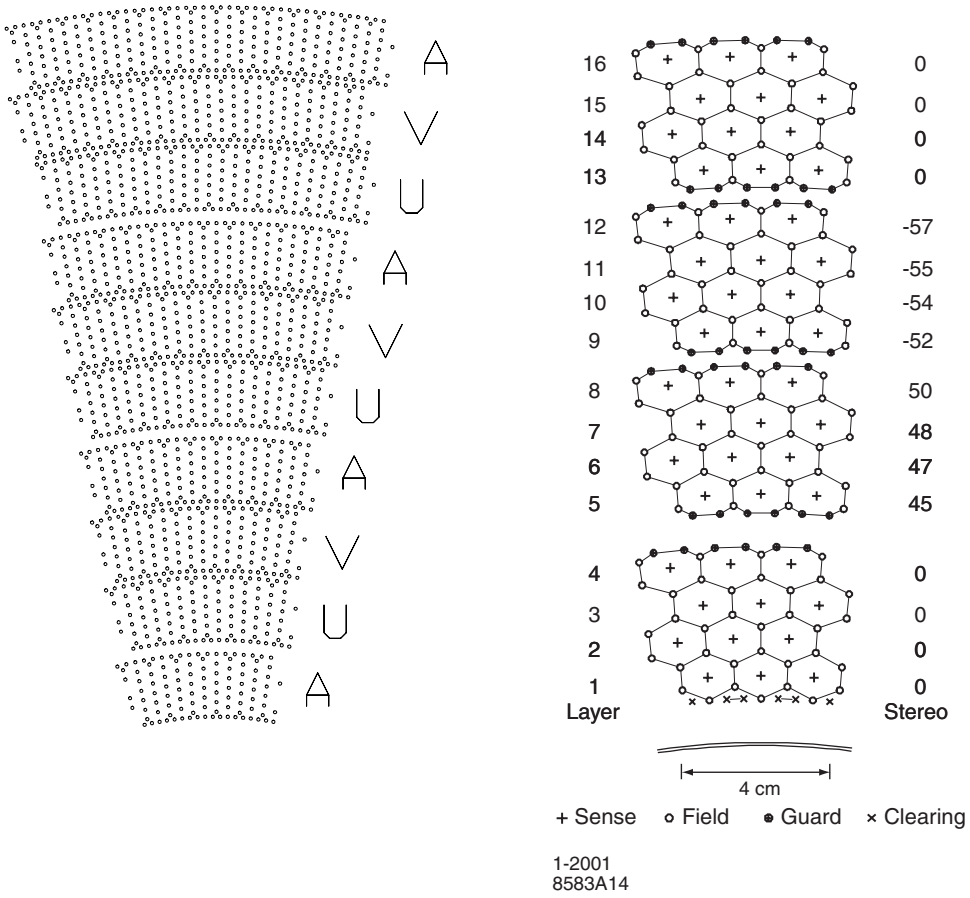

Figure 3.10: *Transverse cross-sections through the DCH, showing a segment of the 40 layers of hexagonal cells that are arranged into 10 super-layers (left), and the four innermost super-layers (right). The cell boundaries and the angles of the stereo layers in mrad, are shown in the latter. (From [1])*

3.5 The Detector of Internally Reflected Cherenkov Light (DIRC)

The ability to successfully identify tracks as particles of a particular type, and in particular to separate those charged particles with high multiplicity, namely pions and kaons, is of the utmost importance for measuring CP asymmetries in the B meson system. In addition, the importance of particle identification cannot be overstated in the reconstruction of rare hadronic decays, where combinatorial backgrounds due to track misidentification are prominent. In the measurements described here, where the hadronic final states include only charged pions and kaons, the separation of these particles with low misidentification rates is critical. The DIRC was designed with this purpose in mind.

The DIRC is a new type of particle ID detector that is based on the principle of Cherenkov radiation. Figure 3.11 shows that when relativistic charged particles traverse the DIRC's quartz radiator bars with $\beta > 1/n$ (where $n = 1.473$ is the index of refraction of the quartz), cones of Cherenkov light are emitted. Some of the photons from these cones of light fall within the total internal reflection limit of the radiator bars, which also act as light guides, and are transported within them. Having been focused by an optical wedge and transported through an expansion tank of purified water called the *standoff box*, these photons are imaged onto an array of closely packed photomultiplier tubes (PMTs) at the backward end of the detector. Cherenkov light travelling to the forward end is reflected to the instrumented backward end by a mirror at the forward end of each radiator bar.

The ability of the DIRC to provide information on the difference between the measured and the expected photon arrival times, helps in suppressing beam induced background hits and assigning signal photons to the tracks that produced them in the event. This ability is also used to resolve forward-backward ambiguities.

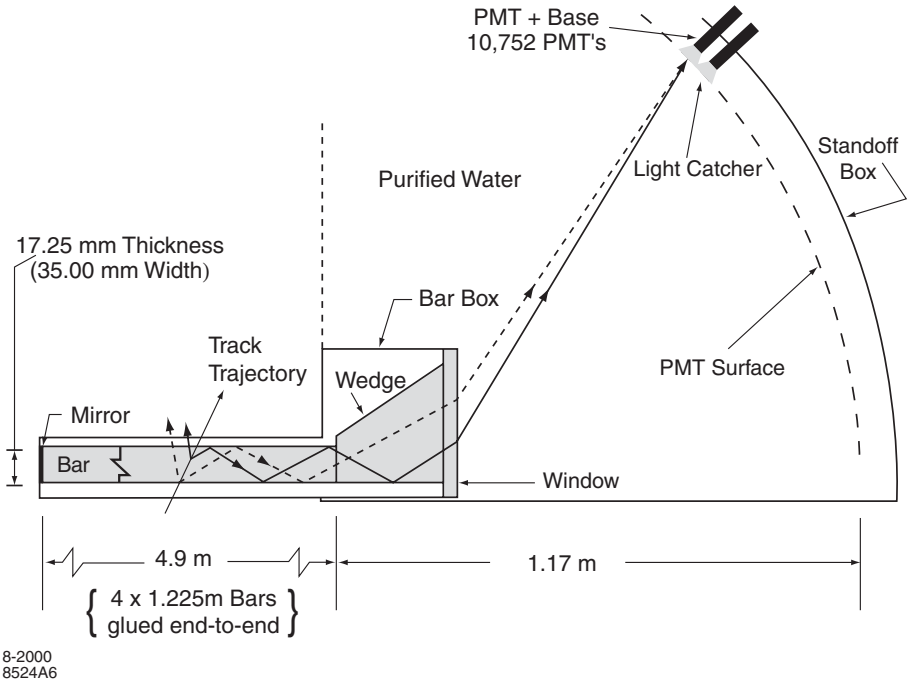

Figure 3.11: *Schematic of the DIRC sub-detector, showing the fused silica radiator bar, which is used to transport the Cherenkov photons emitted within it, the optical wedge, which is used to focus the photons onto the PMT array, and a region of the expansion tank of purified water with the array of imaging PMTs. Note that, in contrast to previous figures of the BABAR detector, the e^- beam is travelling to the left in this diagram. (From [1])*

3.5.1 The DIRC Design

The DIRC's radiator bars are made from synthetic fused silica, which has an index of refraction of $n = 1.473$. Each bar is 17 mm thick and 35 mm wide in cross-section, and is comprised of four sections that are glued end-to-end for a total length of 4.9 m. Hermetically sealed bar boxes are used to house 12 radiator bars arranged next to each other as shown in Figure 3.12. There are twelve bar boxes, which are arranged into a polygonal barrel between the DCH and the EMC sub-systems.

The PMTs are arranged on the outside wall of the standoff box as shown in Figures 3.11 and 3.13. There are 12 PMT sectors each instrumented with 896 PMTs in a close

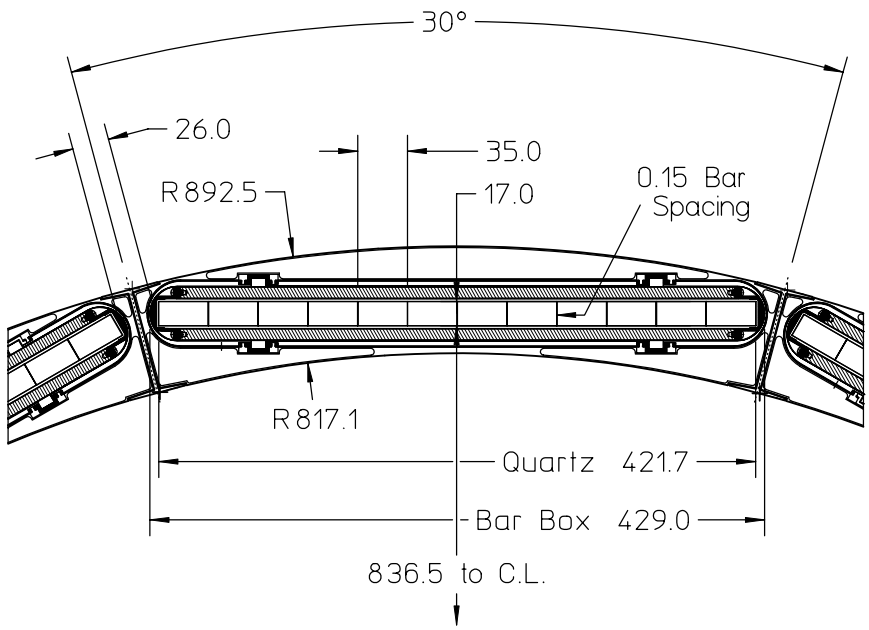

Figure 3.12: *Cross-section through a DIRC bar box, which houses 12 radiator bars. All dimensions are in millimetres. (From [1])*

packed configuration. The PMTs are magnetically shielded by an iron shield, which is enhanced by a bucking coil.

3.5.2 Particle Identification

An unbinned maximum likelihood method is employed to combine all of the space and timing measurements provided by the DIRC, in order to determine a particle hypothesis for each track. It is possible to maximise the likelihood for a given hypothesis for each track to be any of the following, e, μ, π, K, or p. In turn, the likelihood for the entire event is maximised iteratively by setting different hypotheses for each track.

The primary task is to associate the pattern formed by the Cherenkov photons with a track whose momentum and direction are determined by the tracking system, and then to measure the Cherenkov angle due to that track. Once this information is

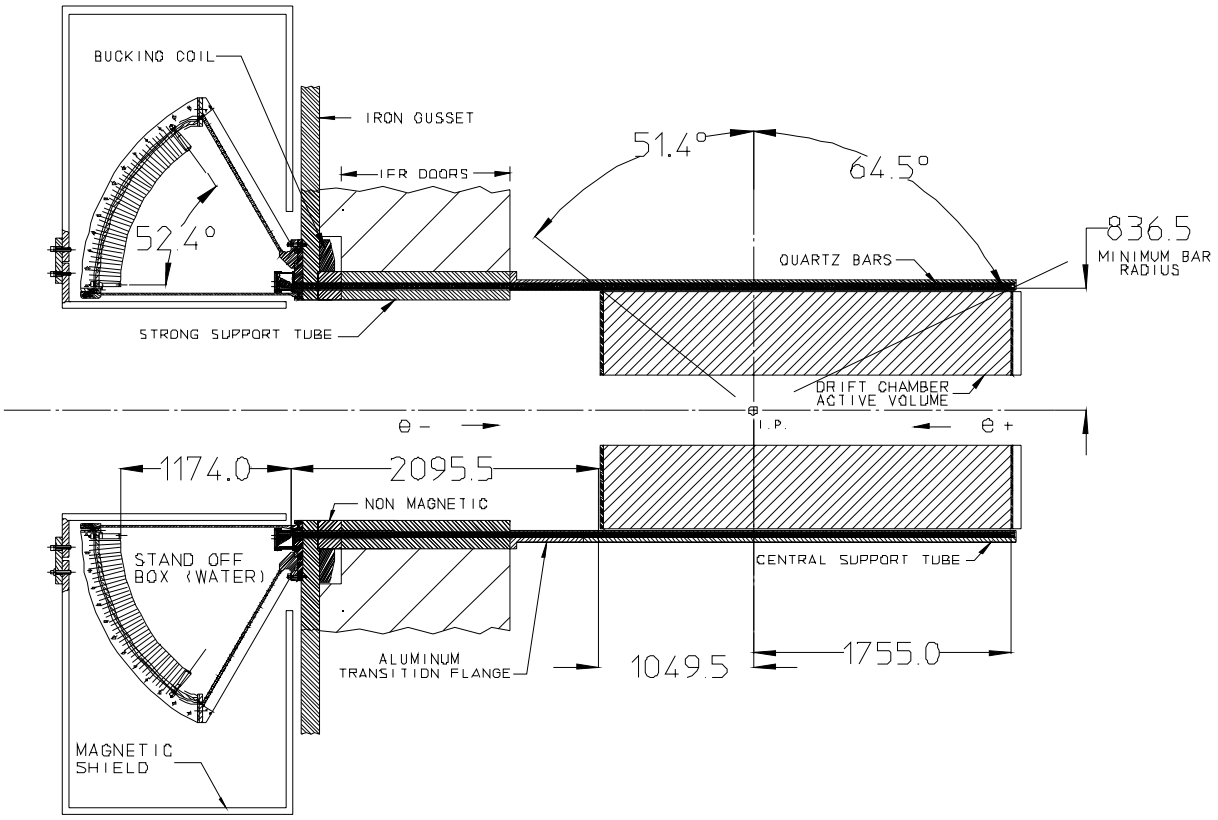

Figure 3.13: *Longitudinal cross-section through the DIRC sub-detector, showing the radiator bars (Quartz Bars) and the expansion tank (Stand Off Box) with the array of PMTs. Also shown is the relative position of the DCH. All dimensions are in millimetres. (From [1])*

determined, a particle hypothesis can be assigned to that track using the maximum likelihood method.

The expected pion-kaon separation of the DIRC as a function of the transverse track momentum p_{t}, is shown in Figure 3.14 for $B^0 \to \pi^+\pi^-$ events. This figure shows a separation of 4.2σ between pions and kaons at $p_{\mathrm{t}} = 3$ GeV. Figure 3.15 shows the efficiencies for correctly identifying kaons and misidentifying pions as kaons, for a control sample of $D^0 \to K^-\pi^+$ decays that were selected kinematically from D^{*+} meson decays. The average efficiencies for kaon selection and pion misidentification are $96.2 \pm 0.2\%$ and $2.1 \pm 0.1\%$, respectively.

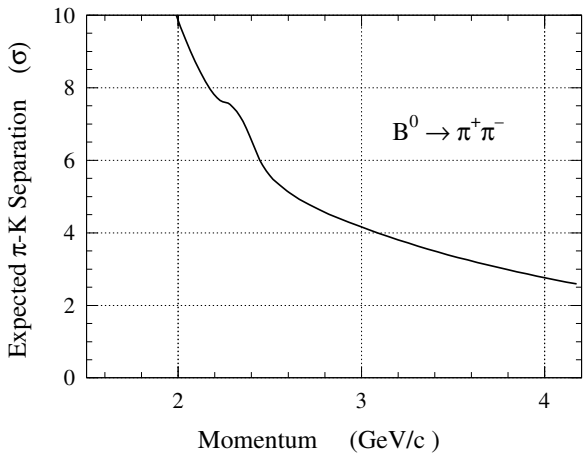

Figure 3.14: *The expected pion-kaon separation for $B^0 \to \pi^+\pi^-$ events, inferred from DIRC studies using $\mu^+\mu^-$ pair events. (From [1])*

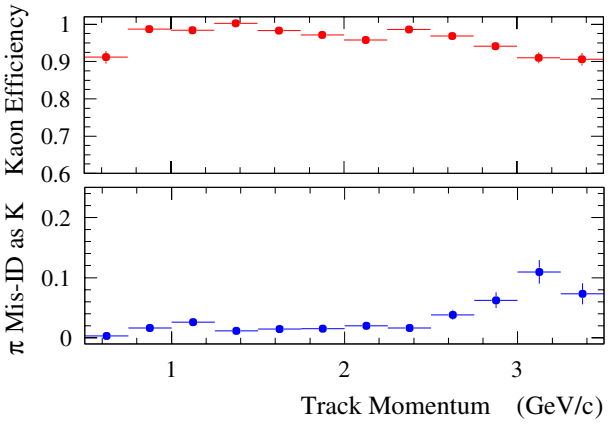

Figure 3.15: *The efficiencies for kaon selection and the misidentification of pions as kaons, is shown for a control sample of $D^0 \to K^-\pi^+$ decays that were selected kinematically from D^{*+} meson decays. (From [1])*

3.6 The Electromagnetic Calorimeter (EMC)

The EMC is designed for the detection of photons, and hence, the reconstruction of π^0 and η mesons, and for the identification of electrons and neutral hadrons. Good energy resolution is required to enable the detection and reconstruction of particles over a range of energies, from soft-π^0 mesons from D^* meson decays, to high energy photons and the π^0 and η mesons from rare B decay processes. In addition, high spatial resolution is required for the angular resolution of photons, especially from the decays of high energy π^0 and η mesons.

3.6.1 The EMC Design

The EMC consists of highly segmented barrel and end-cap sections of Thallium-doped Caesium Iodide (CsI(Tl)) scintillator crystals. There are 5,760 crystals arranged in 48 azimuthal rings in the barrel, and 820 crystals arranged in 8 rings in the forward conical end-cap. The crystals are trapezoidal and are produced in a variety of lengths and transverse dimensions. This is to limit shower leakage and to accommodate the required geometry of the EMC, with the longitudinal axis of each crystal pointing toward one point, which is slightly offset from the IP. Figure 3.16 shows the arrangement of the crystals in the barrel and forward end-cap sections. The end-cap is vertically split into two halves that can be moved out to allow access to the central part of the detector.

Each crystal is polished and wrapped using a reflective Tyvek material to aid light transport. Aluminium foil is used to provide radio-frequency (RF) shielding and a Mylar wrapping is used to provide electrical insulation. Each crystal is read out by two silicon PIN photodiodes and a local preamplifier circuit, which are arranged on the back-end of the crystal. The signals from the PIN photodiodes are averaged to provide an energy measurement. Figure 3.17 shows the schematic of a single crystal and its readout system.

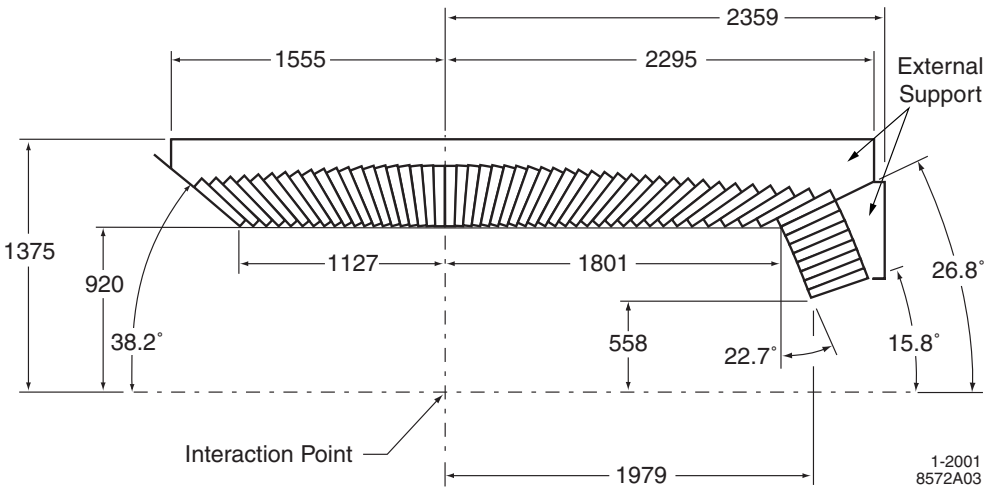

Figure 3.16: *Top half of a longitudinal cross-section through the EMC, showing the arrangement of the 48 barrel and the 8 forward end-cap rings. The EMC is azimuthally symmetric. All dimensions are in millimetres. (From [1])*

3.6.2 Candidate Selection

Candidates in the EMC are reconstructed from *clusters* of neighbouring crystals that have energy deposited in them. Local maxima of energy deposits within clusters are identified as *bumps*, with one or more bumps per cluster. The centroid of a bump can be determined from the weighted sum of the energies in neighbouring crystals. The determination of the weights for each crystal, and hence the centroid position, is an iterative process. Bumps and tracks may be matched by projecting tracks to the EMC face. This match is successful if the distance between the centroid of a bump and the track is consistent with the angle and momentum of the track, according to predetermined criteria.

Photons are identified as bumps that are not associated with any tracks and have a symmetrical shower shape about the bump indicating an electromagnetic interaction. The shower shape is determined using the lateral moment (LAT) of the shower, which

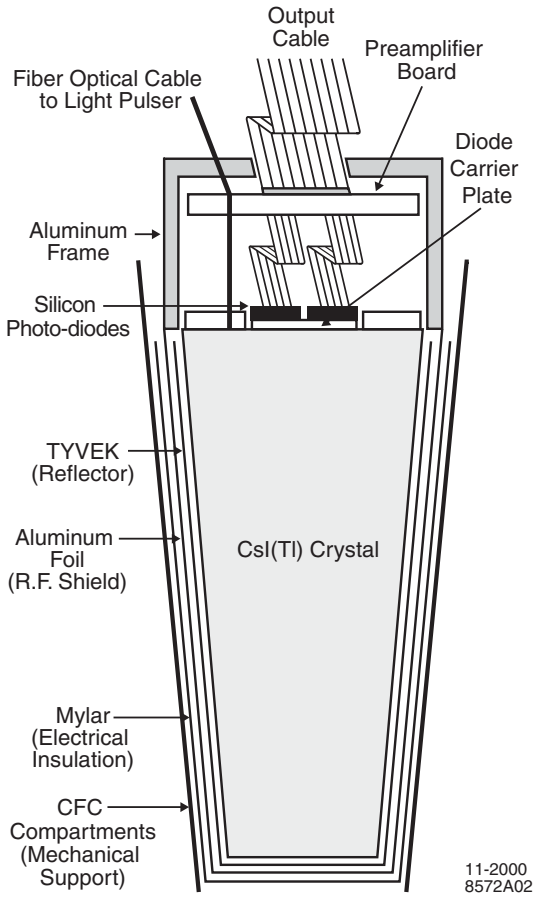

Figure 3.17: *Schematic diagram of a single CsI(Tl) crystal, showing the readout system (the two PIN photodiodes and the preamplifier board) and the various layers of wrapping. (From [1])*

is defined by,

$$LAT = \frac{\sum_{i=3}^{N} E_i r_i^2}{\sum_{i=3}^{N} E_i r_i^2 + E_1 R_0^2 + E_2 R_0^2}, \tag{3.2}$$

where r_i and R_0 are defined in Figure 3.18, and E_i is the energy deposited in crystal i. The LAT is small for electromagnetic showers, which deposit their energy symmetrically.

The energy dependent photon energy resolution, $\frac{\sigma_E}{E}$, was determined using a number

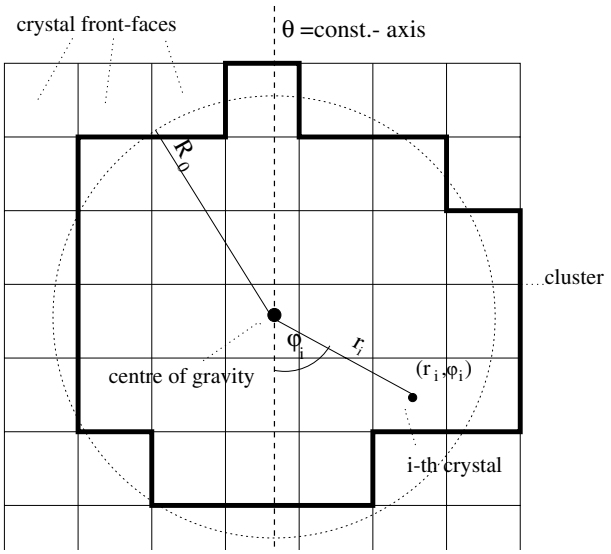

Figure 3.18: *Schematic diagram of an EMC cluster, showing the definitions of* r_i *and* R_0*. (From [15])*

of methods. For energies below 2 GeV, the mass resolution of π^0 and η mesons decaying to two photons of similar energy was studied. In addition, the decay $\chi_{c1}(1P) \to \gamma J/\psi(1S)$ provided a photon energy resolution measurement for an average energy of 500 MeV, while the measurement for higher energy photons were made using Bhabha scattering events. For the energy E measured in GeV, a fit to these data results in a resolution of,

$$\frac{\sigma_E}{E} = \frac{(2.32 \pm 0.30)\%}{\sqrt[4]{E}} \oplus (1.85 \pm 0.12)\% \,. \tag{3.3}$$

Electrons are identified by measuring the ratio of their shower energy to their track momentum, E/p. This quantity is close to one for electrons, since they deposit almost all of their energy in the EMC. The LAT is also used to discriminate between electrons, which produce symmetrical electromagnetic showers, and charged hadrons. For a candidate that is identified as an electron by the EMC, the dE/dx energy loss measurement from the DCH and the Cherenkov angle measurement from the DIRC must also be consistent with those for an electron.

3.7 The Superconducting Magnet

For the measurement of charged track momenta, a superconducting solenoid is used to provide a 1.5 T magnetic field in the direction of the detector's z-axis. The z-axis is offset in the horizontal plane by approximately 20 mrad from the direction of the e^- beam. This offset between the detector axis and the beam direction is used in the separation of the e^+ and e^- beams.

The steel flux return of the magnet together with a bucking coil in the backward end, serve to provide a uniform longitudinal field within the tracking volume of the *BABAR* detector. The radial field gradient must be small in order for the beam steering and focusing magnets to perform optimally.

3.8 The Instrumented Flux Return (IFR)

The outermost sub-system of the *BABAR* detector is the IFR. This sub-detector makes use of the multilayered steel flux return of the *BABAR* magnet as an absorber of hadrons, to allow only muons to pass through. It is the muon identifier of the *BABAR* detector. The IFR is also used to detect neutral hadrons such as K_L^0 mesons.

Figure 3.19 shows the steel flux return of the magnet, which is arranged into a barrel section and two end door sections. Each of the end door sections is vertically divided into two halves that can be separated to allow access to the inner detector. The barrel and the end door sections are made up of layers of steel, which are interleaved with 19 and 18 layers, respectively, of gas filled planar RPC detectors. The RPCs provide two dimensional readout of streamers from ionising charged particles that traverse the gas in the chamber. A schematic of the RPC cross-section is shown in Figure 3.20.

In addition to the planar RPCs that are interleaved with the layers of the steel flux return, there are two layers of cylindrical RPCs around the EMC to detect particles exiting the EMC.

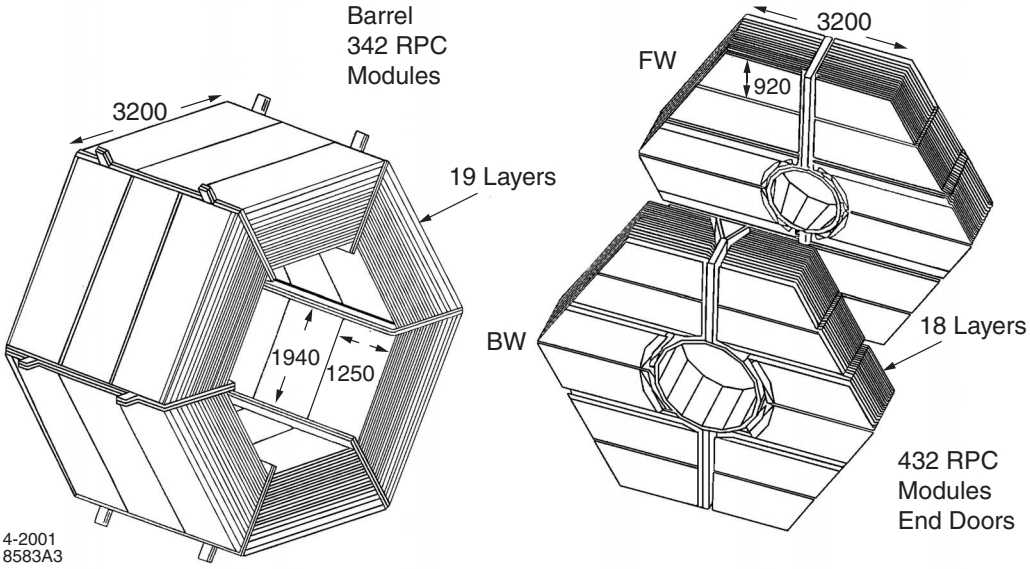

Figure 3.19: *The IFR barrel and forward (FW) and backward (BW) end door sections, showing the layers of steel of varying thickness. The dimensions of the RPC detectors are shown in millimetres. (From [1])*

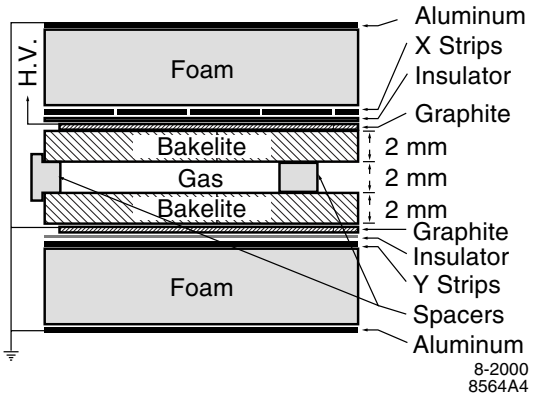

Figure 3.20: *Schematic diagram of the cross-section through the planar RPCs used in the IFR. (From [1])*

Basic candidate identification by the IFR involves the reconstruction of three-dimensional clusters of hits and their association to track information from the tracking systems. Various algorithms provide selection criteria, which are applied for the identification of muons and charged hadrons for track matched clusters. Neutral hadrons, including K_L^0 mesons, are identified as clusters with no associated tracks. Although energy information is not available from the clusters, it is possible to identify particles from a particular decay by comparison of the missing momentum from that decay and the direction of the cluster as determined from the IP.

3.9 The *BABAR* Trigger System

The *BABAR* trigger system is designed to select $B\bar{B}$ events with an efficiency of over 99%, while rejecting unwanted background events. It is implemented in two stages, the Level 1 (L1) trigger in hardware, and the Level 3 (L3) trigger in software. There is as yet no Level 2 (L2) trigger, but this is a designed redundancy stage that may be necessary when the machine luminosity is increased beyond current design limits.

At the design luminosity of 3.0×10^{33} cm^{-2} s^{-1} and a centre-of-mass energy of 10.58 GeV, the typical machine induced background rate is about 20 kHz, while the rate for $b\bar{b}$ production is 3.2 Hz. The L1 trigger efficiency for $b\bar{b}$ events is 100% with an overall output rate of up to 2 kHz. The L3 trigger filters physics events from the output of the L1 trigger with an acceptance rate of approximately 90 Hz.

The L1 trigger is based on three independent triggers. These are, the Drift Chamber Trigger (DCT), the Electromagnetic Calorimeter Trigger (EMT), and the Instrumented Flux Return Trigger (IFT). The latter acts as a muon trigger for cosmic ray and $\mu^+\mu^-$ pair events. Information on the location and energy of tracks and energy deposits is sent from these triggers to a Global Level 1 Trigger (GLT), and is summarised into predefined triggers that are designed to select specific physics events.

The predefined triggers can contain information from either of the DCT or EMT, or from a mixture of different triggers. This information is passed to a Fast Control

and Timing System (FCTS), where the final trigger decisions are made for event selection. The predefined triggers are made up of especially defined trigger primitives (or criteria) from the DCT, EMT, and IFT, with adjustable thresholds set for each primitive. Trigger primitives for the DCT are defined by track lengths and momenta, for the EMT by energy deposits with various topologies and energy thresholds, and for the IFT by the number of signals with various topologies.

The L3 trigger selects events from the output of the L1 trigger using information from the FCTS. The L3 selection process is based on entire event data, which are used to construct selection criteria such as total event energy and track multiplicity, using specific tracking and calorimeter clustering algorithms. These selection criteria are logically combined to determine a pass or fail condition for each event. The L3 software filters use the standard data analysis framework used in *BABAR* for offline analysis. It is possible, therefore, to include any analysis code in the L3 filtering process for the selection of specially defined physics events.

Chapter 4

The *BABAR* Software and Data

4.1 The *BABAR* Software Environment

The *BABAR* software environment is divided into the online and offline systems. The online environment is the amalgamation of the sub-systems that provide real-time detector control and calibration, and data acquisition, monitoring, and processing. The offline environment consists of the physics tools that are available for the filtering of data and data reconstruction and analysis. Both environments are based on an *object-oriented* (OO) design architecture using the C++ programming language. The code is divided into specific modules, each of which performs a particular task. Due to the homogeneity of the online and offline systems, physics application tools developed in the offline environment can be easily implemented in the online environment.

Although the online system consists mostly of OO based C++ code developed within *BABAR*, parts of the system make use of other available software. These include the Experimental Physics and Industrial Control System (EPICS) [41], which is used as the interface for detector control, and the Java Analysis Studio (JAS) [42], which is used as the interface for data quality monitoring.

High level data analysis can be undertaken using the ROOT Object-Oriented Data Analysis Framework [43], which is based on the C++ programming language, or the

Physics Analysis Workstation (PAW) software package [44], which is based on the Fortran programming language. Both of these packages are available from the CERN Program Library and include interfaces to well established software such as COMIS, HBOOK, HIGZ, MINUIT, and ZEBRA, all of which are available from the same source.

4.2 Data Acquisition and Processing

The *BABAR* data acquisition (DAQ) system is part of the detector's online computing system. The first stage of the DAQ chain is controlled by the Online Data Flow (ODF) software. In ODF, raw data from the front-end electronics (FEE) of each sub-detector are routed to sub-detector specific VME based readout modules (ROMs). Once the data are collated by ODF, they are passed from the ROMs to a farm of 32 Unix workstations, which undertake the Online Event Processing (OEP) and L3 filtering. Accepted events are written to a disk buffer for reconstruction by the Online Prompt Reconstruction (OPR) software, prior to being transferred as reconstructed data to a High Performance Storage System (HPSS) database.

The use of sub-detector specific ROMs results in a DAQ system that is physically divided into sub-detector *partitions*. The ROMs are based around single-board computers that run detector specific software. They perform gain and pedestal corrections, as well as data sparsification and formatting. In addition, electronics calibrations are processed in the ROMs and used for feature extraction of signals at this stage.

The DAQ system is also divided into independent *virtual* partitions for simultaneous data acquisition from individual sub-detector systems. This feature is implemented in the Online Run Control (ORC) system, which provides a graphical user interface for the logical management of all detector systems for data acquisition and for performing calibrations. Sub-detector calibrations are run in parallel once a day for sub-detector specific diagnostics.

The ODF sub-system is responsible for the delivery of all raw event data from the FEE,

via the ROMs, to the OEP farm. This process involves the control and configuration of the FEE, the gathering of event data from the FEE after receiving an L1 accept, and the processing of sub-detector data for calibrations.

The OEP sub-system runs on a set of 32 parallel Unix nodes as part of the online system. The L3 software trigger is run within the OEP environment. The histograms that are produced for real-time data quality monitoring, are accumulated during partial data reconstruction by the OEP. Any deviation of the data quality from a set of predefined reference data, is indicated in a run logbook by the shift operators.

Events passing the L3 filters are sent to a Logging Manager (LM). The data from all 32 OEP nodes are combined and written to a single file for each run by the LM. This file is then retrieved for full event reconstruction by OPR. The OPR sub-system bridges the online and offline systems. It performs full event reconstruction and the key task of *rolling calibrations*, where calibration constants generated during event reconstruction for one run, are then used during the reconstruction of events in the next run by OPR.

Complete reconstruction of events and their classification into streams of different event types, such as `isMultiHadron` or `isPhysicsEvents`, by OPR, is undertaken on a dedicated farm of Unix machines. The detector configuration data, calibration and alignment constants, and the detector parameters and environmental data, are all used by OPR in the reconstruction of data for analysis. Fully reconstructed data are archived to the object-based Objectivity database, which is hosted on the HPSS.

Reconstructed data are written out to a hierarchy of databases containing various levels of detail. These include the `reco`, `micro`, and `nano` databases. The `reco` database includes full details of the event that can be used in detailed analyses. The `micro` database, used for the analyses presented here, contains lists of track and cluster candidates and summary event information produced during reconstruction, and thus, does not allow the full flexibility offered at the `reco` level. The `nano` database, also known as the *tag* database, is used to filter the data into smaller *skimmed* data-sets. This filtering can be undertaken during or after data processing by OPR.

The inclusive `isPhysicsEvents` stream is skimmed into more exclusive data-sets using the event information provided in the tag database. These exclusive skims are defined for different analysis types and implemented by specific software filters in OPR. For the analyses presented here, an instantiation of a charmless three-body B decay filter was used, which reconstructs B^0 mesons from two oppositely charged tracks and a K^0_S meson to produce the `BCCKs3body` skim. This skim contains less than 1% of all of the `isPhysicsEvents` data.

4.3 Data Definition

The *detector data* used for the analyses presented here were taken during the first run of the *BABAR* experiment, in a twelve month period between October 1999 and October 2000. This data sample consists of 20.58 fb^{-1} of *on-resonance* data taken near the $\Upsilon(4S)$ resonance mass, which correspond to 22.55 million $B\bar{B}$ events. In addition, 2.61 fb^{-1} of *off-resonance* data acquired at a nominal centre-of-mass energy of 40 MeV below the $\Upsilon(4S)$ resonance mass, were used for the study of continuum backgrounds from real data.

Section 3.4.1 mentioned the reduction of the DCH sense wire voltage from the design value of 1960 V to 1900 V, for a fraction of the data acquisition period during the first run of the *BABAR* detector. Table 4.1 summarises the amount of on-resonance and off-resonance data used for the analyses presented here, for each voltage setting. Data taken with the voltage set to 1900 V and 1960 V are referred to as *block1* (b1) and *block2* (b2) data, respectively.

The treatment of data from acquisition by the FEE of the sub-detectors to storage in the Objectivity database, was outlined in Section 4.2. In the Objectivity database, the data skims created during OPR are made available for specific analyses. For the analyses presented here, the data filtered to the `BCCKs3body` skim in the `micro` database were used.

Table 4.1: *Summary of the amounts of data used for the analyses presented here, acquired at each of the DCH sense wire voltage settings during the first run of the BABAR experiment.*

		Data (fb^{-1})	
Data Block	DCH Voltage (V)	On-resonance	Off-resonance
b1	1900	11.14	1.24
b2	1960	9.44	1.37

4.4 Monte Carlo Simulated Data

Monte Carlo (MC) simulated event generation is implemented by a combination of two generators. The `EvtGen` generator [45] is used for the decay of B mesons to exclusive final states, while the `Jetset 7.4` generator [46] is used for all other inclusive B decays, and to generate generic continuum events. For the exclusive decay modes, decay trees and corresponding branching fractions can be specified by users in a `DECAY.DEC` file that is then used in the production of simulated events.

Full MC detector simulation was achieved using a `Geant321` [47] based package named `BBsim`. `BBsim` is linked to the event generators via a package called `Beget`. It undertakes the simulated decay and propagation of simulated event products through the *BABAR* detector. `BBsim` produces an output file containing digitised hit information from each sub-detector in the form of `GHits`. The model of the *BABAR* detector in `BBsim` includes a comprehensive description of every sub-detector, and the location and materials of all active and inactive detector elements.

The simulated detector data is then processed using a package called `SimApp`. This package produces raw information in the form of `digis` from the `GHits` created by `BBsim`. These `digis` represent the detector's response simulation and are equivalent to the actual `digis` as processed by the detector electronics and readout systems. MC

data is reconstructed using a package called `Bear`, in the same way that real data is reconstructed in OPR using a package called `Elf`.

Background hits are mixed with MC simulated data during processing by `SimApp`. These background hits are not simulated. They are actual detector event samples, which have been recorded with a random trigger using a luminosity weighting factor.

When generating MC data, *truth* lists of generated event products are made. In order to fine tune analyses, reconstructed candidates from MC data can be matched to their truth partners by performing a χ^2 test on candidate specific parameters such as momenta, energy, and various geometric information.

All MC data were generated using real detector and machine conditions, ambient data, and some of the calibration constants used for the reconstruction of real data. This enables MC data to be better matched to real data from the detector. To this end, MC data were generated in two sets representing the change in the operating voltage of the DCH sense wires from 1900 V to 1960 V during the first run of the experiment.

4.4.1 Exclusive Signal MC Data

Each exclusive MC sample includes 20,000 events. Exclusive MC data were generated for each of the two modes under study and for a *calibration mode*. This information is summarised in Table 4.2. These data were used to obtain the efficiency for the selection of signal events using the chosen analysis selection variables for each mode. In addition, the exclusive MC data for the calibration mode were used to obtain efficiency correction factors that were needed due to discrepancies between MC and detector data.

4.4.2 Generic MC Data

Generic MC samples of $B\bar{B}$ and light $q\bar{q}$ events were used to investigate backgrounds in the analyses presented. These were generated as $B^0\bar{B}^0$, B^+B^-, $c\bar{c}$, and uds MC

Table 4.2: *Summary of the amounts of the exclusive signal MC data that were used in the analyses presented here. For each event, one of the B meson pair is forced to decay to the exclusive mode stated. The appropriate branching fractions were used for the secondary decays.*

Mode		Number of Events
$B^0 \to \phi K^0_S$	(Signal Mode)	20,000
$\phi \to K^+K^-, K^0_S \to \pi^+\pi^-$		
$B^0 \to K^{*+}\pi^-$	(Signal Mode)	20,000
$K^{*+} \to K^0_S\pi^+, K^0_S \to \pi^+\pi^-$		
$B^0 \to D^-\pi^+$	(Calibration Mode)	20,000
$D^- \to K^0_S\pi^-, K^0_S \to \pi^+\pi^-$		

samples, where the latter represents the combined continuum backgrounds from $u\bar{u}$, $d\bar{d}$, and $s\bar{s}$ production. Table 4.3 shows the number of events, and the equivalent integrated luminosity, which were used for each category.

4.4.3 Charmless Hadronic $B\bar{B}$ MC Data

The charmless hadronic $B\bar{B}$ MC data sample consists of a cocktail of charmless hadronic B meson decay modes. These data were used to study the amount of cross-talk from other charmless hadronic B meson decays with similar kinematics to those studied and presented here. The sample generated is equivalent to that which would exist in approximately 21 fb^{-1} of on-resonance data. The branching fractions for a number of the decays present in this sample are as yet unknown, and the upper limits on their branching fractions were therefore used to generate them. For each event, one of the B meson pair was forced to decay to a charmless hadronic final state, while the other decayed generically.

Table 4.3: *Summary of the amounts of the generic MC data that were used in the analyses presented here. The mode uds represents continuum backgrounds from $u\bar{u}$, $d\bar{d}$, and $s\bar{s}$ events.*

Mode	Number of Events ($\times 10^6$)	Equivalent Integrated Luminosity (fb^{-1})
$B^0\bar{B}^0$	2.3	5.04
B^+B^-	3.8	8.33
$c\bar{c}$	6.5	5.00
uds	11.9	5.69

4.5 Event Reconstruction and Candidate Lists

During data processing by OPR, event reconstruction is undertaken by the `Elf` package. This package processes the raw `digi` information from the sub-detectors, in order to provide reconstructed event information for analysis. `Elf` uses pattern recognition and fitting algorithms to reconstruct cluster and track *candidates*, and hence, various particle candidate lists that are made available for use in analyses. Table 4.4 summarises the candidate lists that were used in the analyses presented here, with a description of the requirements for their selection. These lists are obtained, or reconstructed at run time, from the `micro` database. Since the `Bear` package is used to reconstruct simulated MC events in the same way that `Elf` is used for real data, it produces the same candidate lists in MC data.

4.5.1 Track Reconstruction

In the SVT, clusters are reconstructed by the SVT electronics using time, position, and charge information. These clusters are made available to pattern recognition

Table 4.4: *Summary of the candidate lists that were used in the analyses presented here. These lists were obtained, or reconstructed at run time, from the* `micro` *database.*

List Name	Description and Selection Criteria
`TaggingList`	All candidates with non-zero charge and with the pion mass hypothesis assigned.
`GoodTracksLoose`	Same as `TaggingList`, but, with • at least 100 MeV of transverse momentum, • a maximum momentum of 10 GeV, • at least 12 DCH hits, • a minimum and a maximum DOCA of -10 cm and $+10$ cm, respectively, in the direction of the beam, and • a maximum DOCA of 1.5 cm perpendicular to the beam direction, where DOCA is the *distance of closest approach* to the IP.
`KsDefault`	Composite candidates reconstructed from pairs of oppositely charged tracks from the `ChargedTracks` list (same as the `TaggingList` list) using four-momentum addition, with • a reconstructed mass within ± 25 MeV of the nominal K_S^0 mass of 498 MeV [17], • a reconstructed vertex away from the IP, and • a constraint on the absolute cosine of the helicity angle of less than one.

algorithms in `Elf` for track reconstruction. In addition, drift time and integrated charge information for the DCH cells with registered hits, are feature extracted using DCH specific algorithms in the ROMs and are also used for track reconstruction and dE/dx measurements.

Online track finding and fitting is undertaken using a Kalman filter technique [48] that takes into account the distribution of materials in the detector and a full map of the magnetic field. For offline tracking, improvements are made to the L3 trigger tracking algorithm. Improved event timing, obtained from available track parameters and individual track hit information, is used to better match tracks to hits and to identify track segments for tracks that do not originate from the IP. Tracks and track segments identified in the DCH are fitted again using the Kalman filter, before a match is attempted with track segments in the SVT. For those tracks that satisfy the expected error for extrapolation between the DCH and SVT, the Kalman fit is performed once more for the whole track.

4.6 Beta Tools

Beta Tools are a set of analysis tools that are accessed through the `Beta` package and can be used for high level analysis of the reconstructed data in the `micro` database. At this stage of the analysis, there is no need to manipulate the reconstruction code in OPR. Most analyses, and all preliminary analyses, need only be concerned with the data in the `micro` database. Should the need arise, however, `Beta` does allow access to the basic reconstruction information in the `reco` database for more advanced analysis, providing a comprehensive and flexible package for multilevel analyses.

The `Beta` package provides lists of basic particle candidates, which are reconstructed during data processing, a set of *operators*, such as vertexing and four-vector addition algorithms, and geometric and kinematic *fitting tools*. Using these lists and operators, decay trees may be reconstructed for composite candidates that in turn behave as basic candidates, allowing them to be propagated through other decay trees.

Various *association tools* may be used to link mother and daughter particles in decay trees, or to associate reconstructed particles with their MC simulated truth particles. They can also be used to associate various track segments that are reconstructed in the SVT and DCH, and in turn to associate tracks with clusters in the EMC or IFR.

Particle candidates are filtered using *selectors* that make use of particle ID, and kinematic and geometric discriminators as appropriate. There are various levels of criteria for each selector, varying from *very loose* to *very tight* selections. Candidates passing each level of the selector's criteria are mapped into the appropriate candidate list for that selector and criteria.

4.7 Kinematic Constraints

As mentioned at the start of Chapter 3, the production of B mesons at the $\Upsilon(4S)$ resonance mass has several advantages. Most notably, powerful kinematic constraints are introduced into the system, which allow for the separation of signal from background in the reconstruction of B mesons. These kinematic constraints are manifest in two largely uncorrelated variables that are used to select fully reconstructed B meson candidates. Both of these variables use the energy of the beam as a constraint to veto combinatoric and continuum backgrounds.

The first of these variables is an invariant quantity known as ΔE [1]. This variable is defined as the difference between the reconstructed and the expected B meson energy, where the latter is simply the beam-energy in the centre-of-mass frame, $E^*_{\rm beam} = \sqrt{s}/2$. In its Lorentz invariant form,

$$\Delta E = \frac{p_0 \cdot p_B}{\sqrt{s}} - E^*_{\rm beam}\,, \tag{4.1}$$

where $p_B = (E_B, \vec{p}_B)$ and $p_0 = (E_0, \vec{p}_0)$ are the four-momenta of the B meson and the initial e^+e^- system, respectively.

The second variable is the mass of the reconstructed B meson, which is constrained

using the energy and momentum of the beam. This variable is known as the *beam-energy substituted mass*, $m_{\rm ES}$ [1], of the B meson and is defined by,

$$m_{\rm ES} = \sqrt{E_{\rm BC}^2 - \vec{p}_B^{\,2}}\,, \tag{4.2}$$

where the beam-energy constrained B meson energy in the laboratory frame of reference, $E_{\rm BC}$, is given by,

$$E_{\rm BC} = \frac{E_0^2 - \vec{p}_0^{\,2} + 2(\vec{p}_0 \cdot \vec{p}_B)}{2E_0}\,. \tag{4.3}$$

For the analyses presented here, both $m_{\rm ES}$ and ΔE were calculated in the laboratory frame of reference.

The total event energy and momentum, E_0 and $\vec{p}_0$, are obtained from the PEP-II environment database. The B meson momentum $\vec{p}_B$ is the sum of the momenta of its daughters. From Equations 4.2 and 4.3, it is evident that the determination of $m_{\rm ES}$ is independent of any mass hypotheses for the B meson daughters. For the determination of ΔE, however, mass hypotheses are needed for the B meson daughters in order to obtain E_B, and hence p_B in Equation 4.1.

For true reconstructed B mesons, ΔE should have a distribution centred on 0 MeV and the distribution of $m_{\rm ES}$ should be centred on the nominal B meson mass of 5.279 GeV/c^2 [17]. Figure 4.1 shows the reconstructed $m_{\rm ES}$ and ΔE distributions from signal MC and on-resonance data, for the calibration mode $B^0 \to D^-\pi^+$, where $D^- \to K_S^0\pi^-$. The discrepancies between MC and detector data can be seen in the differences between the fits to these $m_{\rm ES}$ and ΔE distributions. The shift in the mean and the change in the width of each distribution are used to obtain correction factors for the signal efficiency, which is obtained from the signal MC for each mode.

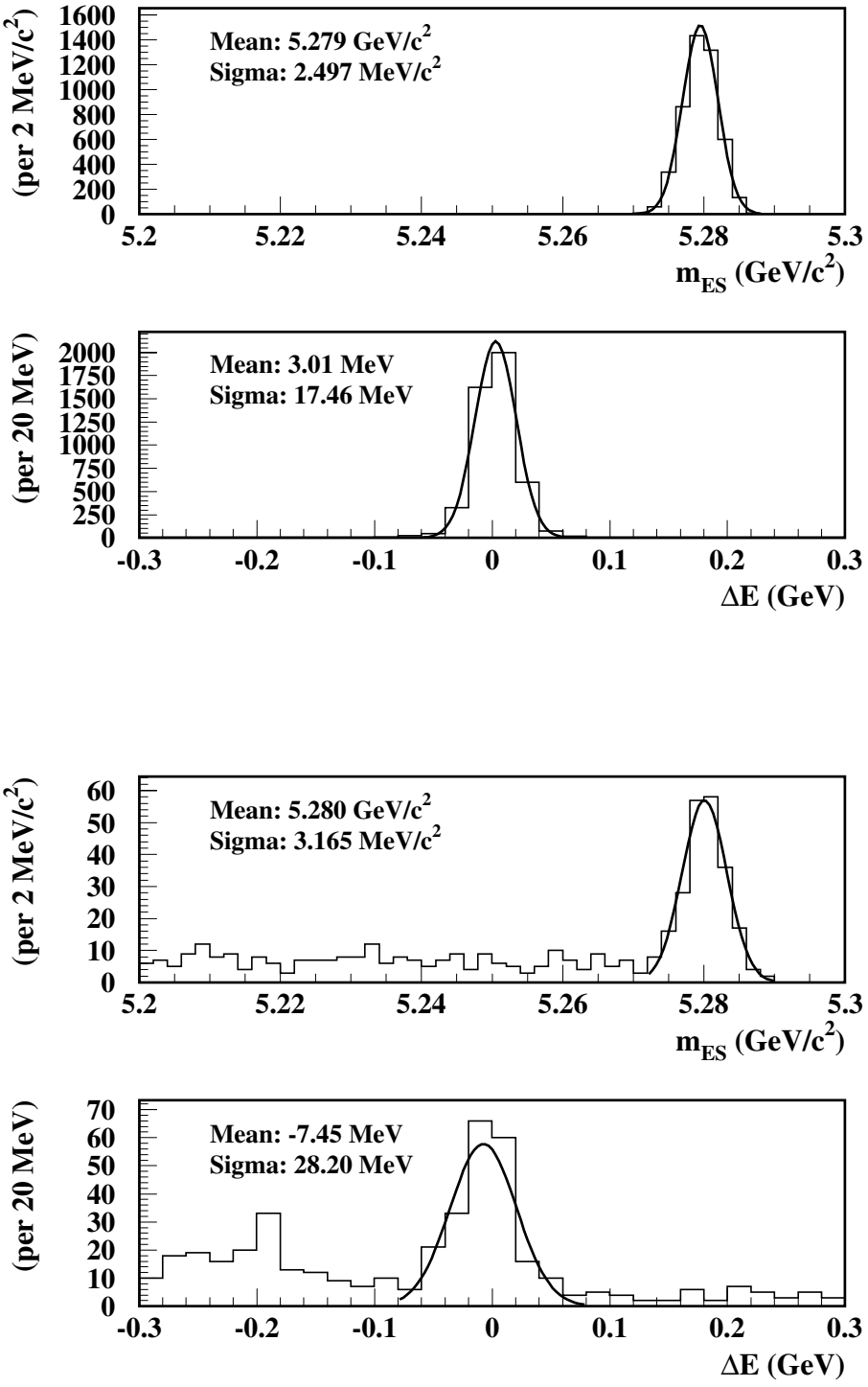

Figure 4.1: *The m_{ES} and ΔE distributions from signal MC (top) and on-resonance data (bottom), for reconstructed B mesons from the decay $B^0 \to D^-\pi^+$, where $D^- \to K^0_S\pi^-$. All distributions have been fitted with a single Gaussian.*

4.8 Data Skims and Ntuple Production

4.8.1 Data Skims

The `BCCKs3body` skim was produced during data processing by OPR using the `B3bodyTagFilter` module in the `FilterTools` package. This module requires that there be at least four tracks from the `TaggingList` for each event, and that the total energy of the event is less than 20 GeV. In addition, `B3bodyTagFilter` requires that the `BCCKs3body` tag bit be set in the `TagB3body` module of the `EventTagTools` package.

In order to set the `BCCKs3body` tag bit, B^0 meson candidates are reconstructed in the `TagB3body` module by four-momenta addition of all the combinations of two tracks from the `GoodTracksLoose` list and a K^0_S meson from the `KsDefault` list of candidates. Both combinations of pion and kaon mass hypotheses are set for the tracks used. Events are selected if the two tracks are oppositely charged. In addition, the $m_{\rm ES}$ of the reconstructed B mesons must be within 100 MeV of the centre-of-mass beam-energy limit $\sqrt{s}/2$, and the absolute value of ΔE must be less than 450 MeV.

4.8.2 Three-Body Ntuple Production Using Beta Tools

After the data have been skimmed by OPR and archived to the Objectivity database, they are available for analysis using the Beta Tools in the `Beta` analysis environment. For the three-body analyses presented here, a collection of modules in the `NonCharm3BodyUser` Beta package were used for the production of Ntuples. Ntuple data files are specially formatted flat files that contain vectors of variables and their values. These Ntuples can be used in high level analyses using software such as the PAW package [44]. In this scheme, the data contained in the Ntuples are manipulated using kumac macros, which in turn use dedicated Fortran routines.

In the Ntuple production process, B meson candidates are reconstructed and selected using selection cut variables with very loose criteria. For the analyses presented here,

Ntuples were produced for the study of three-body decay modes with an intermediate single resonance, where $B^0 \to RH$, where H can be a charged pion or kaon, or a K^0_S meson, and R is the intermediate resonance that decays as $R \to h^{\pm}K^0_S$ or $h^{\pm}h^{\mp}$, where h can be a pion or kaon. The same Ntuples can be used for non-resonant decays, where $B^0 \to h^{\pm}h^{\mp}K^0_S$, where again h can be a pion or kaon. Only one of the three daughters of the B^0 mesons in these Ntuples is a K^0_S meson.

For the study of the decays with the intermediate single resonance, information on the composite resonant particles that are reconstructed from various combinations of two of the three final state daughters, is made available in the Ntuples. This information includes the mass and the cosine of the helicity angle, $\cos\theta_{\rm H}$, of the resonant particles. The helicity angle $\theta_{\rm H}$, is the angle between the direction of flight of the B meson and the direction of decay of the daughters of the resonant particle in its rest frame.

In addition to the track multiplicity and kinematic selection criteria applied at the data skimming stage, vertexing and kinematic fitting of the B meson daughters were undertaken during Ntuple production. The charged track daughters of the reconstructed B mesons were vertexed using the `BtaFastVertexer` algorithm with a $\chi^2 < 200$ vertex fit constraint. The `GeoKin` fitter was then used to produce B meson candidates with fitted daughters.

Over 200 variables are written into the Ntuples. The `B03bodyCCKs` module, which inherits from the `B3bodyBase` class in the `NonCharm3BodyUser` package, writes a number of variables specific to the decays of B mesons to two charged tracks and a K^0_S candidate, including information on the possible intermediate resonances. Other variables, including details of the B meson candidates and their daughters, event shape information, and results of the particle ID selectors, are calculated or obtained, and written out by the `B3bodyBase` module.

Ntuples are archived to disc for all analyses that require the final three-body states that they contain. User defined selection cut variables can then be applied to the various Ntuple variables for specific analyses.

Chapter 5

Charmless Three-Body Analyses

5.1 Introduction

The analyses of the two rare charmless hadronic B meson decays presented here are *cut and count* analyses. In this scheme, a set of selection variables are chosen for the selection of reconstructed B mesons decaying to the mode of interest. The selection variables used here are typical of those used in the studies of charmless hadronic B meson decays at *BABAR* and elsewhere [49, 50, 51, 52, 53].

Event shape variables were used to discriminate against continuum backgrounds, which are the major source of background in these analyses. In addition, particle ID selectors were used for the separation of pions and kaons, in order to reduce the combinatoric backgrounds caused by the misidentification of these high multiplicity products. For the three-body analyses presented here, two selection cuts were used to distinguish the single intermediate resonance. The first selection was on the mass of the resonance, and the second on its polarised decay geometry, since the K^{*+} and ϕ resonances are both vector mesons. K^0_S mesons were selected by their resonant mass distributions and the significance of the measurement of their flight lengths.

A *blind* analysis technique was used in these analyses. This means that the number of events in the signal region was not counted, nor the $m_{\rm ES}$ or ΔE signal distributions

observed, until the selection cut values of the selection variables had been optimised to give the best *significance* for the measurement of the branching fraction for each analysis. This method of analysis reduces the risk of any bias in the determination of the selection cut value of each of the selection variables, which may be introduced by observing the distribution of events in and around the signal region while tuning the selection cut values. The distribution of events in the $m_{\rm ES}$-ΔE plane is kept hidden until the selection cut value of each of the selection variables has been optimised and the analyses are tuned and ready for *unblinding*.

A calibration mode was used to investigate any inconsistencies between on-resonance data and the signal MC used for the estimation of the signal efficiency for these analyses. Correction factors for the signal efficiencies were obtained from discrepancies between the $m_{\rm ES}$ and ΔE distributions from the signal MC of the calibration mode, and those obtained from on-resonance data for the calibration mode. These correction factors were then applied to the signal efficiencies that were obtained from the signal MC for the two modes studied. The calibration mode used for this purpose was the mode $B^0 \to D^-\pi^+$, where $D^- \to K^0_S\pi^-$. This mode has two charged tracks and a K^0_S meson in its final state, and is therefore a close match to the final states studied here.

5.2 Event Shape Variables

The primary source of background for charmless hadronic B meson decays is from continuum events from $u\bar{u}$, $d\bar{d}$, $c\bar{c}$, and $s\bar{s}$ production. The distinctive decay topology of $B\bar{B}$ events produced at the $\Upsilon(4S)$ resonance, provides powerful tools in the form of event shape variables for the rejection of these jet-like $q\bar{q}$ continuum events.

In the centre-of-mass system, $B\bar{B}$ events produced at the $\Upsilon(4S)$ threshold decay nearly at rest. This results in a spherical decay topology for true $B\bar{B}$ events, while continuum event products from light quark pair production are ejected from the IP in jets, the directions of which are highly correlated.

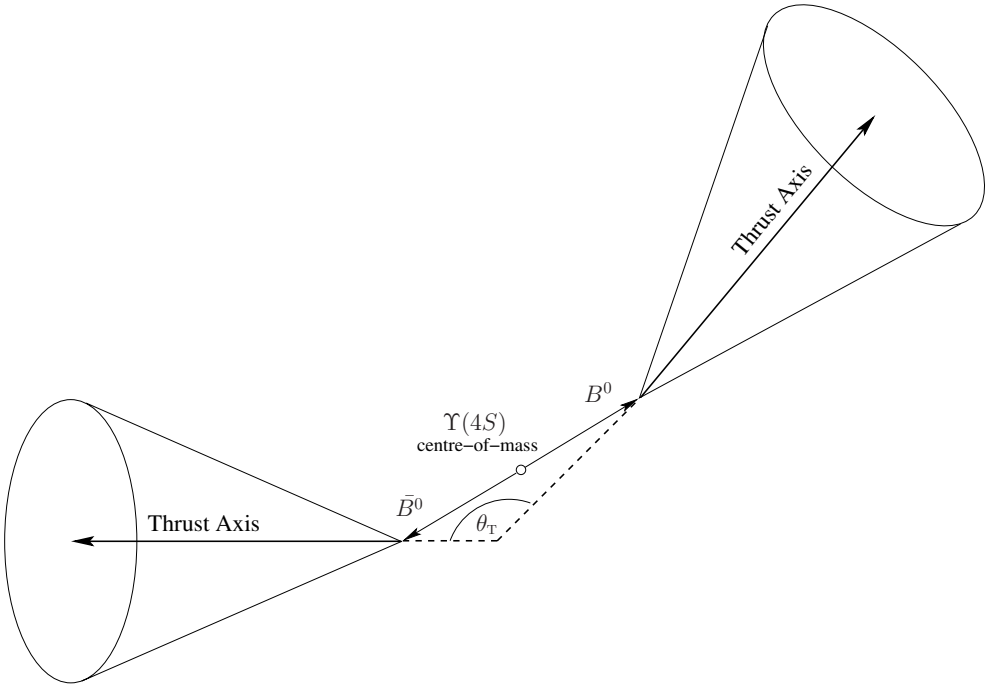

Figure 5.1: *The thrust angle θ_T is shown as the angle between the thrust axis of a reconstructed B meson and that of the rest of the event, presumed to be the thrust axis of the $\bar{B}$ meson, in the centre-of-mass system of the $\Upsilon(4S)$. In this frame of reference, the $B\bar{B}$ meson pair decay nearly at rest, whereas continuum events from light $q\bar{q}$ pair production are ejected in correlated back-to-back jets.*

5.2.1 Thrust Angle Variable

The thrust angle θ_{T} is defined in the centre-of-mass system of the $\Upsilon(4S)$. It is the angle between the direction of the thrust of a reconstructed B meson and that of the rest of the event, as shown in Figure 5.1. The thrust of the B meson is the axis that maximises the sum of the momenta of the B meson daughters. For the rest of the event, the thrust axis is defined for all track and neutral candidates not used in the reconstruction of the B meson candidate.

The cosine of the thrust angle, $\cos\theta_{\mathrm{T}}$, has a flat distribution for true $B\bar{B}$ pair events due to the spherical nature of their decay topology in the centre-of-mass system, as a result of their decay nearly at rest. In the same frame of reference, this distribution

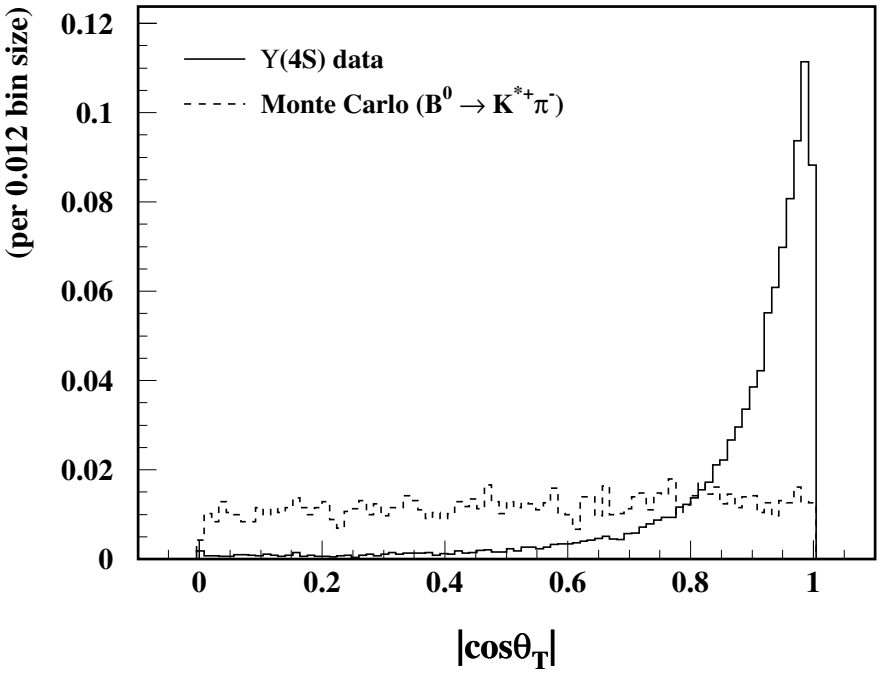

Figure 5.2: *Comparison between the* $|\cos\theta_T|$ *distribution from the* $B^0 \to K^{*+}\pi^-$ *signal MC, where* $K^{*+} \to K^0_S\pi^+$*, and that obtained from on-resonance data, from the* `BCCKs3body` *skim. This comparison illustrates the difference between the signal distribution and that from the background dominated* $\Upsilon(4S)$ *data. A nominal cut at 0.8 would allow good separation between the signal events (*< 0.8*) and background events (*> 0.8*). The selection variables used to produce these plots are listed in Table 5.1. The distributions have been normalised to one in order to show their relative shapes.*

is peaked at ± 1 for jet-like continuum events due to the high correlation between the directions of the jets, which are back-to-back.

Figure 5.2 shows a comparison between the $|\cos\theta_{\rm T}|$ distribution from the $B^0 \to K^{*+}\pi^-$ signal MC, where $K^{*+} \to K^0_S\pi^+$, and that obtained from on-resonance data, from the `BCCKs3body` skim. The selection variables used to produce these plots are listed in Table 5.1. These selection variables are described later in this chapter.

Table 5.1: *Selection variables used to produce the* $|\cos\theta_T|$ *and Fisher discriminant distributions in Figures 5.2 and 5.4, respectively, for the mode* $B^0 \to K^{*+}\pi^-$, *where* $K^{*+} \to K^0_S\pi^+$.

Selection Variable	Cut Value
π meson particle ID	not `tight` kaon selection
K^0_S meson mass	498 ± 8 MeV/c^2
K^0_S meson flight length $c\tau/\sigma_{c\tau}$	> 10.0
K^{*+} meson mass	892 ± 100 MeV/c^2
K^{*+} meson helicity angle $\lvert\cos\theta_{\rm H}\rvert$	> 0.5

5.2.2 Fisher Discriminant Variable

The Fisher discriminant variable [51] is a linear sum of a set of n weighted selection variables. It is given by,

$$\mathcal{F} = \sum_{i=1}^{n} \alpha_i x_i \,, \tag{5.1}$$

where x_i is the point distribution function (PDF) of the selection variable i, and α_i is the chosen weight for that variable. The weights are chosen in order to maximise a χ^2 for the separation between the Fisher discriminant distributions in signal and in background, as shown by,

$$\chi^2 = \frac{(\bar{\mathcal{F}}_{\rm signal} - \bar{\mathcal{F}}_{\rm background})^2}{\sigma^2_{\rm signal} - \sigma^2_{\rm background}} \,, \tag{5.2}$$

where $\bar{\mathcal{F}}$ is the mean of the fisher distribution, and σ is the width for that distribution. The signal distributions of the weighted selection variables are obtained from signal MC, while the background distributions may be obtained from off-resonance data, or

generic continuum MC.

The χ^2 is maximised by,

$$\frac{\partial \chi^2}{\partial \alpha} = 0\,, \tag{5.3}$$

resulting in the analytic solution,

$$\alpha_i = \sum_{j=1}^{n} (U_{ij}^{\text{background}} + U_{ij}^{\text{signal}})^{-1} (\mu_j^{\text{background}} - \mu_j^{\text{signal}})\,, \tag{5.4}$$

where U_{ij} are the covariance error matrices of the set of selection variables and give the correlation between them, and μ_j is the mean of the PDF of the selection variable j.

The Fisher discriminant used in the analyses presented here is a linear sum of eleven weighted variables in the laboratory frame of reference. These include,

- the cosine of the angle between the thrust axis of the B meson and the beam axis,
- the cosine of the angle between the decay axis of the B meson and the beam axis, where the decay axis is the direction of flight of the B meson, and
- the summed energy of the rest of the event that is contained within each of nine concentric energy cones about the thrust axis of the B meson. Figure 5.3 shows that the angle of each successive energy cone increases by 10° with respect to the thrust axis of the B meson. The cones cover both halves of the event, that containing the reconstructed B meson, and the opposite half.

A comparison between the Fisher discriminant distribution from the $B^0 \to K^{*+}\pi^-$ signal MC, where $K^{*+} \to K_S^0\pi^+$, and that obtained from on-resonance data, from the `BCCKs3body` skim, is shown in Figure 5.4. The selection variables used to produce these plots are listed in Table 5.1. Note that, no selection was made on the thrust angle variable $|\cos\theta_{\rm T}|$.

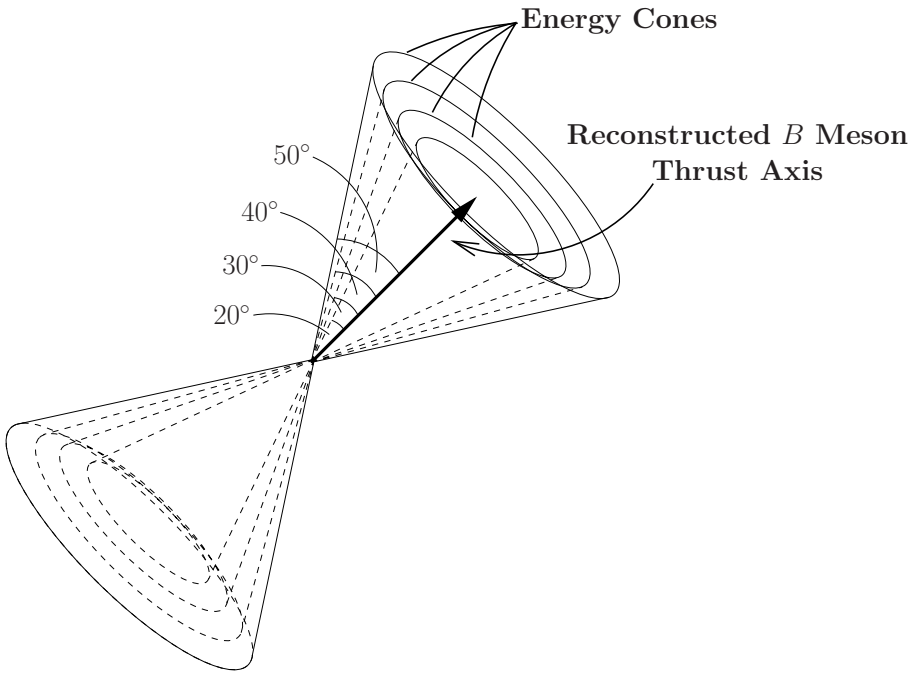

Figure 5.3: *The thrust axis of the reconstructed B meson in the laboratory frame of reference, showing the relation of the second through fifth Fisher discriminant energy cones each containing the summed energy of the rest of the event in that cone.*

The weights for the summed variables in the Fisher discriminant were tuned to provide maximum separation between signal and background for the analysis of the charmless hadronic ωh modes, where h is a kaon or pion. Although not explicitly tuned for the analyses presented here, this Fisher discriminant was found to provide extra discrimination against continuum backgrounds after the application of the trust angle selection $|\cos\theta_{\rm T}|$.

5.3 Selection of π and K Mesons

The particle ID criteria for the two tracks in the final state of the analyses presented here were made available in the Ntuples. The choice of the particle ID selection criteria was optimised to give the best significance for the measurements of the branching fractions. The `PidKaonSMSSelector` kaon selector was used to categorise the particle

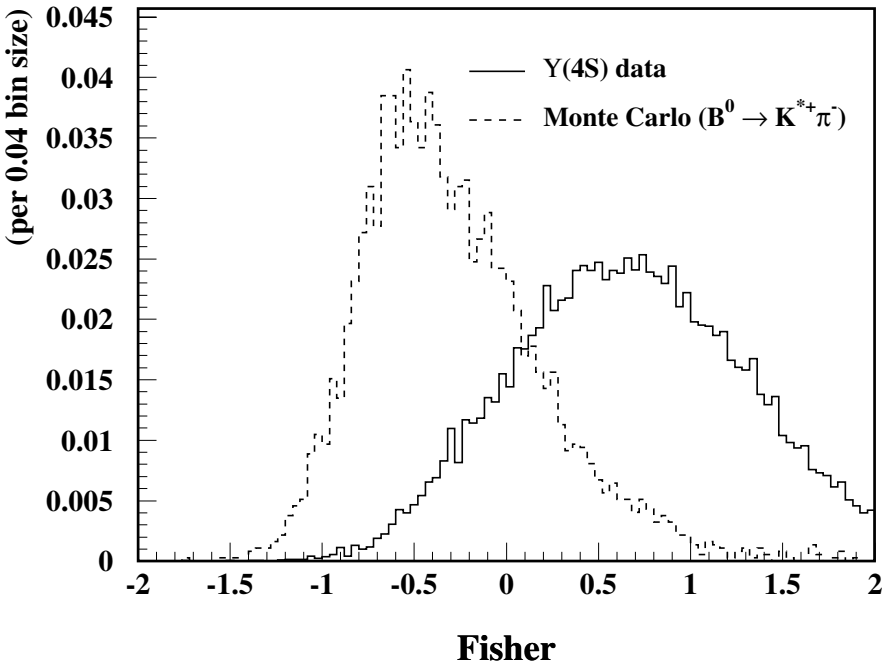

Figure 5.4: *Comparison between the Fisher discriminant distribution from the* $B^0 \to K^{*+}\pi^-$ *signal MC, where* $K^{*+} \to K^0_S\pi^+$*, and that obtained from on-resonance data, from the* `BCCKs3body` *skim. This comparison illustrates the difference between the signal distribution and that from the background dominated* $\Upsilon(4S)$ *data. A nominal cut at 0.0 would allow good separation between the signal events (*< 0.0*) and background events (*> 0.0*). The selection variables used to produce these plots are listed in Table 5.1. The distributions have been normalised to one in order to show their relative shapes.*

ID criteria for the two tracks. The kaon selection criteria studied were, `tight`, `loose`, `veryLoose`, and the `notApion` criteria.

These kaon selections are based on a likelihood calculation method, which uses particle ID information from the SVT, DCH, and DIRC sub-detectors [54]. In order for a track to be considered for identification by any of these sub-detectors, certain momentum dependent requirements must be satisfied for each sub-detector. Table 5.2 summarises

Table 5.2: *Summary of the momentum dependent sub-detector requirements for particle ID information from the SVT, DCH, and DIRC sub-detectors.*

Sub-detector	Momentum Range (GeV/c)	Specific Requirements
SVT	$0.025 < p < 0.7$	Three or more dE/dx measurements.
DCH	$0.090 < p < 0.7$	Ten or more dE/dx measurements.
DIRC	$0.090 < p < 10.0$	One or more expected Cherenkov photons for the e^- hypothesis.

these requirements.

Each of the selector's criteria have been optimised for a particular kaon identification, or pion misidentification threshold. Table 5.3 summarises the particle ID criteria for the kaon selections used in the analyses presented here, with the requirements for each criteria. The sub-detector specific momentum range needs to be satisfied for information from that sub-detector to be used. The ratios r_π and r_p are the pion-to-kaon and proton-to-kaon ratios, respectively, for the average number of inclusive pions, protons, and kaons per event. These ratios are determined using a log likelihood difference between the pions, or protons, and the kaons [54].

Figure 5.5 shows the effect of the application of the `tight` kaon particle ID selection on the tracks used for the reconstruction of ϕ mesons, on the ϕ meson mass distribution. It is obvious that this is a powerful selection for the reduction of combinatoric backgrounds due to misidentified kaons, while retaining the greater part of the ϕ signal.

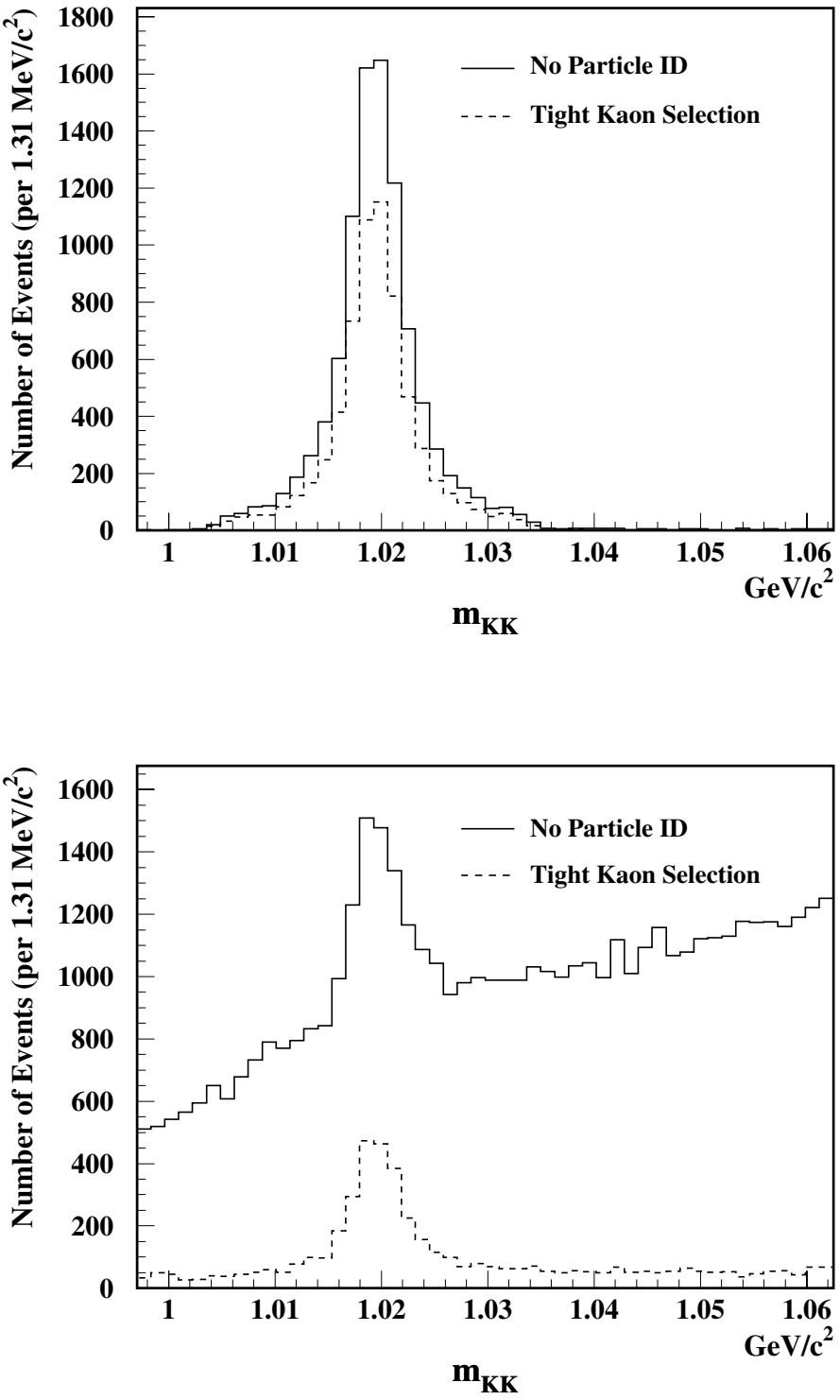

Figure 5.5: *The effect of the application of the* `tight` *kaon particle ID selection to tracks, on the mass distributions of ϕ mesons reconstructed from $\phi \to K^+K^-$. The effect is shown on distributions from the $B^0 \to \phi K^0_S$ signal MC (top), where $K^0_S \to \pi^+\pi^-$, and that obtained from on-resonance data (bottom), from the* `BCCKs3body` *skim.*

Table 5.3: *Summary of the* `PidKaonSMSSelector` *particle ID criteria for the kaon selections used in the analyses presented here. The ratios r_π and r_p are the pion-to-kaon and proton-to-kaon ratios, respectively. l_K, l_π, and l_p are the likelihoods for kaons, pions, and protons, respectively.*

Criteria for Kaon Selection	Momentum Range (GeV/c)	Selection Criteria r_π and r_p	Selection Likelihood
`tight`	SVT, $p < 0.7$ DCH, $p < 0.7$ DIRC, $p > 0.6$	$0.5 < p < 0.7$: $r_\pi = 15$, $r_p = 1$ $p > 2.7$: $r_\pi = 80$, $r_p = 1$ $p < 2.7$: $r_\pi = 1$, $r_p = 1$	$l_K > r_\pi l_\pi$ $l_K > r_p l_p$
`notApion`	SVT, $p < 0.5$ DCH, $p < 0.6$ DIRC, $p > 0.6$	$p \leq 0.5$: $r_\pi = 0.1$, $r_p = 1$ $p > 0.5$: $r_\pi = 1$, $r_p = 1$	$l_K > r_\pi l_\pi$ $l_p > r_\pi l_\pi$

5.4 Selection of K_S^0 Mesons

For the analyses presented here, K_S^0 mesons were reconstructed from the decay $K_S^0 \to \pi^+\pi^-$. This mode has a branching fraction of $\mathcal{B}(K_S^0 \to \pi^+\pi^-) = 0.686 \pm 0.003$ [17]. This secondary branching fraction was taken into account for the measurement of the branching fractions for the modes studied here.

As indicated in Section 4.5, K_S^0 mesons were obtained from the `KsDefault` list, which is created at run-time from the track candidate lists available in the `micro` level of the database. Table 4.4 described the selection criteria for the reconstructed K_S^0 mesons in this list.

In addition to the criteria required for the production of the `KsDefault` list, a further two selections were made in order to veto combinatoric backgrounds in the selection

Table 5.4: *Selection variables used to produce the $c\tau/\sigma_{c\tau}$ distributions in Figure 5.7, for the mode $B^0 \to K^{*+}\pi^-$, where $K^{*+} \to K^0_S\pi^+$.*

Selection Variable	Cut Value
Thrust angle $\lvert\cos\theta_{\rm T}\rvert$	< 0.8
Fisher discriminant	< 0.0
π meson particle ID	not `tight` kaon selection
K^0_S meson mass	498 ± 8 MeV/c^2
K^{*+} meson mass	892 ± 100 MeV/c^2
K^{*+} meson helicity angle $\lvert\cos\theta_{\rm H}\rvert$	> 0.5

of K^0_S mesons. The first of these was a standard ± 8 MeV/c^2 cut on the nominal K^0_S meson mass of 498 MeV/c^2 [17]. The mass distributions of reconstructed K^0_S mesons from the $B^0 \to K^{*+}\pi^-$ signal MC, where $K^{*+} \to K^0_S\pi^+$, and that obtained from on-resonance and off-resonance data, from the `BCCKs3body` skim, are shown in Figure 5.6. These distributions are taken directly from the Ntuples and no additional selections have been applied.

The second selection on the K^0_S meson sample was a cut on the significance of the measurement of the K^0_S meson flight length, $c\tau/\sigma_{c\tau}$, where c is the speed of light, τ is the measured lifetime of the K^0_S meson, and $\sigma_{c\tau}$ is the error on the measurement of the quantity $c\tau$. The distributions of $c\tau/\sigma_{c\tau}$ from the $B^0 \to K^{*+}\pi^-$ signal MC, where $K^{*+} \to K^0_S\pi^+$, and from on-resonance data, from the `BCCKs3body` skim, are shown in Figure 5.7. The selection variables used to produce these plots are listed in Table 5.4. The large spike close to zero in the distribution from on-resonance data, indicates a large number of K^0_S candidates with flight length measurements of low significance that need to be vetoed.

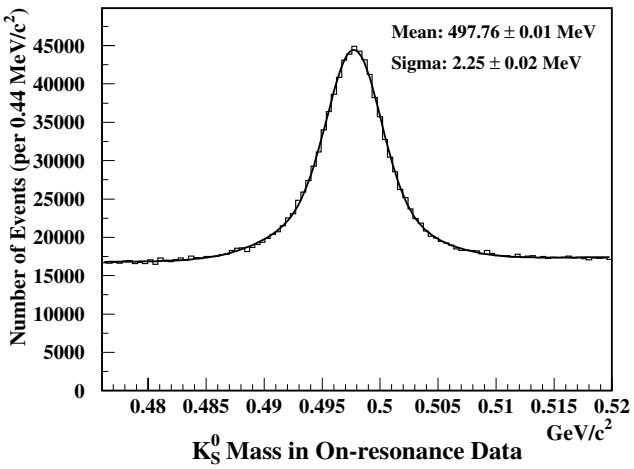

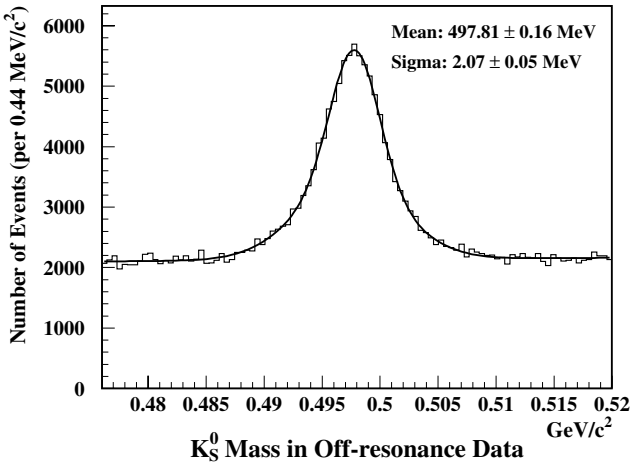

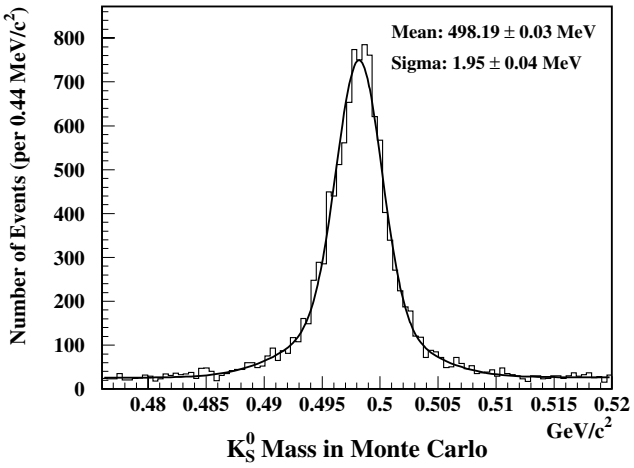

Figure 5.6: *K_S^0 meson mass distributions from on-resonance data (top), off-resonance data (middle), and from the $B^0 \to K^{*+}\pi^-$ signal MC (bottom). The distributions have been fitted with a combination of a double Gaussian and a third order polynomial. The quoted mean and sigma are for the core Gaussian in each case.*

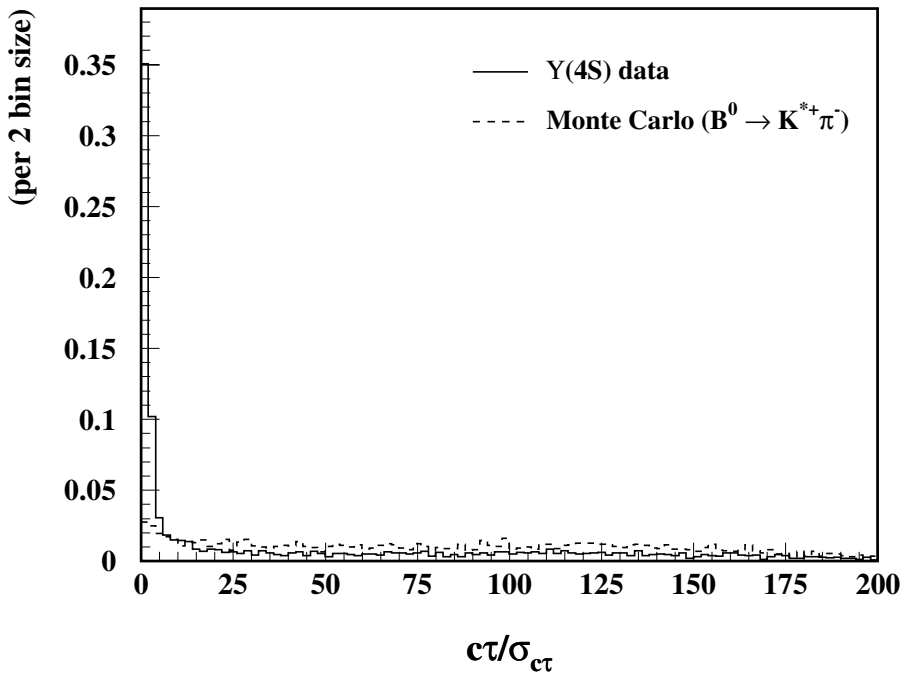

Figure 5.7: *Comparison between the $c\tau/\sigma_{c\tau}$ distribution from the $B^0 \to K^{*+}\pi^-$ signal MC, where $K^{*+} \to K^0_S\pi^+$, and that obtained from on-resonance data, from the* `BCCKs3body` *skim. This comparison illustrates the difference between the signal distribution and that from the background dominated $\Upsilon(4S)$ data. The latter has a large spike close to zero due to fake K^0_S candidates. A nominal cut at 5.0 would allow good separation between the signal events (> 5.0) and background events (< 5.0). The selection variables used to produce these plots are listed in Table 5.4. The distributions have been normalised to one in order to show their relative shapes.*

A comparison between the mass distribution of K^0_S mesons from the $B^0 \to K^{*+}\pi^-$ signal MC, where $K^{*+} \to K^0_S\pi^+$, and that obtained from on-resonance data, from the `BCCKs3body` skim, is shown in Figure 5.8 for a selection of $c\tau/\sigma_{c\tau} > 10.0$. The effect of varying the value of the $c\tau/\sigma_{c\tau}$ selection on the K^0_S mass distribution, can be seen in Figure 5.9 for the $B^0 \to K^{*+}\pi^-$ signal MC, where $K^{*+} \to K^0_S\pi^+$, and for on-resonance data.

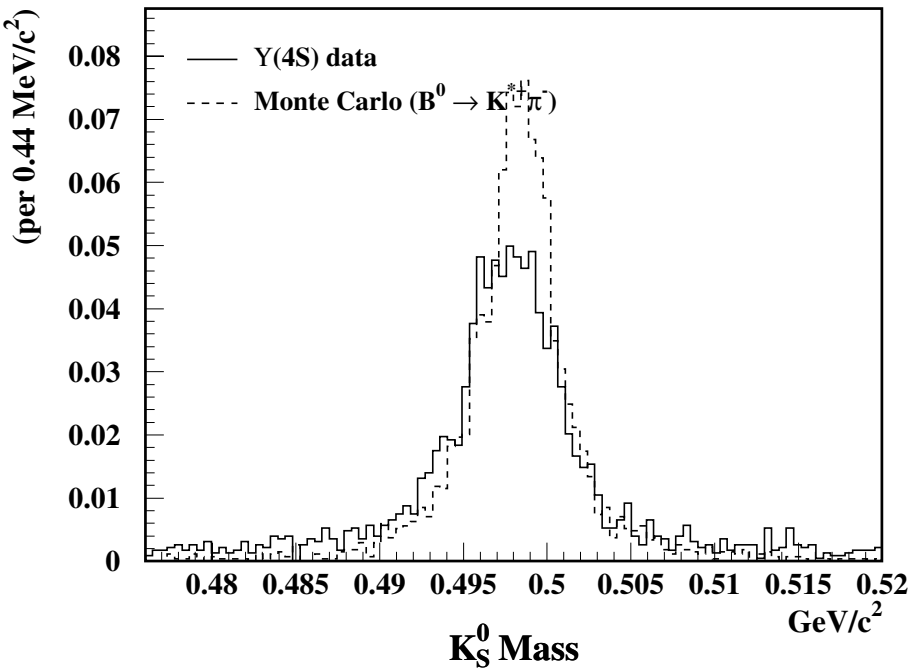

Figure 5.8: *Comparison between the K^0_S meson mass distribution from the $B^0 \to K^{*+}\pi^-$ signal MC, where $K^{*+} \to K^0_S\pi^+$, and that obtained from on-resonance data, from the* `BCCKs3body` *skim, showing the K^0_S meson mass peak in both. A standard 498 ± 8 MeV/c^2 mass cut was made in the analyses presented here, in order to veto the background in the tails of these distributions. The selection variables used to produce these plots are listed in Table 5.4, except that a selection cut of $c\tau/\sigma_{c\tau} > 10.0$ was made in place of the K^0_S meson mass selection. The distributions have been normalised to one in order to show their relative shapes.*

5.5 Selection of ϕ Mesons

For the study of the $B^0 \to \phi K^0_S$ mode, ϕ mesons were reconstructed from the decay $\phi \to K^+K^-$ during Ntuple production. This mode has a branching fraction of $\mathcal{B}(\phi \to K^+K^-) = 0.492 \pm 0.007$ [17]. This secondary branching fraction was taken into account for the measurement of the branching fraction for the $B^0 \to \phi K^0_S$ mode.

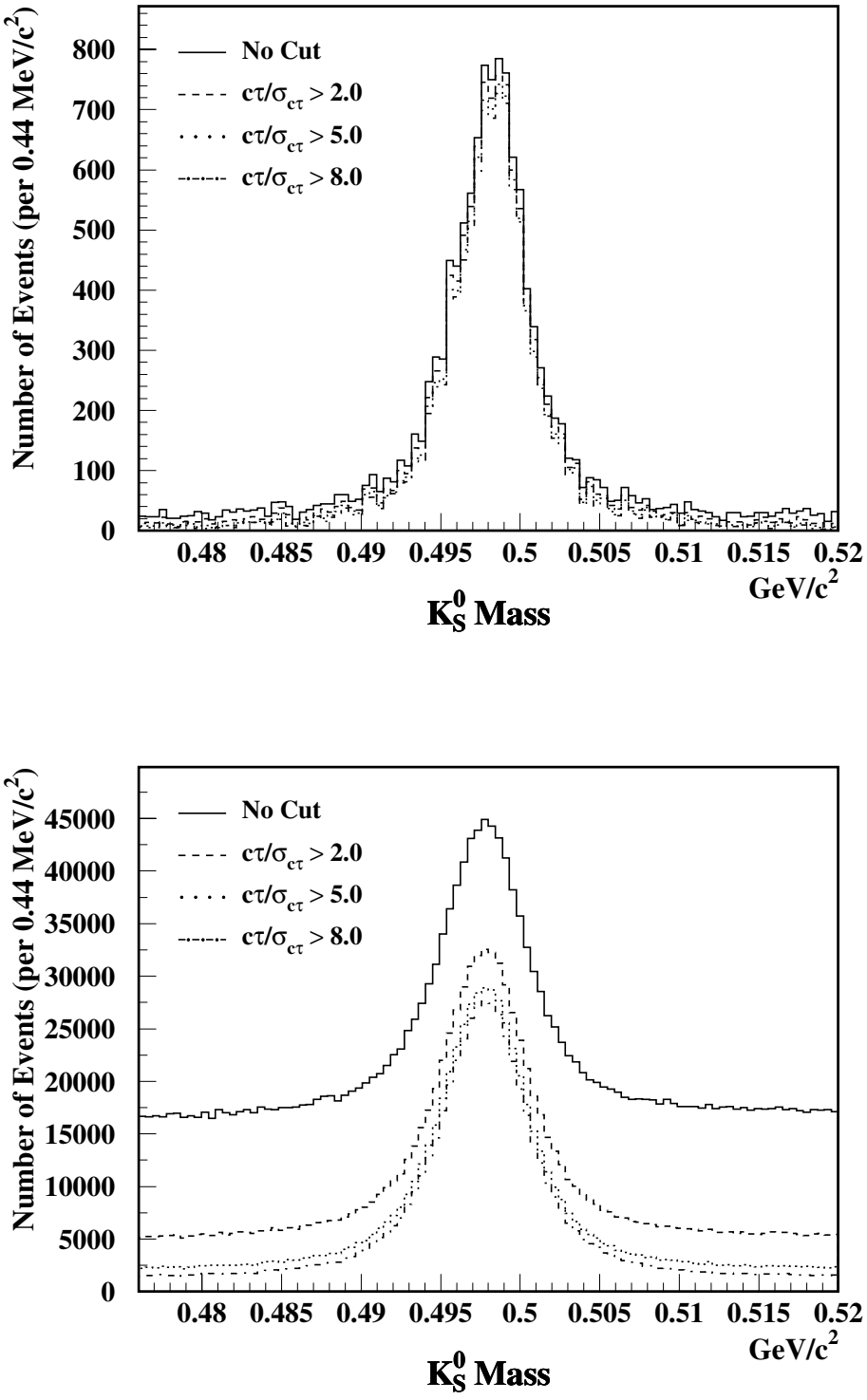

Figure 5.9: *The effect of successively tighter $c\tau/\sigma_{c\tau}$ selection cuts is shown on the mass distributions of reconstructed K^0_S mesons from the $B^0 \to K^{*+}\pi^-$ signal MC (top), where $K^{*+} \to K^0_S\pi^+$, and from on-resonance data (bottom), from the* `BCCKs3body` *skim.*

Table 5.5: *Selection variables used to produce the ϕ meson mass distributions in Figure 5.10, for the $B^0 \to \phi K^0_S$ mode.*

Selection Variable	Cut Value
Thrust angle $\lvert\cos\theta_{\rm T}\rvert$	< 0.9
Fisher discriminant	< 0.2
K meson particle ID	`notApion` kaon selection
K^0_S meson mass	498 ± 8 MeV/c^2
K^0_S meson flight length $c\tau/\sigma_{c\tau}$	> 10.0
ϕ meson helicity angle $\lvert\cos\theta_{\rm H}\rvert$	> 0.2

For each event, all combinations of two oppositely charged tracks from those entered into the Ntuples, were used for the reconstruction of ϕ meson candidates. The two tracks were vertexed using the `BtaFastVertexer` algorithm. Subsequently, the `notApion` kaon selection criteria was applied to both tracks. This kaon selection criteria was chosen as a result of an optimisation process, which was carried out in order to obtain the highest significance for the measurement of the branching fraction for the $B^0 \to \phi K^0_S$ mode.

The resonant mass distribution of ϕ mesons has a very narrow Breit-Wigner width of $\Gamma = 4.26 \pm 0.05$ MeV/c^2 [17]. A selection on the nominal ϕ meson mass of 1020 MeV/c^2 [17], allows very good separation of the ϕ meson signal from combinatoric backgrounds. This selection was applied and the cut was varied between 1020 ± 10 MeV/c^2 and 1020 ± 20 MeV/c^2, in order to obtain the highest significance for the measurement of the $B^0 \to \phi K^0_S$ branching fraction. The mass distributions of the reconstructed ϕ mesons from the $B^0 \to \phi K^0_S$ signal MC, where $\phi \to K^+K^-$, and from on-resonance data, from the `BCCKs3body` skim, are shown in Figure 5.10. The selection variables used to produce these plots are listed in Table 5.5.

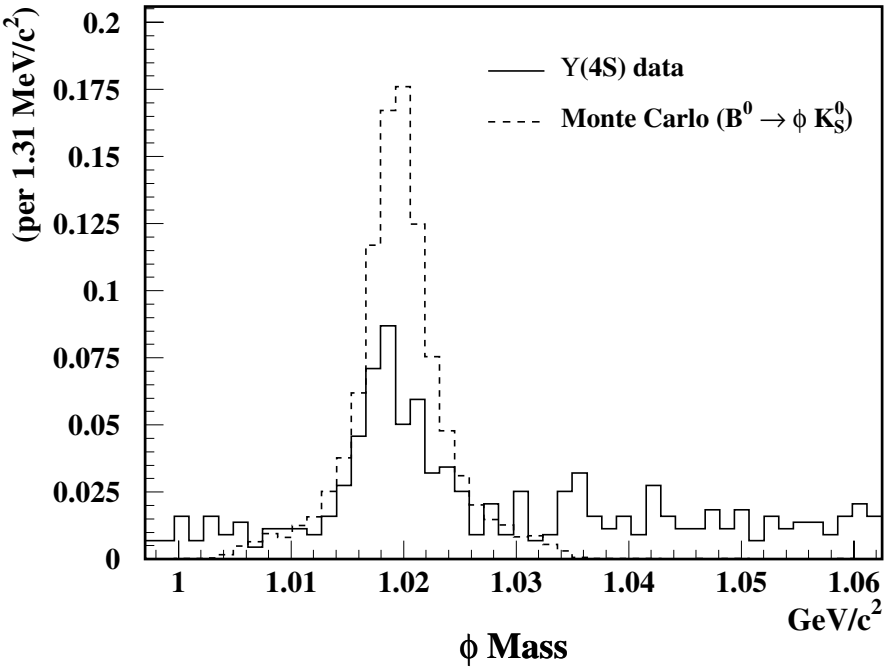

Figure 5.10: *Comparison between the ϕ meson mass distribution from the $B^0 \to \phi K^0_S$ signal MC, and that obtained from on-resonance data, from the* `BCCKs3body` *skim, showing the ϕ meson mass peak in both. A nominal 1020 ± 15 MeV/c^2 mass cut would veto the background in the tails of these distributions. The selection variables used to produce these plots are listed in Table 5.5. The distributions have been normalised to one in order to show their relative shapes.*

In its rest frame, the ϕ meson decays to two back-to-back kaons. Since it is a vector meson with a spin of one, it has a preferential decay topology. That is, the decay axis of the kaons is preferentially aligned with the momentum vector of the parent B meson in the ϕ rest frame. This leads to a *helicity* distribution that is used to further veto combinatoric backgrounds in the selection of ϕ mesons. The angle between the direction of flight of the B meson and the decay axis of the two kaons, in the ϕ rest frame, is known as the *helicity angle* $\theta_{\rm H}$ of the ϕ meson decay and is shown in Figure 5.11. A selection on the absolute value of the cosine of the helicity angle, $\cos\theta_{\rm H}$, is used

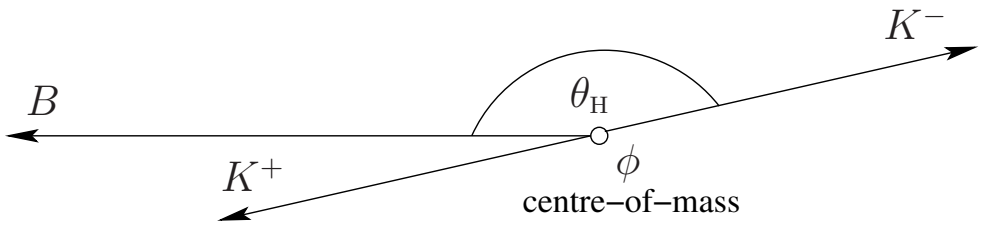

Figure 5.11: *The helicity angle θ_H is shown as the angle between the direction of flight of a reconstructed B meson and the decay axis of the two kaons from its daughter ϕ meson, in the rest frame of the latter. For a vector meson with a spin of one, such as the ϕ meson, the decay axis of its daughters is preferentially aligned with the momentum vector of the parent B meson in the rest frame of the vector meson.*

to separate signal from background in the selection of ϕ mesons. Figure 5.12 shows that the $|\cos\theta_{\rm H}|$ distribution is peaked towards +1 for ϕ mesons from the $B^0 \to \phi K^0_S$ signal MC, while for the on-resonance data it is mostly flat.

5.6 Selection of K^{*+} Mesons

For the study of the $B^0 \to K^{*+}\pi^-$ mode, K^{*+} mesons were reconstructed from the decay $K^{*+} \to K^0_S\pi^+$ during Ntuple production. This mode has a total branching fraction of 1/3, from $\mathcal{B}(K^{*+} \to K^0\pi^+) = 2/3$ and $\mathcal{B}(K^0 \to K^0_S) = 1/2$. This secondary branching fraction was taken into account for the measurement of the branching fraction for the $B^0 \to K^{*+}\pi^-$ mode.

For each event, all combinations of a K^0_S meson and a track from those entered into the Ntuples, were used for the reconstruction of the K^{*+} meson candidates. For the selection of pions, particle ID selection was applied to both tracks by vetoing the `tight` kaon selection criteria for each track. This particle ID selection is a loose pion selection and was chosen as a result of an optimisation process that was carried out in

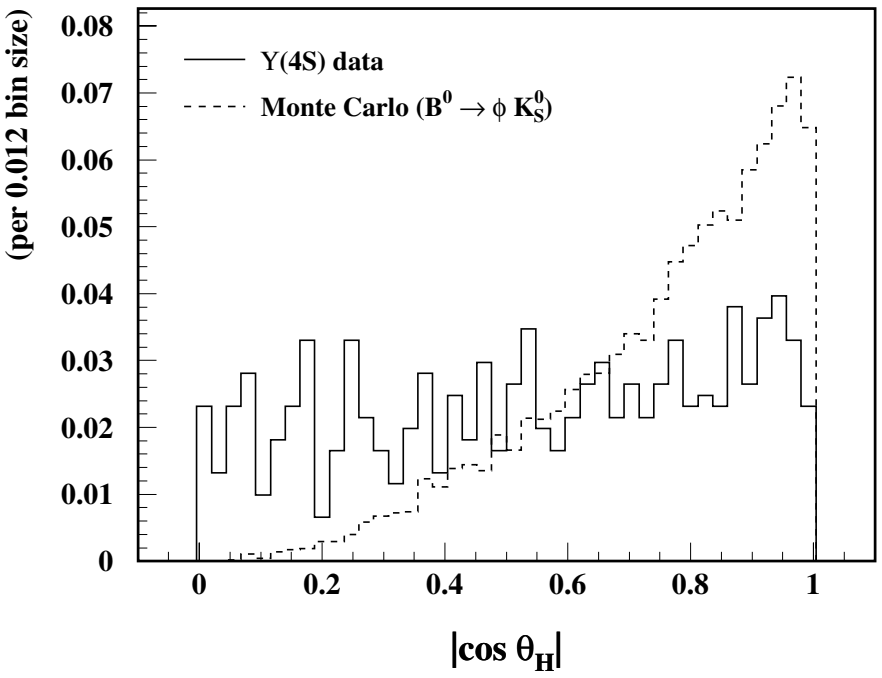

Figure 5.12: *Comparison between the* $|\cos\theta_H|$ *distribution from the* $B^0 \to \phi K^0_S$ *signal MC, and that obtained from on-resonance data, from the* `BCCKs3body` *skim. This comparison illustrates the difference between the signal distribution and that from the background dominated* $\Upsilon(4S)$ *data. A nominal cut at 0.5 would allow good separation between the signal events* (> 0.5) *and background events* (< 0.5). *The selection variables used to produce these plots are listed in Table 5.5, except that a selection cut of* 1020 ± 50 *MeV/*c^2 *was made on the* ϕ *meson mass resonance in place of the selection on the* ϕ *meson helicity angle* $|\cos\theta_H|$. *The distributions have been normalised to one in order to show their relative shapes.*

order to obtain the highest significance for the measurement of the branching fraction for the $B^0 \to K^{*+}\pi^-$ mode.

The resonant mass distribution of K^{*+} mesons has a Breit-Wigner width of $\Gamma = 50.8 \pm 0.9$ MeV/c^2 [17]. A selection on the nominal K^{*+} meson mass of 892 MeV/c^2 [17] was used to separate combinatoric backgrounds from the K^{*+} meson signal. This selection

was applied and the cut was varied between 892 ± 50 MeV/c^2 and 892 ± 70 MeV/c^2, in order to obtain the highest significance for the measurement of the $B^0 \to K^{*+}\pi^-$ branching fraction. The mass distributions of the reconstructed K^{*+} mesons from the $B^0 \to K^{*+}\pi^-$ signal MC, where $K^{*+} \to K^0_S\pi^+$, and from on-resonance data, from the `BCCKs3body` skim, are shown in Figure 5.13. The selection variables used to produce these plots are listed in Table 5.4, except that a selection cut of $c\tau/\sigma_{c\tau} > 10.0$ was made in place of the K^{*+} meson mass selection.

As with the ϕ meson, the K^{*+} meson is a vector meson with a spin of one. It too decays with a preferred topology. In the rest frame of the K^{*+} meson, the angle between the direction of flight of the parent B meson and the decay axis of the K^{*+} meson daughters, which decay back-to-back, is defined as the helicity angle $\theta_{\rm H}$. A selection on the absolute value of the cosine of this angle, $|\cos\theta_{\rm H}|$, is used to improve the selection of K^{*+} mesons. Figure 5.14 shows that the $|\cos\theta_{\rm H}|$ distribution is peaked towards $+1$ for K^{*+} mesons from the $B^0 \to K^{*+}\pi^-$ signal MC, while for the on-resonance data it is mostly flat.

5.7 Selection of D^- Mesons

For the study of the calibration mode $B^0 \to D^-\pi^+$, D^- mesons were reconstructed from the decay $D^- \to K^0_S\pi^-$ during Ntuple production. This mode has a total branching fraction of 0.0139, from $\mathcal{B}(D^- \to K^0\pi^-) = 0.0277 \pm 0.0018$ [17] and $\mathcal{B}(K^0 \to K^0_S) = 1/2$. This secondary branching fraction was taken into account for the measurement of the branching fraction for the $B^0 \to D^-\pi^+$ mode.

For each event, all combinations of a K^0_S meson and a track from those entered into the Ntuples, were used for the reconstruction of the D^- meson candidates. For the selection of pions, particle ID selection was applied to both tracks by vetoing the `tight` kaon selection criteria for each track. This particle ID selection is a loose pion selection and was chosen as a result of an optimisation process that was carried out in order to obtain the highest significance for the measurement of the branching fraction

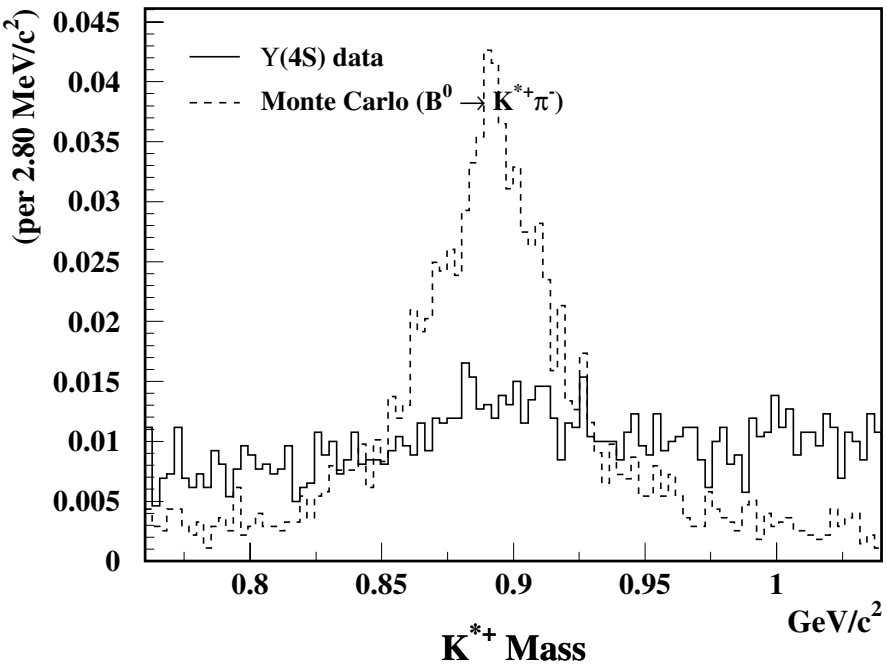

Figure 5.13: *Comparison between the K^{*+} meson mass distribution from the $B^0 \to K^{*+}\pi^-$ signal MC, where $K^{*+} \to K^0_S\pi^+$, and that obtained from on-resonance data, from the* `BCCKs3body` *skim, showing the K^{*+} meson mass peak in the former. A nominal 892 ± 50 MeV/c^2 mass cut would veto the background in the tails of these distributions. The selection variables used to produce these plots are listed in Table 5.4, except that a selection cut of $c\tau/\sigma_{c\tau} > 10.0$ was made in place of the K^{*+} meson mass selection. The distributions have been normalised to one in order to show their relative shapes.*

for the $B^0 \to D^-\pi^+$ mode.

A selection on the nominal D^- meson mass of 1869 MeV/c^2 [17] was used to separate combinatoric backgrounds from the D^- meson signal. This selection was applied and the cut was varied between 1869 ± 20 MeV/c^2 and 1869 ± 35 MeV/c^2, in order to obtain the highest significance for the measurement of the $B^0 \to D^-\pi^+$ branching fraction. The mass distributions of the reconstructed D^- mesons from the $B^0 \to D^-\pi^+$ signal

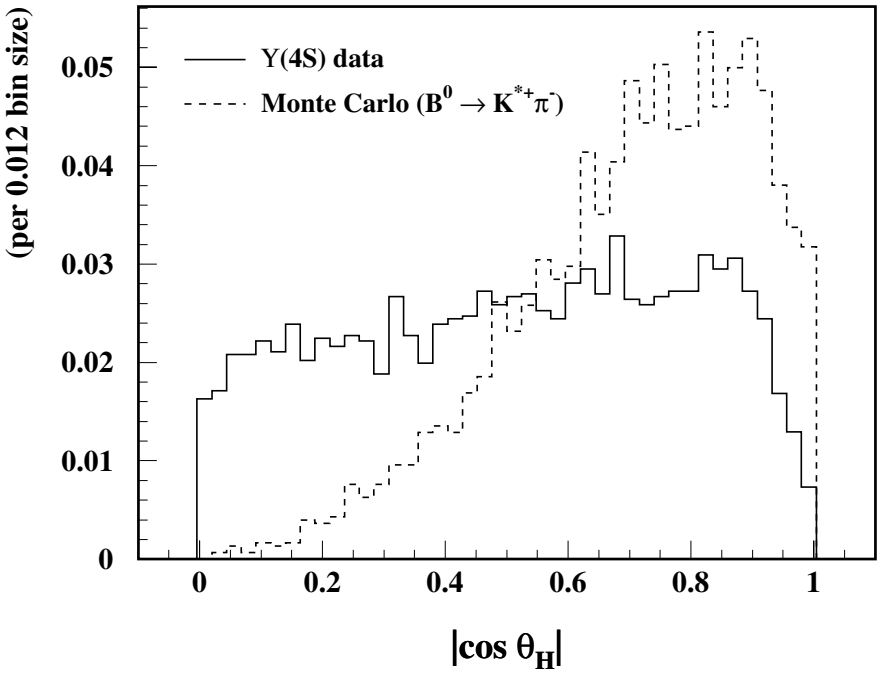

Figure 5.14: *Comparison between the* $|\cos\theta_H|$ *distribution from the* $B^0 \to K^{*+}\pi^-$ *signal MC, where* $K^{*+} \to K^0_S\pi^+$*, and that obtained from on-resonance data, from the* `BCCKs3body` *skim. This comparison illustrates the difference between the signal distribution and that from the background dominated* $\Upsilon(4S)$ *data. A nominal cut at 0.5 would allow good separation between the signal events (*> 0.5*) and background events (*< 0.5*). The selection variables used to produce these plots are listed in Table 5.4, except that a selection cut of* $c\tau/\sigma_{c\tau} > 10.0$ *was made in place of the selection on the* K^{*+} *meson helicity angle* $|\cos\theta_H|$*. The distributions have been normalised to one in order to show their relative shapes.*

MC, where $D^- \to K^0_S\pi^-$, and from on-resonance data, from the `BCCKs3body` skim, are shown in Figure 5.15. The selection variables used to produce these plots are listed in Table 5.4, except that a selection cut of $c\tau/\sigma_{c\tau} > 10.0$ was made in place of the K^{*+} meson mass selection, and no helicity angle cut was made since the D^- meson has a spin of zero and is, therefore, not polarised.

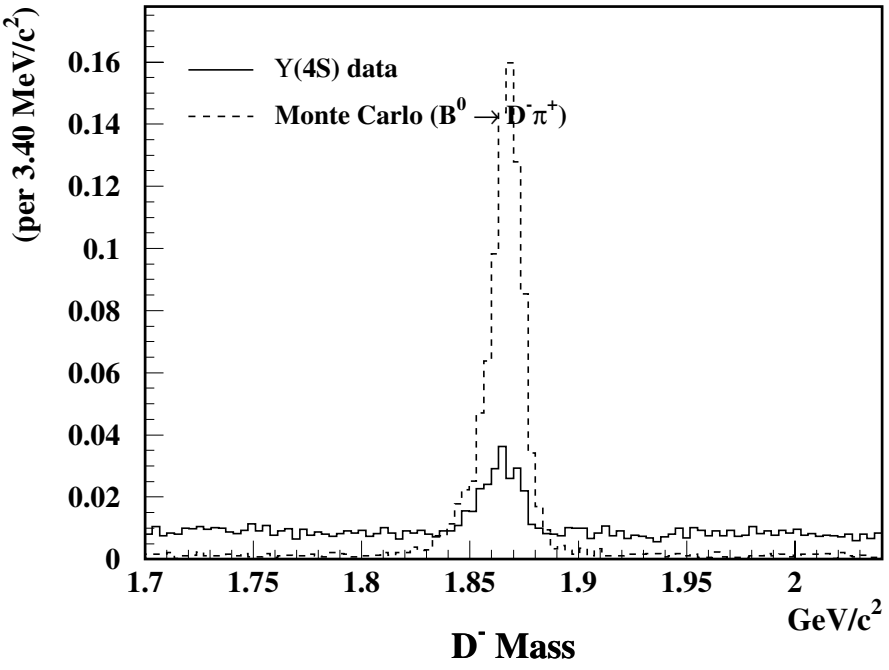

Figure 5.15: *Comparison between the D^- meson mass distribution from the $B^0 \to D^-\pi^+$ signal MC, where $D^- \to K^0_S\pi^-$, and that obtained from on-resonance data, from the* `BCCKs3body` *skim, showing the D^- meson mass peak in both. A nominal 1869 ± 30 MeV/c^2 mass cut would veto the background in the tails of these distributions. The selection variables used to produce these plots are listed in Table 5.4, except that a selection cut of $c\tau/\sigma_{c\tau} > 10.0$ was made in place of the K^{*+} meson mass selection, and no helicity angle cut was made. The distributions have been normalised to one in order to show their relative shapes.*

5.8 Signal and Sideband Regions

Details of the kinematic constraints $m_{\rm ES}$ and ΔE, which are used for the selection of reconstructed B meson candidates, were given in Section 4.7. In the two-dimensional $m_{\rm ES}$-ΔE plane, a signal region and one or more sideband regions may be chosen in order to determine the number of signal B meson candidates and the number of

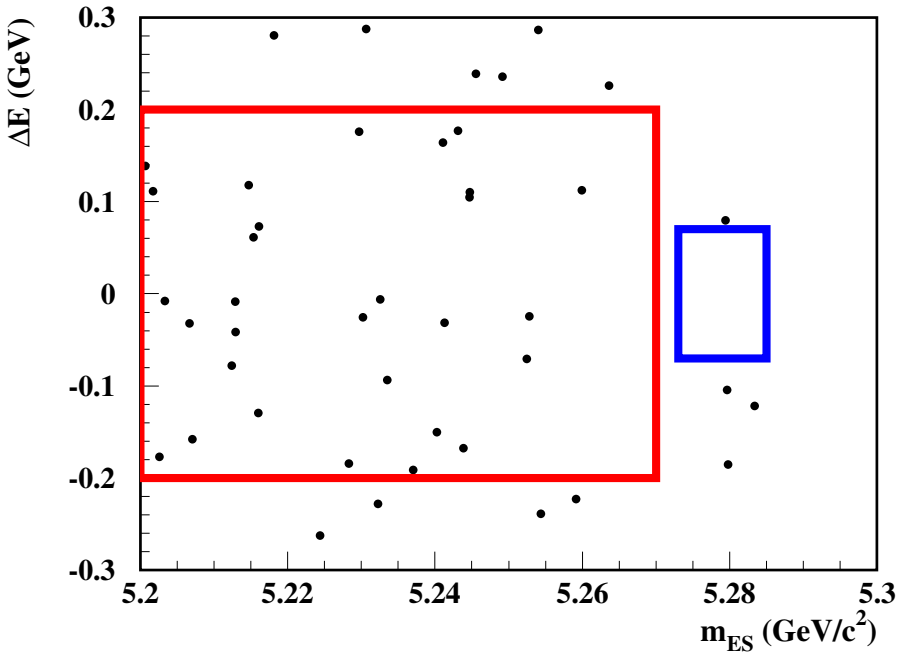

Figure 5.16: *The m_{ES}-ΔE plane showing the signal region, the small blue rectangle defined by $5.273 < m_{ES} < 5.285$ GeV/c^2 and $|\Delta E| < 0.07$ GeV, and the sideband region, the large red rectangle defined by $5.20 < m_{ES} < 5.27$ GeV/c^2 and $|\Delta E| < 0.2$ GeV, which was used to estimate the background in the signal region. This plot was produced from the off-resonance data using the final set of selection variable cuts used in the $B^0 \to K^{*+}\pi^-$ analysis and shown in Table 6.16.*

background candidates, respectively. Figure 5.16 shows the signal region and the sideband region chosen for the analyses presented here.

The number of events within the signal region $N_{\rm sig}$, includes both signal and background events. In order to find the number of true signal events N_S, the number of background events in the signal region N_B, must be subtracted from the total number of events observed there. The number of background events in the signal region is estimated by extrapolation from the number of background events in the sideband region $N_{\rm sb}$. In order to carry out this extrapolation, the background shape of the

$m_{\rm ES}$ and ΔE distributions must be carefully studied and characterised, to obtain the correct ratio between the number of background events in the signal region and in the sideband region.

5.9 Background Characterisation and Estimation

For the characterisations of the shapes of the background distributions, sideband regions were chosen in the $m_{\rm ES}$-ΔE plane, which did not include the signal region. These sideband regions are shown in Figure 5.17. They include two horizontal strips, the *upper* sideband, which is defined by,

$$5.20 \text{ GeV/c}^2 < m_{\rm ES} < 5.30 \text{ GeV/c}^2 \quad \text{and} \quad 0.1 \text{ GeV} < \Delta E < 0.3 \text{ GeV} \quad ,$$

and the *lower* sideband, which is defined by,

$$5.20 \text{ GeV/c}^2 < m_{\rm ES} < 5.30 \text{ GeV/c}^2 \quad \text{and} \quad \text{-0.3 GeV} < \Delta E < \text{-0.1 GeV} \quad .$$

The upper and lower sidebands were used to project data onto the $m_{\rm ES}$ axis for the characterisation of the background shape in its distribution. Another sideband region, which is defined by,

$$5.20 \text{ GeV/c}^2 < m_{\rm ES} < 5.27 \text{ GeV/c}^2 \quad \text{and} \quad |\Delta E| < 0.3 \text{ GeV} \quad ,$$

was used to project data onto the ΔE axis for the characterisation of the background shape in its distribution.

Figure 5.18 shows the typical background shape of the $m_{\rm ES}$ distribution, which was obtained by projecting the data in the upper and lower horizontal sidebands onto the $m_{\rm ES}$ axis. The background shape of the $m_{\rm ES}$ distribution is well represented by the *Argus function* [55], which is defined by,

$$\frac{dN}{dx} = Ax\sqrt{1-x^2}\exp\left[-\xi(1-x^2)\right], \tag{5.5}$$

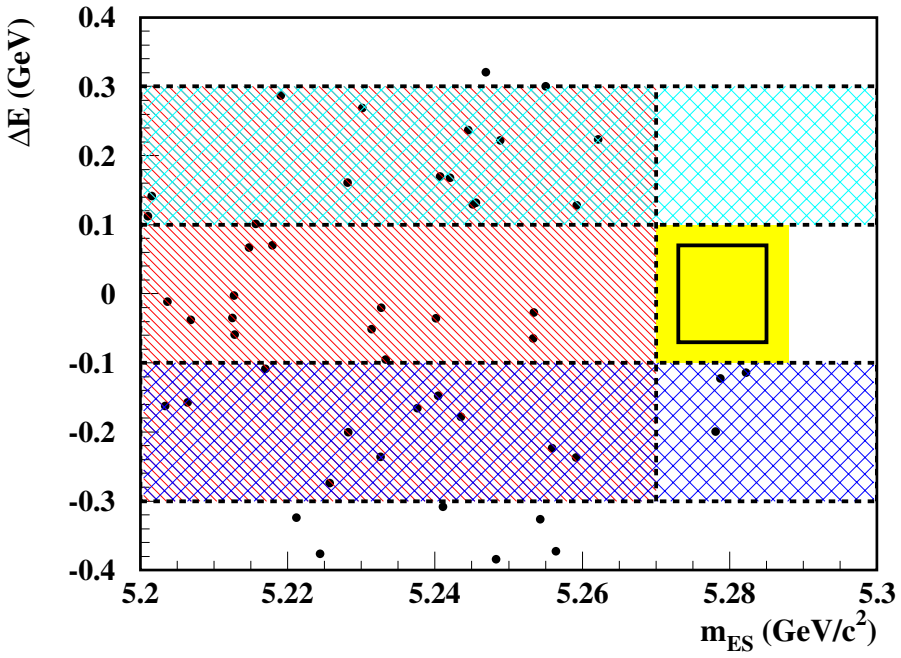

Figure 5.17: *The m_{ES}-ΔE plane showing the signal region, which is the small solid black rectangle defined by $5.273 < m_{ES} < 5.285$ GeV/c^2 and $|\Delta E| < 0.07$ GeV. The yellow box, which surrounds the signal region, is the blinded region and extends to the edge of the sideband regions in order to cover any signal leakage and to avoid any possible bias in the blind analysis. Also shown are the two cross-hatched upper and lower sideband regions and the large lightly shaded red region, which were used for the background characterisation of the m_{ES} and ΔE distributions, respectively. This plot was produced from the off-resonance data using the final set of selection variable cuts used in the $B^0 \to K^{*+}\pi^-$ analysis and shown in Table 6.16.*

where N is the number of events per bin, x represents the value of $m_{\rm ES}$, A is the normalisation of the distribution, and ξ is the Argus function parameter that defines the shape of the distribution. When characterising the $m_{\rm ES}$ distribution, ξ is the parameter that must be determined.

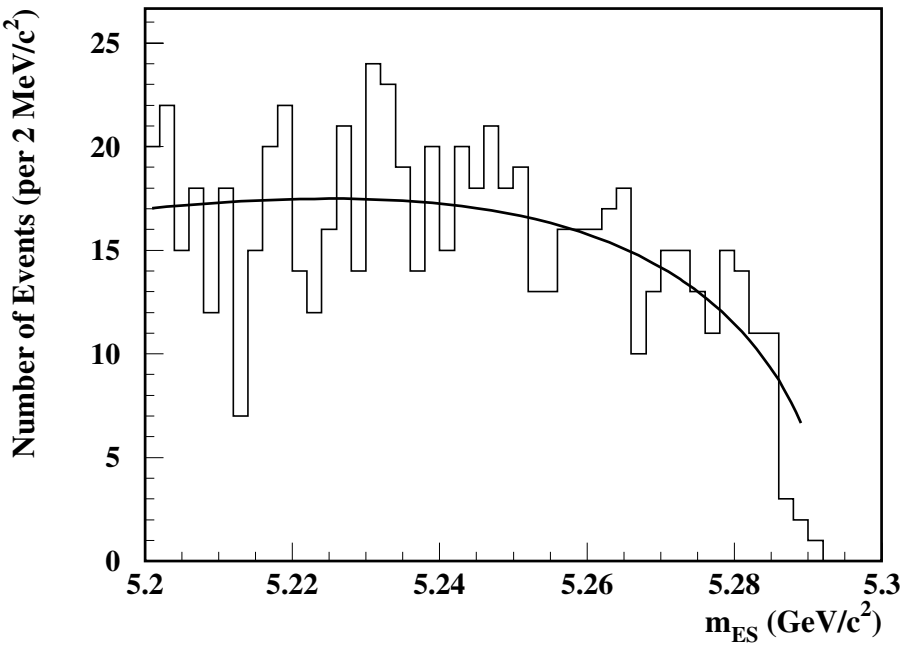

Figure 5.18: *The typical m_{ES} background distribution fitted with the Argus function shown in Equation 5.5. The Argus function parameter ξ is obtained from the fit. For this plot $\xi = 19.23$.*

The typical background shape of the ΔE distribution is shown in Figure 5.19 and is well represented by a simple quadratic function defined by,

$$\frac{dN}{dy} = B(1 + Cy + Dy^2)\,, \tag{5.6}$$

where y represents the value of ΔE, B is the normalisation of the distribution, and C and D are the parameters defining the shape of the distribution. When characterising the ΔE distribution, C and D are the parameters that must be determined.

Both on-resonance and off-resonance data were used for the characterisation of the $m_{\rm ES}$ and ΔE backgrounds for each analysis. A set of selection variables were applied for these characterisations, the details of which are given in the specific sections that

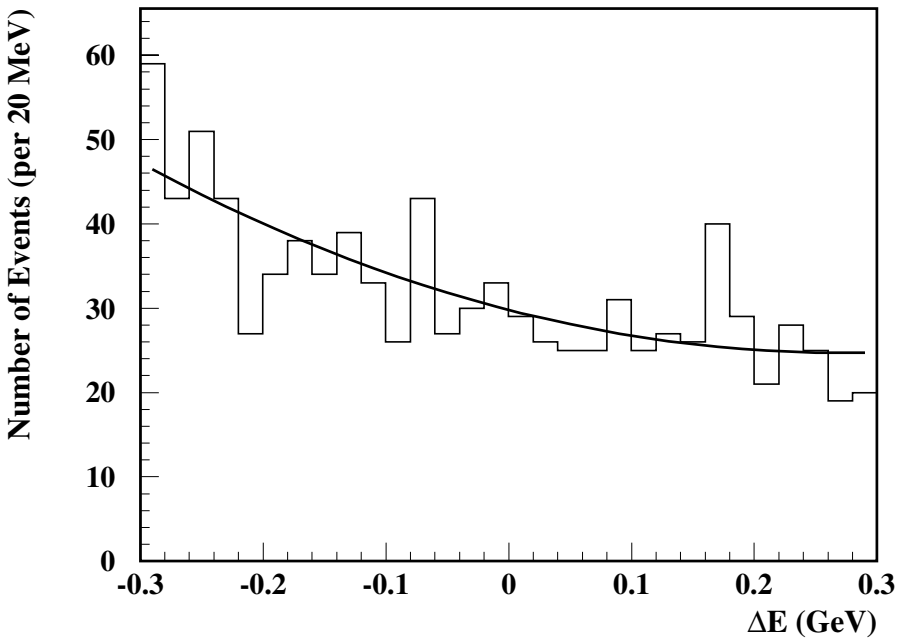

Figure 5.19: *The typical ΔE background distribution fitted with the quadratic function shown in Equation 5.6. The two defining parameters C and D are obtained from the fit. For this plot $C = -1.26$ and $D = 2.31$.*

describe the results of each analysis in Chapter 6.

The $m_{\rm ES}$ background was characterised for the sum of the data in the upper and the lower ΔE sidebands, and for the data in each sideband individually. Only on-resonance data were used for the latter, since the limited statistics in the individual sidebands in off-resonance data resulted in poor fits to the background.

For the extrapolation of the number of background events from the sideband region to the signal region, the ratios between the signal region and the sideband region, of the areas under the fits to the $m_{\rm ES}$ and ΔE background distributions, $R_{m_{\rm ES}}$ and $R_{\Delta E}$, respectively, must be determined. The determination of these ratios involves the calculation of the integral of the fitted function to each distribution, between the signal

region and sideband region limits. The product of these ratios $\mathcal{A}$, is given in Equation 5.7 and is the ratio between the number of background events in the sideband region $N_{\rm sb}$, to that in the signal region N_B, as given in Equation 5.8.

$$\mathcal{A} = R_{m_{\rm ES}}\, R_{\Delta E}\,. \tag{5.7}$$

$$N_B = \mathcal{A}\, N_{\rm sb}\,. \tag{5.8}$$

5.10 Selection Variable Cut-Optimisation

The selection variable cut values were optimised to give the highest significance for the measurement of the branching fraction for each analysis. The significance calculated for each set of cut values is defined by,

$$\text{significance} = \frac{N_S}{\sqrt{N_S + N_B}}\,, \tag{5.9}$$

where N_S and N_B are the number of signal and background events in the signal region, respectively. The estimation of N_B by extrapolation from the number of background events in the sideband region was explained in Section 5.9.

The value of each selection variable was varied independently from that of the others, about a nominal value chosen by comparison of the distributions of that selection variable in on-resonance data and in signal MC, as illustrated in Figures 5.2, 5.4, 5.7, 5.10, 5.12, 5.13, 5.14, and 5.15, after the application of a set of loose selection cuts. The significance in Equation 5.9 was calculated for all combinations of the selection variable cuts, and the set of values resulting in the highest significance was chosen.

The cut-optimisation process inherently introduces a bias into the estimation of N_B. Since the selection variable cuts are optimised by maximising the significance in Equation 5.9, the background in the sideband region, and hence its estimate in the signal region, are both minimised. Any fluctuation in the number of background events will also be minimised, resulting in a low estimate of N_B and a biased analysis. For this

reason, cut-optimisation is undertaken using only half of the on-resonance $B\bar{B}$ events in the sideband region, the even numbered events. The background in the signal region is then estimated by using the optimised cuts on the other half of the events, the odd numbered events, and scaling up by a factor of two. Equation 5.8 then becomes,

$$N_B = \mathcal{A}\, 2 N_{\rm sb}\,. \tag{5.10}$$

For the blind analyses presented here, the distribution of events in the signal region of the $m_{\rm ES}$-ΔE plane was kept hidden until the analysis cuts were optimised and the analyses were ready for unblinding. Since the signal region is blinded, N_S is calculated using,

$$N_S = \epsilon\, N_{B\bar{B}}\, \mathcal{B}_{\rm ba}\,, \tag{5.11}$$

where ϵ is the signal efficiency, which was obtained from the signal MC, $N_{B\bar{B}}$ is the number of $B\bar{B}$ events used for these analyses, and $\mathcal{B}_{\rm ba}$ is the *best available* measurement, or estimate, of the branching fraction for each mode.

5.11 Signal Efficiency and Corrections

The signal efficiency ϵ is given by,

$$\epsilon = \frac{N_{S_{\rm MC}}}{N_{\rm MC}}\,, \tag{5.12}$$

where $N_{\rm MC}$ is the total number of signal MC events used for the analyses (20,000 events) and $N_{S_{\rm MC}}$ is the number of signal MC events that pass the selection variable cuts in the signal region. As a result of discrepancies between the generated MC and the detector data, ϵ must be corrected using a number of correction factors.

Some of these correction factors are obtained using control samples from data. These include correction factors for tracking efficiencies, particle ID efficiencies, and for the

Table 5.6: *Efficiency correction factors for the discrepancies between the generated MC and on-resonance data for the analyses presented here. The particle ID and tracking corrections and their errors, are for two pions, two kaons, and two tracks.*

	Correction Factor
$2 \times \pi$ meson particle ID	0.988 ± 0.040
$2 \times K$ meson particle ID	0.986 ± 0.099
$2\times$ tracks tracking	0.969 ± 0.023
K^0_S meson	1.034 ± 0.037
ΔE	0.993 ± 0.009
$m_{\rm ES}$	1.000 ± 0.014

selection of K^0_S mesons. In addition, correction factors for the $m_{\rm ES}$ and ΔE distributions were obtained using the calibration mode, by comparing their distributions from signal MC and from on-resonance data for the final set of selection variable cuts for the $B^0 \to D^-\pi^+$ analysis. A list of the efficiency corrections is given in Table 5.6. The corrected MC signal efficiency $\epsilon_{\rm c}$, is the product of these corrections and ϵ.

For the analyses presented here, where neutral B mesons decay to a three-body final state with one K^0_S meson and two tracks, the decay $B^0 \to D^-\pi^+$, where $D^- \to K^0_S\pi^-$, was chosen for the calibration mode. This mode offers a large branching fraction and suffers from relatively small backgrounds, allowing good comparisons between signal MC and on-resonance data, and making it ideal as a calibration mode. This mode was studied following the method used for the two modes of interest.

5.12 Branching Fraction Measurement

Once the selection variable cuts were optimised and the analyses were unblinded, the number of signal events N_S, was determined by subtracting the estimated number of background events in the signal region N_B, from the total number of events $N_{\rm sig}$, observed there.

$$N_S = N_{\rm sig} - N_B \,. \tag{5.13}$$

The branching fraction $\mathcal{B}$ for each analysis is then given by,

$$\mathcal{B} = \frac{N_S}{N_{B\bar{B}}\,\epsilon_{\rm c}\,\mathcal{B}_{\rm sec}} \,, \tag{5.14}$$

where,

$$\epsilon_{\rm c} = \epsilon \times \text{Correction Factors} \,, \tag{5.15}$$

and $\mathcal{B}_{\rm sec}$ is the product of the secondary branching fractions for the secondary decays used to reconstruct the mode being measured.

Chapter 6

Analysis Results and Discussion

6.1 Analysis Details of the Calibration Mode, $B^0 \to D^-\pi^+$

The calibration mode was used to validate the analyses of the two rare charmless hadronic B meson decays presented here. In addition, it was used to determine correction factors for the $m_{\rm ES}$ and ΔE selections, for the signal efficiency ϵ, for each mode. These correction factors were used to correct for discrepancies between the generated MC and data. They were obtained by comparing the distributions of the $m_{\rm ES}$ and ΔE selection variables from signal MC and from on-resonance data. The calibration mode must be a B meson decay mode with a relatively large branching fraction compared to the two modes under study, and one that offers low background levels so that the signal in the data distributions is prominent.

The mode $B^0 \to D^-\pi^+$, where $D^- \to K^0_S\pi^-$, was chosen as a suitable calibration mode. This mode has a K^0_S meson and two tracks in its final state, which is the same as that in the decay $B^0 \to K^{*+}\pi^-$, where $K^{*+} \to K^0_S\pi^+$. The two final state tracks in both of these modes are $\pi^+\pi^-$, one of which comes from the B meson's resonant daughter. Although this mode is not an ideal match to the final state of $B^0 \to \phi K^0_S$, where $\phi \to K^+K^-$ and the two final state tracks are both from the B meson's resonant daughter, it is the best match to the overall final state of this decay.

Table 6.1: *The selection variables used for the selection of the* $B^0 \to D^-\pi^+$ *mode, where* $D^- \to K^0_S\pi^-$.

Selection Variable	Optimised
Thrust angle $\lvert\cos\theta_{\rm T}\rvert$	Optimised
Fisher discriminant	Optimised
Track particle ID for pions	Optimised
K^0_S meson mass	Not optimised
K^0_S meson flight length $c\tau/\sigma_{c\tau}$	Optimised
D^- meson mass	Optimised
Beam-energy constrained ΔE	Not optimised
Beam-energy substituted mass, $m_{\rm ES}$	Not optimised

The analysis and measurement of the branching fraction for this mode were carried out by following closely the methods described in Chapter 5. The details of the background characterisation and cut-optimisation of the selection variables are given in Sections 6.1.2 and 6.1.3, along with the results obtained for each procedure. The selection variables used for the selection of this mode are listed in Table 6.1. This table indicates the selection variables that were optimised according to the method described in Section 5.10, in order to obtain the highest significance for the measurement of the branching fraction.

6.1.1 Study of the Signal MC for $B^0 \to D^-\pi^+$

Signal MC data were used to determine the signal efficiency for the three modes analysed. In addition, the signal MC data were used to help define the extents of

the signal region in the $m_{\rm ES}$-ΔE plane. The distributions of $m_{\rm ES}$ and ΔE from the signal MC for $B^0 \to D^-\pi^+$, where $D^- \to K^0_S\pi^-$, are shown in Figure 6.1. Also shown is the D^- meson mass distribution from the same signal MC data. The final optimised selection variable cuts that are listed in Table 6.4 were used to produce these distributions.

The signal region for all of the three modes analysed is defined by,

$$5.273 \text{ GeV/c}^2 < m_{\rm ES} < 5.285 \text{ GeV/c}^2 \quad \text{and} \quad |\Delta E| < 0.07 \text{ GeV} \quad ,$$

and the sideband region that was used to estimate the background in the signal region is defined by,

$$5.20 \text{ GeV/c}^2 < m_{\rm ES} < 5.27 \text{ GeV/c}^2 \quad \text{and} \quad |\Delta E| < 0.2 \text{ GeV} \quad .$$

Note that, although the sideband region used for the background characterisation of ΔE spans $|\Delta E| < 0.3$ GeV, only the $|\Delta E| < 0.2$ GeV region is used for the estimation of the background in the signal region. This was done in order to reduce the effect of backgrounds from incorrectly reconstructed B mesons with missing energy, on the estimation of the number of background events in the signal region. These backgrounds appear in the $\Delta E < -0.1$ GeV region within the limits of the $m_{\rm ES}$ signal region, and are not characteristic of the distribution of the continuum background in the rest of the $m_{\rm ES}$-ΔE plane.

6.1.2 Background Characterisation for $B^0 \to D^-\pi^+$

The shapes of the background distributions of $m_{\rm ES}$ and ΔE were characterised as described in Section 5.9. Figure 6.2 shows the values of the Argus function parameter ξ, which were obtained from the fits to the $m_{\rm ES}$ background distributions for different values of the $|\cos\theta_{\rm T}|$ selection variable. This characterisation is shown for two different sets of selection cuts for each of the on-resonance and off-resonance data. These

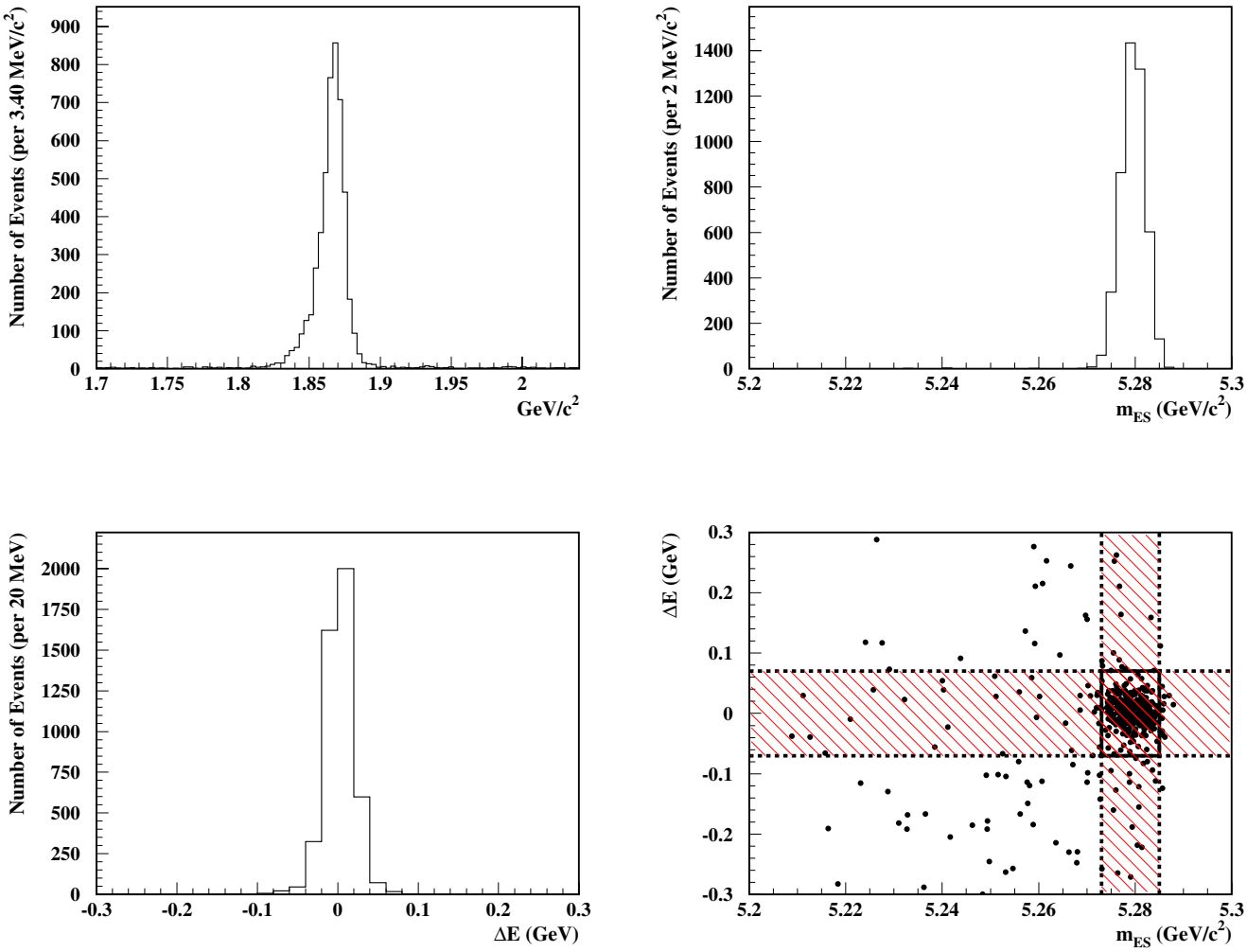

Figure 6.1: *The m_{ES} (top right) and ΔE (bottom left) distributions for 20,000 $B^0 \to D^-\pi^+$ signal MC events, where $D^- \to K^0_S\pi^-$. The shaded bands in the 2-D scatter plot of the m_{ES}-ΔE plane (bottom right), show the constraint of the signal region of each variable on the distribution of the other. Also shown is the D^- meson mass distribution (top left) from the same signal MC data, for the candidates in the signal region.*

Table 6.2: *The selection variables used for the background characterisations of m_{ES} and ΔE for the $B^0 \to D^-\pi^+$ analysis. The thrust angle $|\cos\theta_T|$ selections were applied with both the loose and the tight selection on the Fisher discriminant.*

Selection Variable	Selections	
	Loose	Tight
Fisher discriminant	< 1.5	< 0.5
D^- meson mass	1869 ± 200 MeV/c^2	
K^0_S meson flight length $c\tau/\sigma_{c\tau}$	> 0.0	
Track particle ID for pions	not `tight` kaon ID	
K^0_S meson mass	498 ± 8 MeV/c^2	
Thrust angle $\lvert\cos\theta_T\rvert$	$< 0.80, 0.85, 0.90, 0.95, 0.98, 1.00$	

include selection cuts on the D^- meson mass, the $c\tau/\sigma_{c\tau}$ selection on the flight length of the K^0_S meson, and a loose and a tight selection cut on the Fisher discriminant as summarised in Table 6.2. The same set of selection criteria were applied for the characterisation of the two parameters C and D of the quadratic fit to the ΔE background distribution. The values of C and D for these characterisations are shown in Figure 6.3.

The top plot in Figure 6.2 shows the results of the fits to the sum of the $m_{\rm ES}$ background distributions in the upper and lower ΔE sidebands, which are defined by 0.1 GeV $< \Delta E <$ 0.3 GeV and -0.3 GeV $< \Delta E <$ -0.1 GeV, respectively. The bottom plot in this figure shows the results of the characterisation of the $m_{\rm ES}$ background distribution for each of the upper and lower ΔE sidebands individually, for on-resonance data only.

There is considerable cross-talk in this mode from B meson decays to other final states

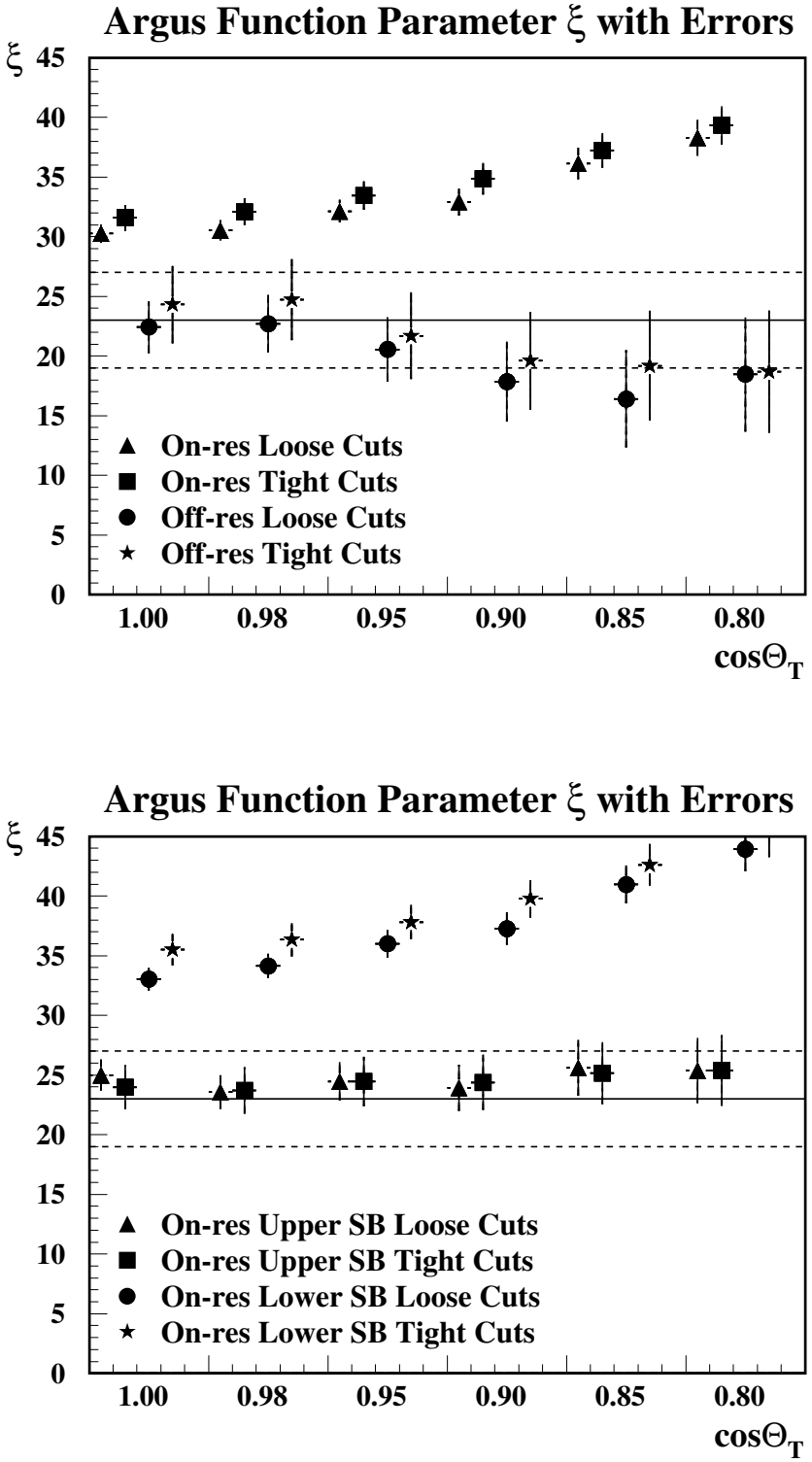

Figure 6.2: *The values of the Argus function parameter ξ, obtained by fitting the m_{ES} distributions in the upper and lower ΔE sidebands together (top), and separately (bottom), for the $B^0 \to D^-\pi^+$ analysis. On-resonance and off-resonance data were used with a loose and a tight selection cut on the Fisher discriminant.*

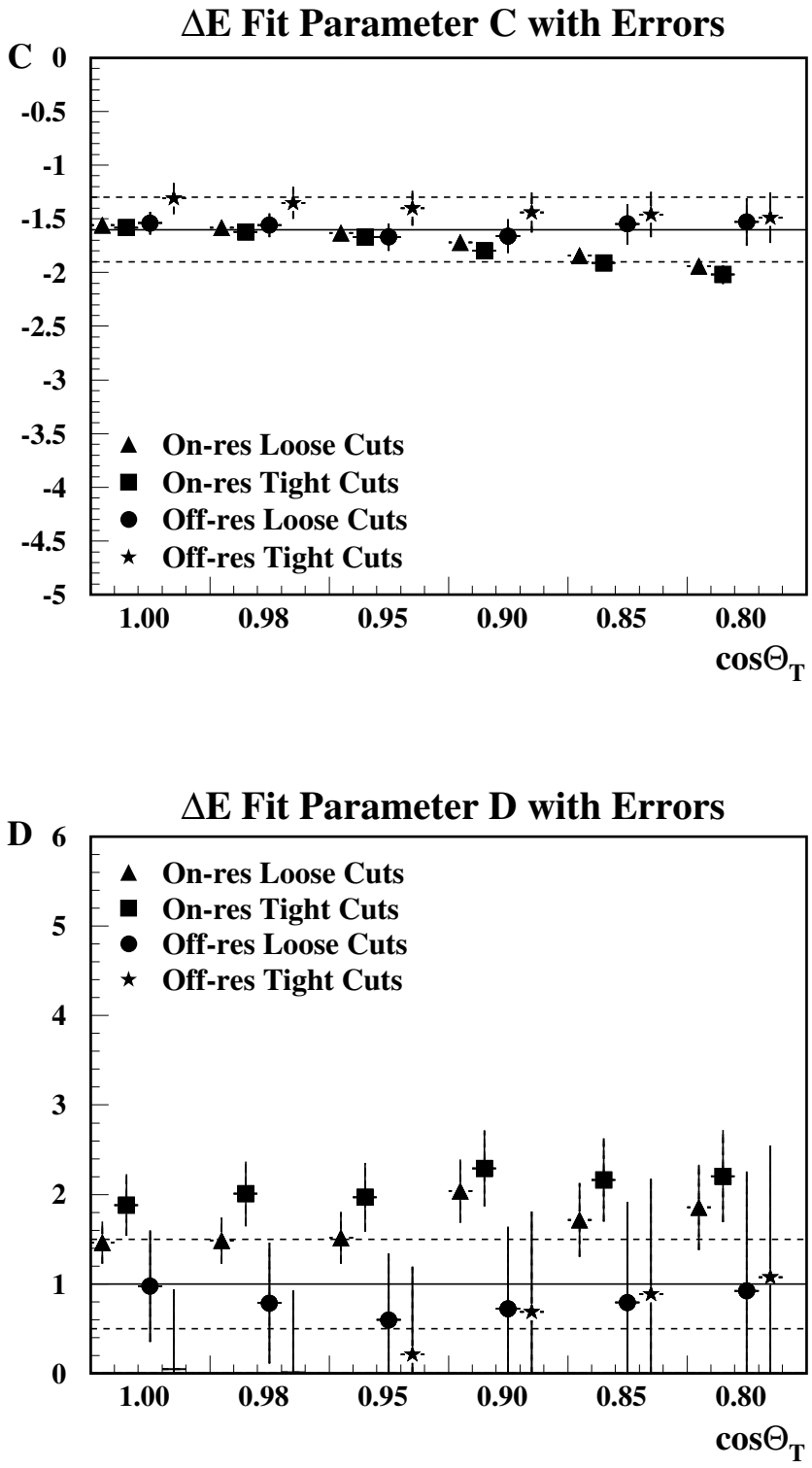

Figure 6.3: *The values of the parameters C (top) and D (bottom), of the quadratic fits to the ΔE background distributions for the $B^0 \to D^-\pi^+$ analysis. On-resonance and off-resonance data were used with a loose and a tight selection cut on the Fisher discriminant.*

with a charmed meson. These modes may include $B^0 \to D^- \rho^+$, where $D^- \to K^0_S \pi^-$ and $\rho^+ \to \pi^0 \pi^+$, or $B^0 \to D^{*-} \pi^+$, where $D^{*-} \to D^- \pi^0$ and $D^- \to K^0_S \pi^-$. Incorrectly reconstructed B meson candidates from these modes will have missing energy due to a missing final state particle. The missing particle for the two mentioned modes would be the π^0 meson, which would result in a ΔE that is less than 0 GeV by at least the nominal mass of the π^0 meson. These incorrectly reconstructed B mesons fall within the $\Delta E < 0$ GeV region of the $m_{\rm ES}$-ΔE plane as shown in Figure 6.4, which was produced using the final optimised selection variable cuts in Table 6.4. As a result, this cross-talk affects the background characterisations for this mode. The fit to the $m_{\rm ES}$ background distribution in the lower ΔE sideband, therefore, does not correctly characterise the continuum background. For the determination of ξ, only the fits to the $m_{\rm ES}$ background distributions from off-resonance data and the upper ΔE sideband in on-resonance data were used. The same cross-talk affects the characterisation of the ΔE background distribution in on-resonance data, and the off-resonance data were therefore used for the characterisation of the continuum background in ΔE.

The chosen value for each of the parameters ξ, C, and D, was not obtained by using a fit to the values shown in Figures 6.2 and 6.3. This was because it was found that the variation of their values between the large systematic errors assigned to them, made an insignificant difference to the value of the ratio $\mathcal{A}$, and hence, the estimation of the number of background events in the signal. Figures 6.2 and 6.3 show the chosen value (solid line) for each of the characterised parameters, which is a best estimate from the values obtained, with the assigned systematic errors (dashed lines). These results are summarised in Table 6.3. The calculated value of $\mathcal{A}$ for this analysis is 0.0439 ± 0.0034.

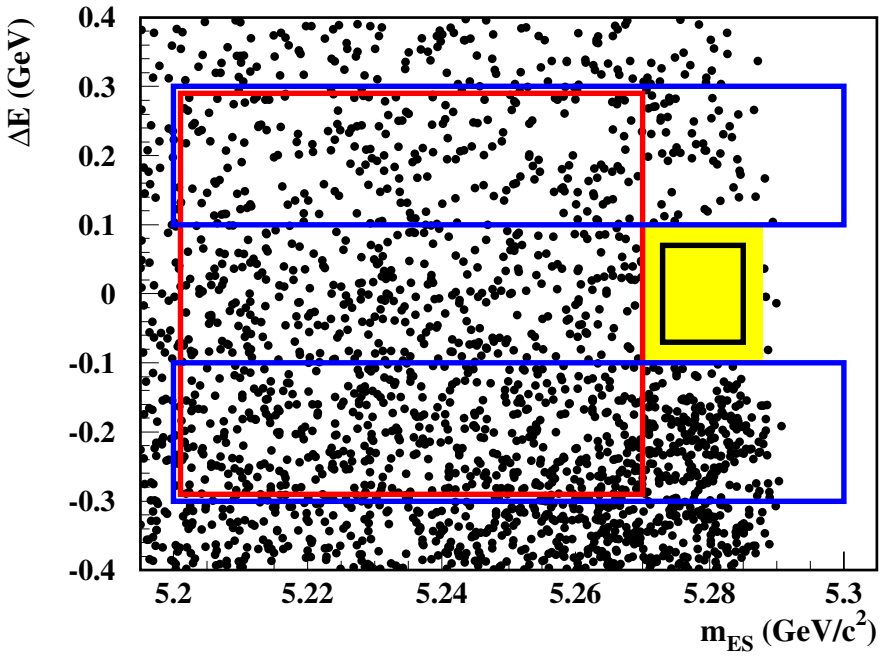

Figure 6.4: *The distribution of reconstructed B meson candidates from on-resonance data, for the $B^0 \to D^-\pi^+$ analysis. Considerable cross-talk from B meson decays to other final states with a charmed meson is evident in the lower ΔE sideband, within the limits of the m_{ES} signal region. This cross-talk creeps into the lower right hand corner of the square sideband region used for the characterisation of the ΔE background distribution.*

6.1.3 Cut-Optimisation for $B^0 \to D^-\pi^+$

The procedure for cut-optimisation was described in Section 5.10. The best available branching fraction that was used in Equation 5.11 to estimate N_S was [17],

$$\begin{aligned} & \mathcal{B}_{\rm ba}((B^0 \to D^-\pi^+) \times (D^- \to K^0\pi^-) \times (K^0 \to K^0_S) \times (K^0_S \to \pi^+\pi^-)) \\ = \;& (3.0 \times 10^{-3}) \times 0.028 \times 0.500 \times 0.686 \\ = \;& 2.88 \times 10^{-5}\,. \end{aligned} \tag{6.1}$$

Table 6.3: *Results of the background characterisations of m_{ES} and ΔE for the $B^0 \to D^-\pi^+$ analysis.*

Background Distribution	Fitted Function	Fit Parameter	Value and Systematic Error
$m_{\rm ES}$	Argus	ξ	23 ± 4
ΔE	Quadratic	C	-1.6 ± 0.3
ΔE	Quadratic	D	1.0 ± 0.5

The final set of selection variables are listed in Table 6.4.

6.1.4 Study of the Backgrounds in $B^0 \to D^-\pi^+$

Using the final set of optimised selection variable cuts shown in Table 6.4, the number of reconstructed B meson candidates in the signal region, $N_{\rm sig}$, and in the sideband region, $N_{\rm sb}$, were counted for every event in off-resonance data, and in the generic MC and charmless hadronic $B\bar{B}$ MC data that were introduced in Sections 4.4.2 and 4.4.3, respectively.

The results are given in Table 6.5 and show a considerable number of events in the signal region for the generic $B^0\bar{B}^0$ MC data sample. A study of the MC decay trees for these events shows that 55 of the 62 events include the signal mode $B^0 \to D^-\pi^+$, where $D^- \to K^0_S\pi^-$ and $K^0_S \to \pi^+\pi^-$. Of the remaining seven events, two have the decay $B^0 \to K^0_S\pi^+\pi^-$, where $K^0_S \to \pi^+\pi^-$, and the others involve decays where muons and high energy kaons have been misidentified as pions. In addition, of the ten events in the signal region in the charmless hadronic $B\bar{B}$ MC data sample, five include the signal mode from the B meson which was not forced to decay to a charmless final state, four are the non-resonant $B^0 \to K^0_S\pi^+\pi^-$ mode, and one is the mode $B^0 \to \rho^0 K^0_S$. The latter has four charged pions in its final state, which is the same as for the signal

Table 6.4: *The final set of selection variable cuts used in the* $B^0 \to D^-\pi^+$ *analysis.*

Selection Variable	Cut Value
Thrust angle $\lvert\cos\theta_{\rm T}\rvert$	< 1.0 (no cut)
Fisher discriminant	< 0.4
Track particle ID for pions	not `tight` kaon ID
K^0_S meson mass	498 ± 8 MeV/c^2
K^0_S meson flight length $c\tau/\sigma_{c\tau}$	> 2.0
D^- meson mass	1869 ± 30 MeV/c^2
Beam-energy constrained $\lvert\Delta E\rvert$	< 70 MeV
Beam-energy substituted mass, $m_{\rm ES}$	5279 ± 6 MeV/c^2

mode.

Except for the cross-talk from the non-resonant decay $B^0 \to K^0_S\pi^+\pi^-$, where $K^0_S \to \pi^+\pi^-$, the cross-talk from all the other mentioned modes is thought to be negligible. A study of 17,000 exclusive MC events of the non-resonant decay $B^0 \to K^0_S\pi^+\pi^-$, where $K^0_S \to \pi^+\pi^-$, using the optimised selection cuts in Table 6.4, resulted in 108 reconstructed B meson candidates in the signal region. This represents a selection efficiency of 0.64 %.

There is currently no published measurement of the branching fraction for the non-resonant decay $B^0 \to K^0_S\pi^+\pi^-$, and only an upper limit of $\mathcal{B}(B^0 \to K^0\pi^+\pi^-) < 4.4\times10^{-4}$ at 90 % confidence limit (CL) has been calculated [56]. Using the branching fraction of $\mathcal{B}(B^0 \to K^0\pi^+\pi^-) = 5\times10^{-5}$ [57] that was recently presented by the CLEO experiment, and taking into account the secondary branching fractions for $K^0 \to K^0_S$ and $K^0_S \to \pi^+\pi^-$, the number of expected background events due to $B^0 \to K^0_S\pi^+\pi^-$

Table 6.5: *The number of reconstructed B meson candidates in the signal region, N_{sig}, and sideband region, N_{sb}, in off-resonance data, and in the generic MC and charmless hadronic $B\bar{B}$ MC data. The number of signal events and non-resonant events with the same final state, N_{true}, are also given. $\mathcal{L}$ is the equivalent integrated luminosity for the data samples used.*

Data	$\mathcal{L}$ (fb^{-1})	$N_{\rm sig}$	$N_{\rm sb}$	$N_{\rm true}$
Charmless $B\bar{B}$ MC data	21	10	14	5 + 4 non-resonant
Generic $B^0\bar{B}^0$ MC data	5.0	62	12	55 + 2 non-resonant
Generic B^+B^- MC data	8.3	0	22	–
Generic $c\bar{c}$ MC data	5.0	1	70	–
Generic uds MC data	5.7	3	119	–
Off-resonance data	2.6	3	82	–

is 2.5 events. This adds a negligible systematic error to the measurement of $\mathcal{B}(B^0 \to D^-\pi^+)$ and is not taken into account.

6.1.5 Branching Fraction of $B^0 \to D^-\pi^+$

Using the final set of optimised selection variable cuts shown in Table 6.4, the number of reconstructed B meson candidates in the signal region, $N_{\rm sig}$, was counted for every event in on-resonance data. The number of background events in the signal region, N_B, was estimated using Equation 5.10. For this purpose, the number of events in the sideband region, $N_{\rm sb}$, was counted for only half of the events from on-resonance data, the odd numbered events, and scaled up by a factor of two. This was done in order to avoid introducing a bias by minimising any fluctuations in the number of background events in the cut-optimisation process described in Section 5.10. The number of signal

Table 6.6: *The final results for the $B^0 \to D^-\pi^+$ analysis. Unless otherwise stated, the first error is the statistical error and the second is the systematic error.*

Number of events in signal region, $N_{\rm sig}$	210
Number of events in sideband region, $N_{\rm sb}$	706
Ratio of sideband to signal region events, $\mathcal{A}$	0.0439±0.0034(syst.)
Number of background events in signal region, N_B	$31.0 \pm 1.6 \pm 2.4$
Number of signal events in signal region, N_S	179.0
Number of B^0 and $\bar{B}^0$ mesons, equal to $N_{B\bar{B}}$	$(22.55 \pm 0.36(\text{total})) \times 10^6$
Corrected Selection efficiency, $\epsilon_{\rm c}$	$23.0 \pm 0.3 \pm 1.4$ %
Secondary Branching Fractions, $\mathcal{B}_{\rm sec}$	$0.028 \times 0.500 \times 0.686$
Branching fraction, $\mathcal{B}(B^0 \to D^-\pi^+)$	$(3.59 \pm 0.29 \pm 0.35) \times 10^{-3}$

events, N_S, was calculated using Equation 5.13. The branching fraction was calculated using Equation 5.14.

The final results are summarised in Table 6.6. The final branching fraction of $\mathcal{B}(B^0 \to D^-\pi^+) = (3.59 \pm 0.29(\text{stat.}) \pm 0.35(\text{syst.})) \times 10^{-3}$ was obtained using the secondary branching fractions $\mathcal{B}(D^- \to K^0\pi^-) = 0.0277 \pm 0.0018$, $\mathcal{B}(K^0 \to K^0_S) = 0.5$, and $\mathcal{B}(K^0_S \to \pi^+\pi^-) = 0.686 \pm 0.003$. This measurement is in good agreement with the world-average branching fraction for this mode, $\mathcal{B}_{\rm ave}(B^0 \to D^-\pi^+) = (3.0 \pm 0.4(\text{total})) \times 10^{-3}$ [17].

Figure 6.5 shows the $m_{\rm ES}$ and ΔE distributions from on-resonance data, which were obtained using the final set of optimised selection variable cuts listed in Table 6.4.

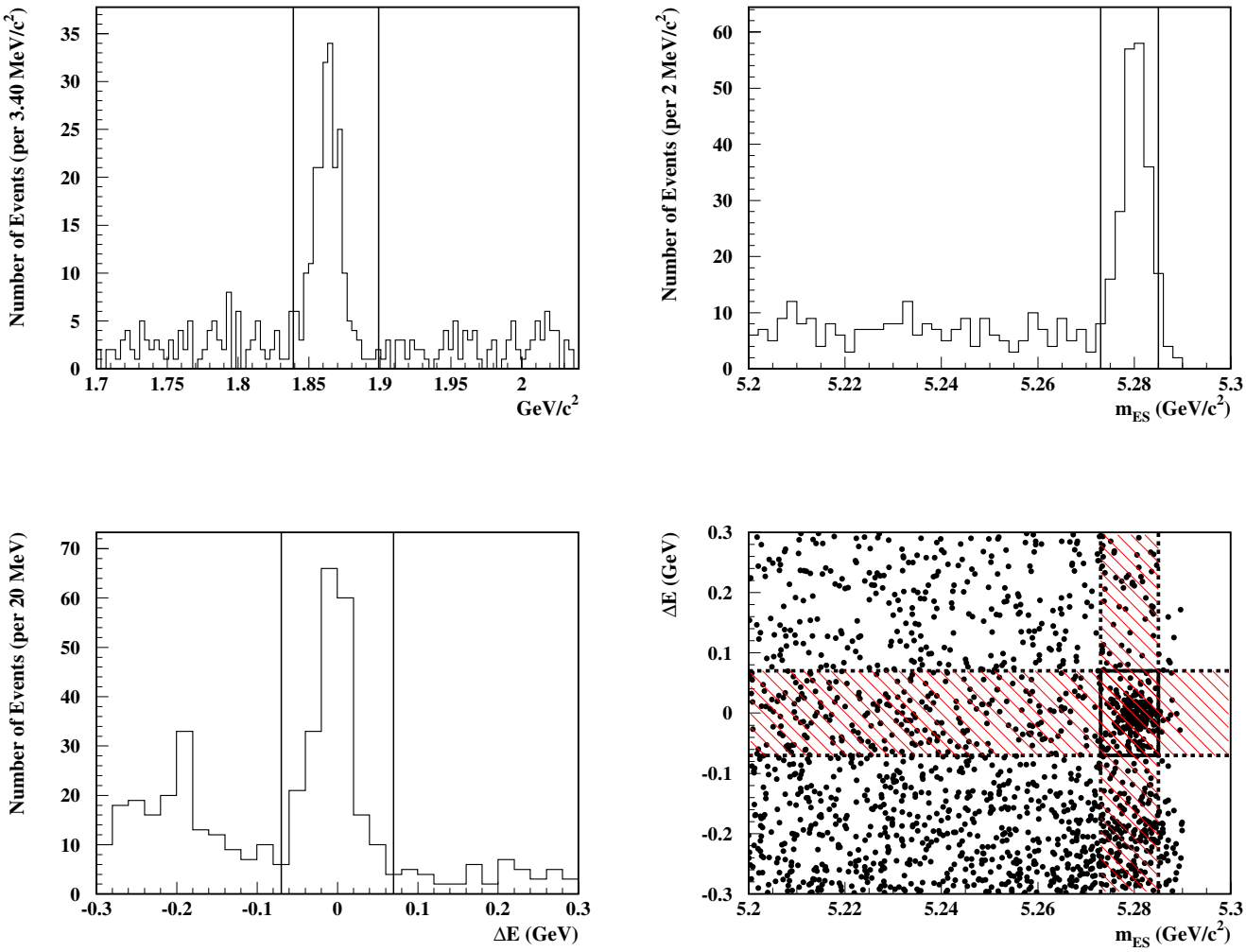

Figure 6.5: *The m_{ES} (top right) and ΔE (bottom left) distributions obtained from on-resonance data using the final set of optimised selection variable cuts listed in Table 6.4 for the $B^0 \to D^- \pi^+$ analysis. Also shown is the D^- meson mass distribution (top left) from the same data, for the candidates in the signal region.*

Table 6.7: *The selection variables used for the selection of the* $B^0 \to \phi K^0_S$ *mode, where* $\phi \to K^+K^-$.

Selection Variable	Optimised
Thrust angle $\lvert\cos\theta_{\rm T}\rvert$	Optimised
Fisher discriminant	Optimised
Track particle ID for kaons	Optimised
K^0_S meson mass	Not optimised
K^0_S meson flight length $c\tau/\sigma_{c\tau}$	Optimised
ϕ meson resonance mass	Optimised
ϕ meson helicity angle $\lvert\cos\theta_{\rm H}\rvert$	Optimised
Beam-energy constrained ΔE	Not optimised
Beam-energy substituted mass, $m_{\rm ES}$	Not optimised

6.2 Analysis Details of $B^0 \to \phi K^0_S$

This mode was reconstructed for the secondary decays $\phi \to K^+K^-$ and $K^0_S \to \pi^+\pi^-$. The reconstruction of the ϕ and K^0_S mesons were described in Sections 5.5 and 5.4, respectively. The selection variables used for the selection of this mode are listed in Table 6.7. This table indicates the selection variables that were optimised according to the method described in Section 5.10, in order to obtain the highest significance for the measurement of the branching fraction.

6.2.1 Study of the Signal MC for $B^0 \to \phi K^0_S$

The use of signal MC data was motivated in Section 6.1.1. The distributions of $m_{\rm ES}$ and ΔE from the signal MC for this mode are shown in Figure 6.6. Also shown is the ϕ meson mass distribution from the same signal MC data. The final optimised selection variable cuts that are listed in Table 6.10 were used to produce these distributions.

6.2.2 Background Characterisation for $B^0 \to \phi K^0_S$

The values of the Argus function parameter ξ, which were obtained from the fits to the $m_{\rm ES}$ background distributions for different values of the $|\cos\theta_{\rm T}|$ selection variable, are shown in Figure 6.7. This characterisation is shown for two different sets of selection cuts for each of the on-resonance and off-resonance data. These include selection cuts on the ϕ meson resonance mass, the ϕ meson helicity angle $|\cos\theta_{\rm H}|$ selection, the $c\tau/\sigma_{c\tau}$ selection on the flight length of the K^0_S meson, and a loose and a tight selection cut on the Fisher discriminant as summarised in Table 6.8. The same set of selection criteria were applied for the characterisation of the two parameters C and D of the quadratic fit to the ΔE background distribution. The values of C and D for these characterisations are shown in Figure 6.8.

The top plot in Figure 6.7 shows the results of the fits to the sum of the $m_{\rm ES}$ background distributions in the upper and lower ΔE sidebands. The bottom plot in this figure shows the results of the characterisation of the $m_{\rm ES}$ background distribution for each of the upper and lower ΔE sidebands individually, for on-resonance data only.

Due to the lack of statistics from off-resonance data in the background distributions in this analysis, only the characterisations from the on-resonance data were used for the parameters ξ, C, and D. The chosen value for each of these parameters was not obtained by using a fit to the values shown in Figures 6.7 and 6.8. This was because it was found that the variation of their values between the large systematic errors assigned to them, made an insignificant difference to the value of the ratio $\mathcal{A}$, and hence, the estimation of the number of background events in the signal. Figures 6.7

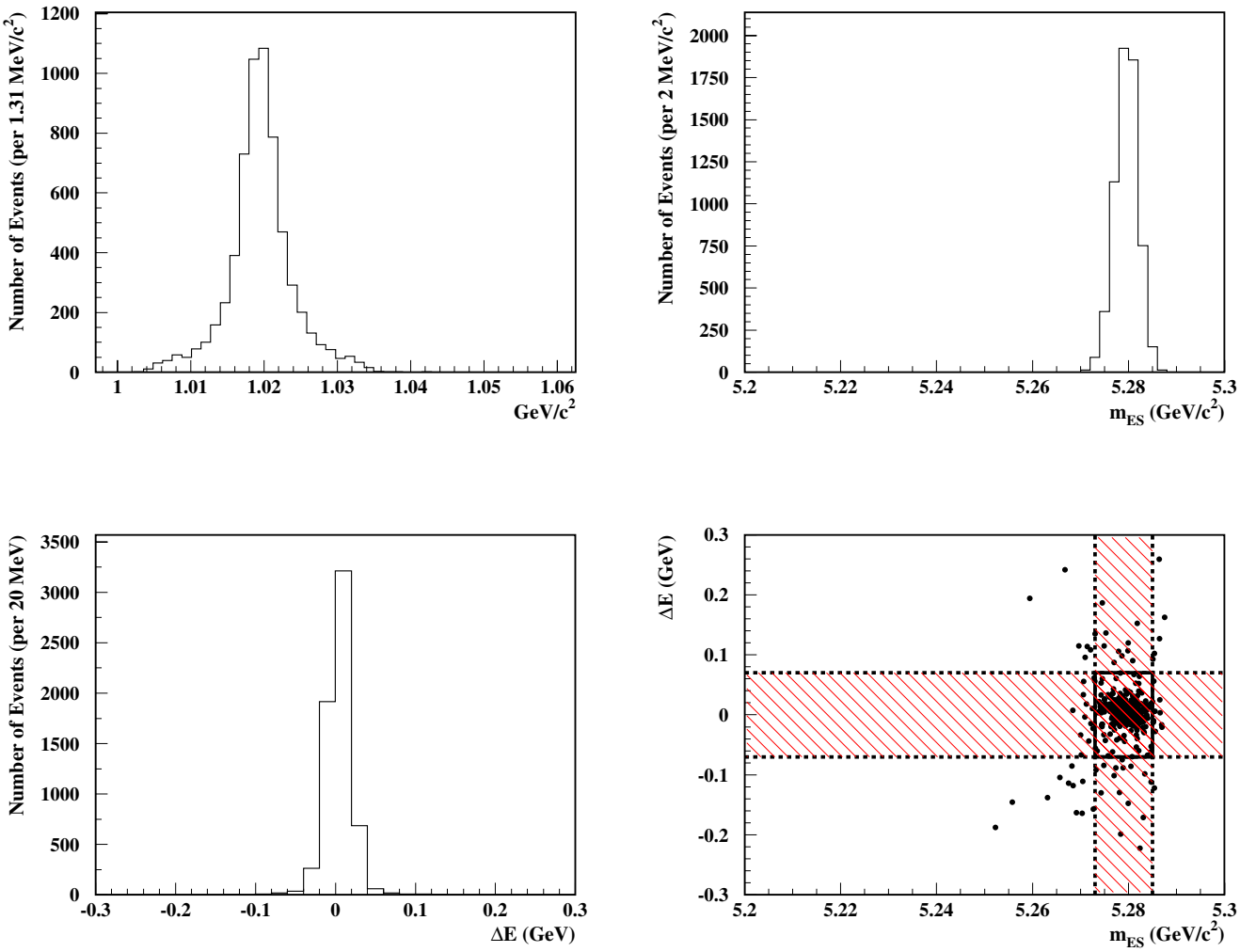

Figure 6.6: *The m_{ES} (top right) and ΔE (bottom left) distributions for 20,000 $B^0 \to \phi K^0_S$ signal MC events, where $\phi \to K^+K^-$ and $K^0_S \to \pi^+\pi^-$. The shaded bands in the 2-D scatter plot of the m_{ES}-ΔE plane (bottom right), show the constraint of the signal region of each variable on the distribution of the other. Also shown is the ϕ meson mass distribution (top left) from the same signal MC data, for the candidates in the signal region.*

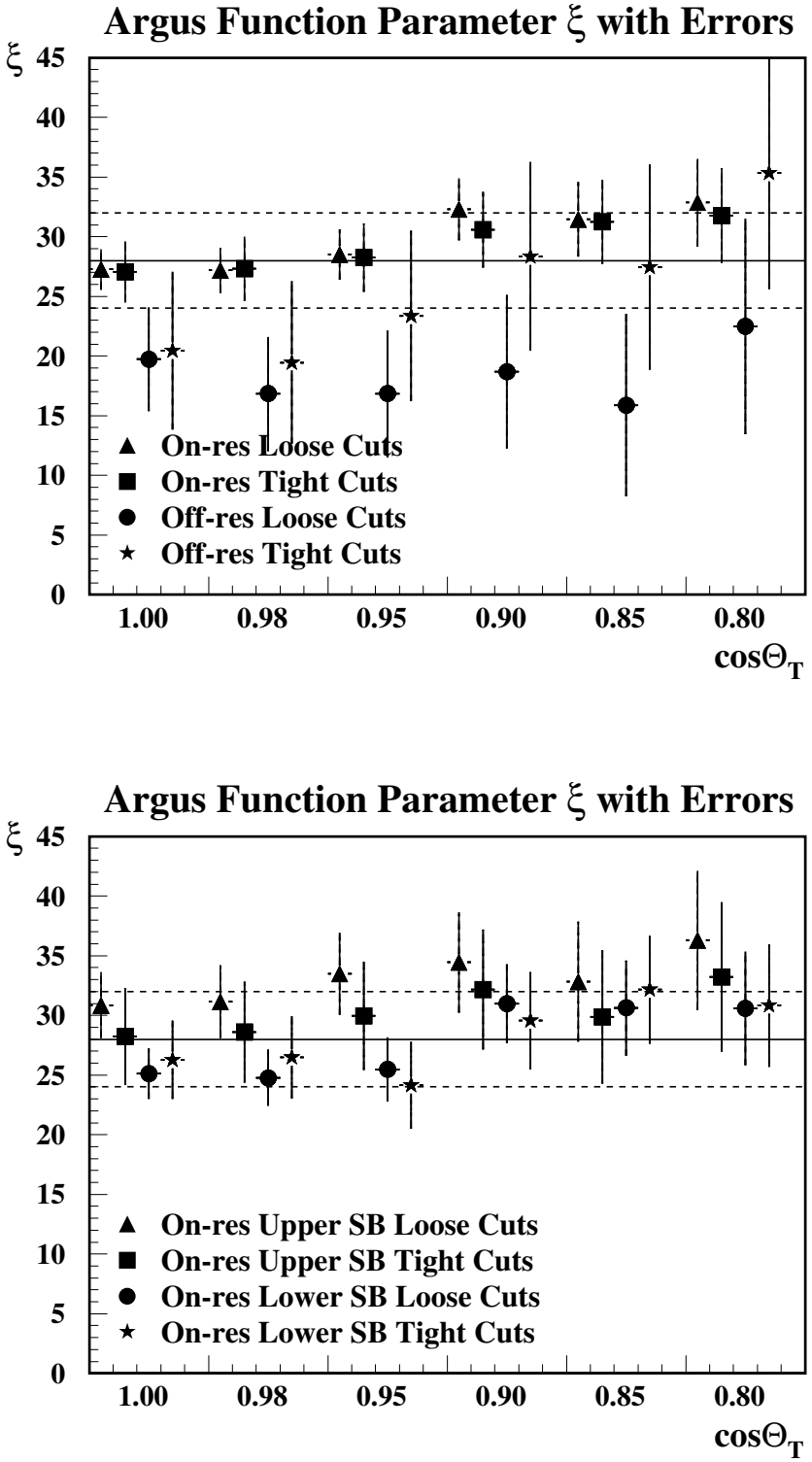

Figure 6.7: *The values of the Argus function parameter ξ, obtained by fitting the m_{ES} distributions in the upper and lower ΔE sidebands together (top), and separately (bottom), for the $B^0 \to \phi K^0_S$ analysis. On-resonance and off-resonance data were used with a loose and a tight selection cut on the Fisher discriminant.*

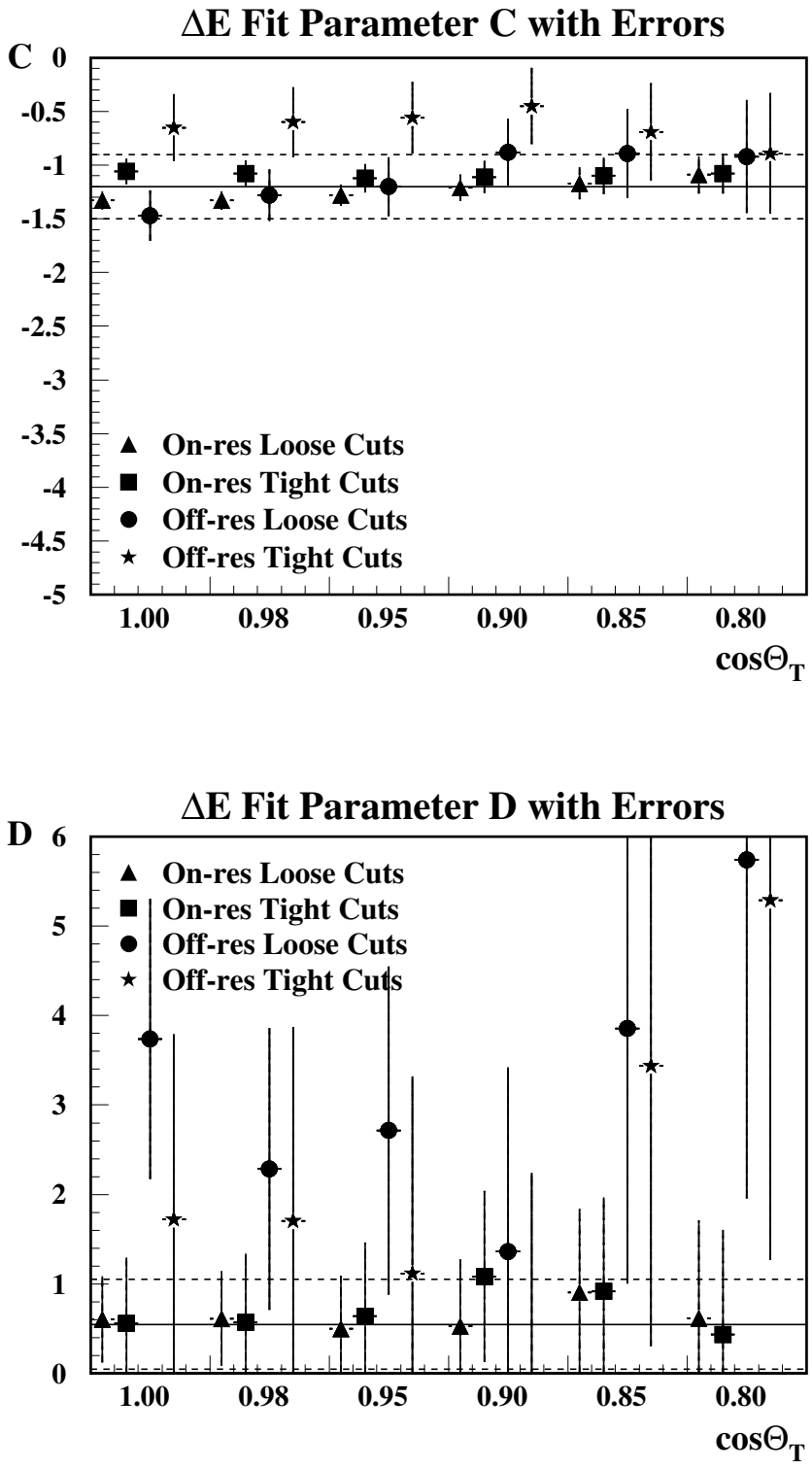

Figure 6.8: *The values of the parameters C (top) and D (bottom), of the quadratic fits to the ΔE background distributions for the $B^0 \to \phi K^0_S$ analysis. On-resonance and off-resonance data were used with a loose and a tight selection cut on the Fisher discriminant.*

Table 6.8: *The selection variables used for the background characterisations of m_{ES} and ΔE for the $B^0 \to \phi K^0_S$ analysis. The thrust angle $|\cos\theta_T|$ selections were applied with both the loose and the tight selection on the Fisher discriminant.*

	Selections	
Selection Variable	Loose	Tight
Fisher discriminant	< 1.5	< 0.5
ϕ meson resonance mass	1020 ± 200 MeV/c^2	
ϕ meson helicity angle $\lvert\cos\theta_{\rm H}\rvert$	> 0.1	
K^0_S meson flight length $c\tau/\sigma_{c\tau}$	> 0.0	
Track particle ID for kaons	`notApion` kaon ID	
K^0_S meson mass	498 ± 8 MeV/c^2	
Thrust angle $\lvert\cos\theta_{\rm T}\rvert$	$< 0.80,\ 0.85,\ 0.90,\ 0.95,\ 0.98,\ 1.00$	

and 6.8 show the chosen value (solid line) for each of the characterised parameters, which is a best estimate from the values obtained, with the assigned systematic errors (dashed lines). These results are summarised in Table 6.9. The calculated value of $\mathcal{A}$ for this analysis is 0.0477 ± 0.0034. Note that, these results are consistent with the results of the background characterisation for the $B^0 \to D^-\pi^+$ analysis presented in Table 6.3.

Table 6.9: *Results of the background characterisations of m_{ES} and ΔE for the $B^0 \to \phi K^0_S$ analysis.*

Background Distribution	Fitted Function	Fit Parameter	Value and Systematic Error
$m_{\rm ES}$	Argus	ξ	28 ± 4
ΔE	Quadratic	C	-1.2 ± 0.3
ΔE	Quadratic	D	0.55 ± 0.5

6.2.3 Cut-Optimisation for $B^0 \to \phi K^0_S$

The best available branching fraction that was used in Equation 5.11 to estimate N_S was [17],

$$\begin{aligned} & \mathcal{B}_{\rm ba}((B^0 \to \phi K^0) \times (\phi \to K^+K^-) \times (K^0 \to K^0_S) \times (K^0_S \to \pi^+\pi^-)) \\ = \; & (8.0 \times 10^{-6}) \times 0.492 \times 0.500 \times 0.686 \\ = \; & 1.35 \times 10^{-6}\,. \end{aligned} \tag{6.2}$$

The branching fraction of $\mathcal{B}(B^0 \to \phi K^0) = 8.0 \times 10^{-6}$ is consistent with the published measurement from the *BABAR* experiment, $\mathcal{B}(B^0 \to \phi K^0) = (8.1^{+3.1}_{-2.5}(\text{stat.}) \pm 0.8(\text{syst.})) \times 10^{-6}$ [58], using the same data that were used for the analyses presented here.

The final set of selection variables are listed in Table 6.10.

6.2.4 Study of the Backgrounds in $B^0 \to \phi K^0_S$

Using the final set of optimised selection variable cuts shown in Table 6.10, the number of reconstructed B meson candidates in the signal region, $N_{\rm sig}$, and in the sideband

Table 6.10: *The final set of selection variable cuts used in the* $B^0 \to \phi K^0_S$ *analysis.*

Selection Variable	Cut Value
Thrust angle $\lvert\cos\theta_{\rm T}\rvert$	< 0.95
Fisher discriminant	< 0.1
Track particle ID for kaons	`notApion` kaon ID
K^0_S meson mass	498 ± 8 MeV/c^2
K^0_S meson flight length $c\tau/\sigma_{c\tau}$	> 8.0
ϕ meson resonance mass	1020 ± 15 MeV/c^2
ϕ meson helicity angle $\lvert\cos\theta_{\rm H}\rvert$	> 0.2
Beam-energy constrained $\lvert\Delta E\rvert$	< 70 MeV
Beam-energy substituted mass, $m_{\rm ES}$	5279 ± 6 MeV/c^2

region, $N_{\rm sb}$, were counted for every event in off-resonance data, and in the generic MC and charmless hadronic $B\bar{B}$ MC data introduced in Sections 4.4.2 and 4.4.3, respectively.

The results are shown in Table 6.11. A study of the MC decay trees of the four events from the charmless hadronic $B\bar{B}$ MC data sample, and the two events from the generic $B^0\bar{B}^0$ MC data sample, which are found in the signal region, shows that they all include the signal mode $B^0 \to \phi K^0_S$, where $\phi \to K^+K^-$ and $K^0_S \to \pi^+\pi^-$. No B meson backgrounds, therefore, were taken into account for this analysis.

Table 6.11: *The number of reconstructed B meson candidates in the signal region, N_{sig}, and sideband region, N_{sb}, in off-resonance data, and in the generic MC and charmless hadronic $B\bar{B}$ MC data. The number of signal events, N_{true}, are also given. $\mathcal{L}$ is the equivalent integrated luminosity for the data samples used.*

Data	$\mathcal{L}$ (fb^{-1})	$N_{\rm sig}$	$N_{\rm sb}$	$N_{\rm true}$
Charmless $B\bar{B}$ MC data	21	4	1	4
Generic $B^0\bar{B}^0$ MC data	5.0	2	0	2
Generic B^+B^- MC data	8.3	0	0	–
Generic $c\bar{c}$ MC data	5.0	2	22	–
Generic uds MC data	5.7	2	14	–
Off-resonance data	2.6	0	11	–

6.2.5 Branching Fraction of $B^0 \to \phi K^0$

Using the final set of optimised selection variable cuts shown in Table 6.10, the number of reconstructed B meson candidates in the signal region, $N_{\rm sig}$, was counted for every event in on-resonance data. The number of background events in the signal region, N_B, was estimated using Equation 5.10 using only the odd numbered events from on-resonance data and scaling up by a factor of two. The number of signal events, N_S, was calculated using Equation 5.13. The branching fraction was calculated using Equation 5.14.

The final results are summarised in Table 6.12. The final branching fraction of $\mathcal{B}(B^0 \to \phi K^0) = (9.3 \pm 3.4(\text{stat.}) \pm 1.1(\text{syst.})) \times 10^{-6}$ was obtained using the secondary branching fractions $\mathcal{B}(\phi \to K^+K^-) = 0.492 \pm 0.007$, $\mathcal{B}(K^0 \to K^0_S) = 0.5$, and $\mathcal{B}(K^0_S \to \pi^+\pi^-) = 0.686 \pm 0.003$. The significance of this branching fraction measurement is 4.9σ. This measurement is in good agreement with that published by the *BABAR* experiment,

Table 6.12: *The final results for the $B^0 \to \phi K^0_S$ analysis. Unless otherwise stated, the first error is the statistical error and the second is the systematic error.*

Number of events in signal region, $N_{\rm sig}$	15
Number of events in sideband region, $N_{\rm sb}$	90
Ratio of sideband to signal region events, $\mathcal{A}$	0.0477±0.0034(syst.)
Number of background events in signal region, N_B	$4.3 \pm 0.6 \pm 0.3$
Number of signal events in signal region, N_S	10.7
Number of B^0 and $\bar{B}^0$ mesons, equal to $N_{B\bar{B}}$	$(22.55 \pm 0.36(\text{total})) \times 10^6$
Corrected Selection efficiency, $\epsilon_{\rm c}$	$30.4 \pm 0.4 \pm 3.3$ %
Secondary Branching Fractions, $\mathcal{B}_{\rm sec}$	$0.492 \times 0.500 \times 0.686$
Branching fraction, $\mathcal{B}(B^0 \to \phi K^0)$	$(9.3 \pm 3.4 \pm 1.1) \times 10^{-6}$

$\mathcal{B}(B^0 \to \phi K^0) = (8.1^{+3.1}_{-2.5}(\text{stat.}) \pm 0.8(\text{syst.})) \times 10^{-6}$ [58], which was obtained using a maximum likelihood fit method.

The quoted significance was calculated following the method described in reference [59]. This significance represents the difference between the observed number of events in the signal region, $N_{\rm sig}$, and the estimated number of background events in the signal region, N_B, and is calculated as a multiple of σ, where $\sigma = \sqrt{\text{variance}}$. The variance of this difference is the combination of the error on the estimated number of background events in the signal region, N_B, and its error. For this analysis the variance is given by,

$$\text{variance} = 4.3 + 0.6^2 + 0.3^2 \,. \tag{6.3}$$

The significance is then given by,

$$\text{significance} = \frac{15 - 4.3}{\sigma}\,. \tag{6.4}$$

Figure 6.9 shows the $m_{\rm ES}$ and ΔE distributions from on-resonance data, which were obtained using the final set of optimised selection variable cuts listed in Table 6.10.

6.3 Analysis Details of $B^0 \to K^{*+}\pi^-$

This mode was reconstructed for the secondary decays $K^{*+} \to K^0\pi^+$, $K^0 \to K^0_S$, and $K^0_S \to \pi^+\pi^-$. The reconstruction of K^{*+} mesons was described in Section 5.6. The selection variables used for the selection of this mode are listed in Table 6.13. This table indicates the selection variables that were optimised according to the method described in Section 5.10, in order to obtain the highest significance for the measurement of the branching fraction.

6.3.1 Study of the Signal MC for $B^0 \to K^{*+}\pi^-$

The use of signal MC data was motivated in Section 6.1.1. The distributions of $m_{\rm ES}$ and ΔE from the signal MC for this mode are shown in Figure 6.10. Also shown is the K^{*+} meson mass distribution from the same signal MC data. The final optimised selection variable cuts that are listed in Table 6.16 were used to produce these distributions.

6.3.2 Background Characterisation for $B^0 \to K^{*+}\pi^-$

The values of the Argus function parameter ξ, which were obtained from the fits to the $m_{\rm ES}$ background distributions for different values of the $|\cos\theta_{\rm T}|$ selection variable, are shown in Figure 6.11. This characterisation is shown for two different sets of selection cuts for each of the on-resonance and off-resonance data. These include selection cuts

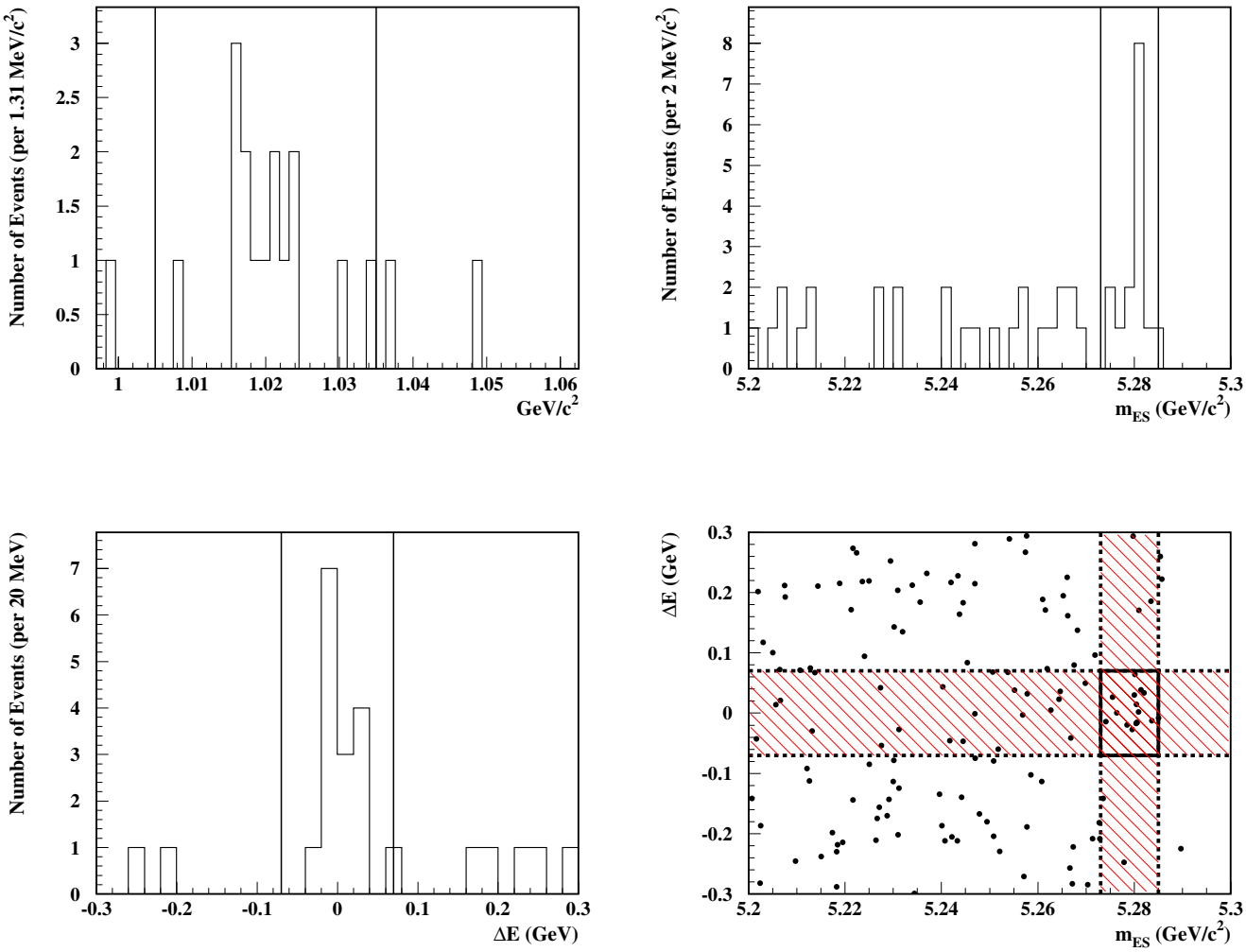

Figure 6.9: *The m_{ES} (top right) and ΔE (bottom left) distributions obtained from on-resonance data using the final set of optimised selection variable cuts listed in Table 6.10 for the $B^0 \to \phi K^0_S$ analysis. Also shown is the ϕ meson mass distribution (top left) from the same data, for the candidates in the signal region.*

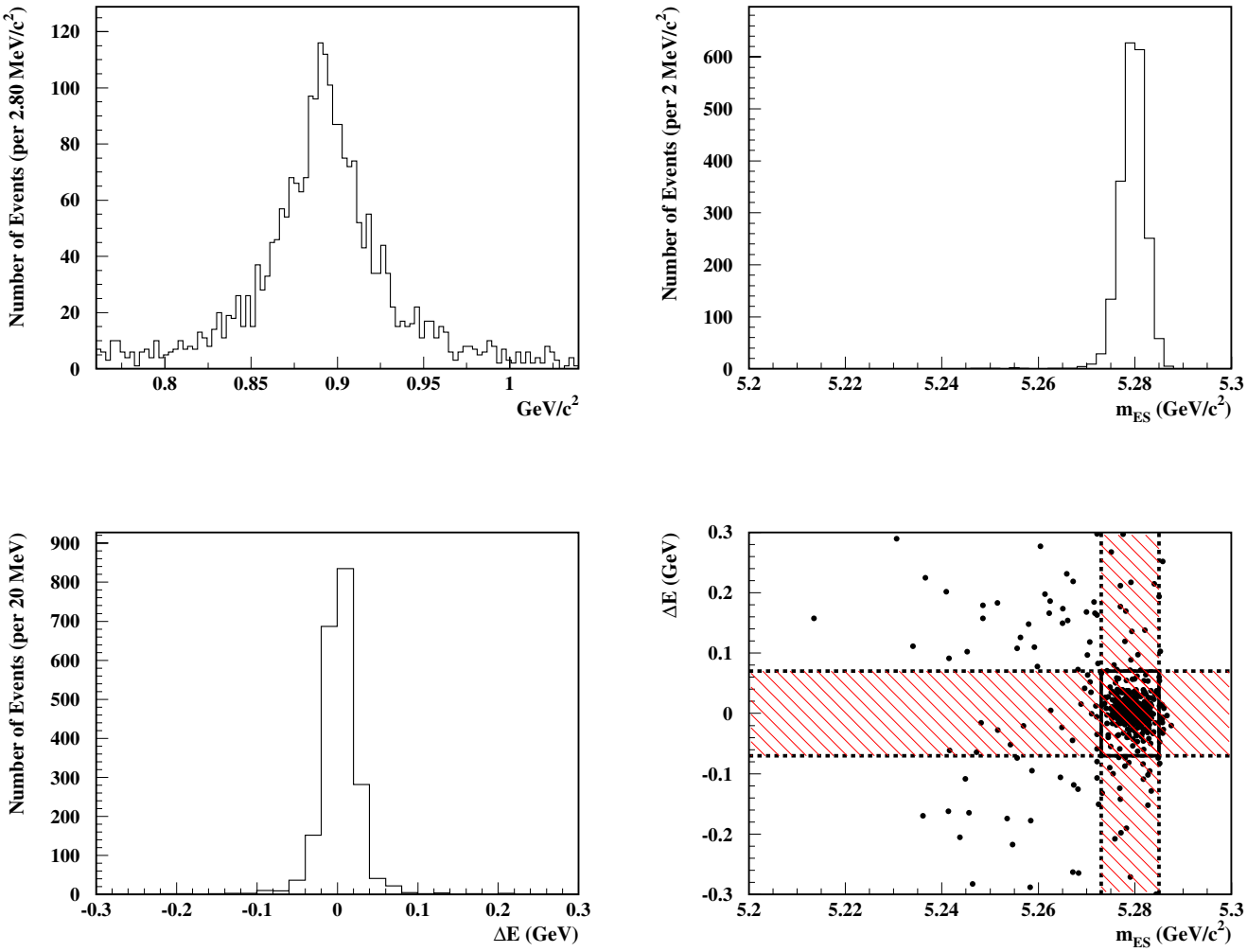

Figure 6.10: *The m_{ES} (top right) and ΔE (bottom left) distributions for 20,000 $B^0 \to K^{*+}\pi^-$ signal MC events, where $K^{*+} \to K^0_S\pi^+$ and $K^0_S \to \pi^+\pi^-$. The shaded bands in the 2-D scatter plot of the m_{ES}-ΔE plane (bottom right), show the constraint of the signal region of each variable on the distribution of the other. Also shown is the K^{*+} meson mass distribution (top left) from the same signal MC data, for the candidates in the signal region.*

Table 6.13: *The selection variables used for the selection of the* $B^0 \to K^{*+}\pi^-$ *mode, where* $K^{*+} \to K^0_S\pi^+$.

Selection Variable	Optimised
Thrust angle $\lvert\cos\theta_{\rm T}\rvert$	Optimised
Fisher discriminant	Optimised
Track particle ID for pions	Optimised
K^0_S meson mass	Not optimised
K^0_S meson flight length $c\tau/\sigma_{c\tau}$	Optimised
K^{*+} meson resonance mass	Optimised
K^{*+} meson helicity angle $\lvert\cos\theta_{\rm H}\rvert$	Optimised
Beam-energy constrained ΔE	Not optimised
Beam-energy substituted mass, $m_{\rm ES}$	Not optimised

on the K^{*+} meson resonance mass, the K^{*+} meson helicity angle $\lvert\cos\theta_{\rm H}\rvert$ selection, the $c\tau/\sigma_{c\tau}$ selection on the flight length of the K^0_S meson, and a loose and a tight selection cut on the Fisher discriminant as summarised in Table 6.14. The same set of selection criteria were applied for the characterisation of the two parameters C and D of the quadratic fit to the ΔE background distribution. The values of C and D for these characterisations are shown in Figure 6.12.

The top plot in Figure 6.11 shows the results of the fits to the sum of the $m_{\rm ES}$ background distributions in the upper and lower ΔE sidebands. The bottom plot in this figure shows the results of the characterisation of the $m_{\rm ES}$ background distribution for each of the upper and lower ΔE sidebands individually, for on-resonance data only.

The chosen value for each of the parameters ξ, C, and D, was not obtained by using

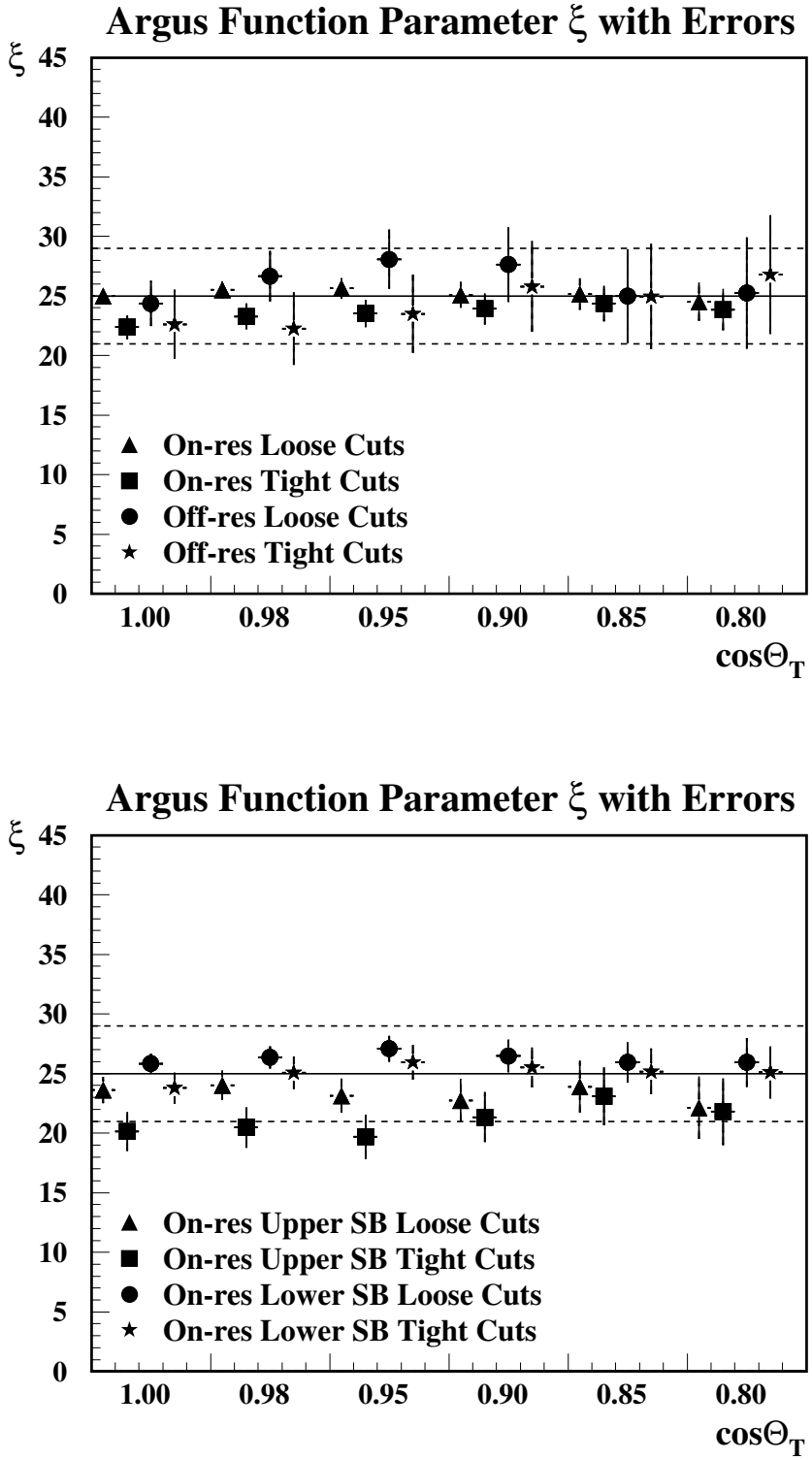

Figure 6.11: *The values of the Argus function parameter ξ, obtained by fitting the m_{ES} distributions in the upper and lower ΔE sidebands together (top), and separately (bottom), for the $B^0 \to K^{*+}\pi^-$ analysis. On-resonance and off-resonance data were used with a loose and a tight selection cut on the Fisher discriminant.*

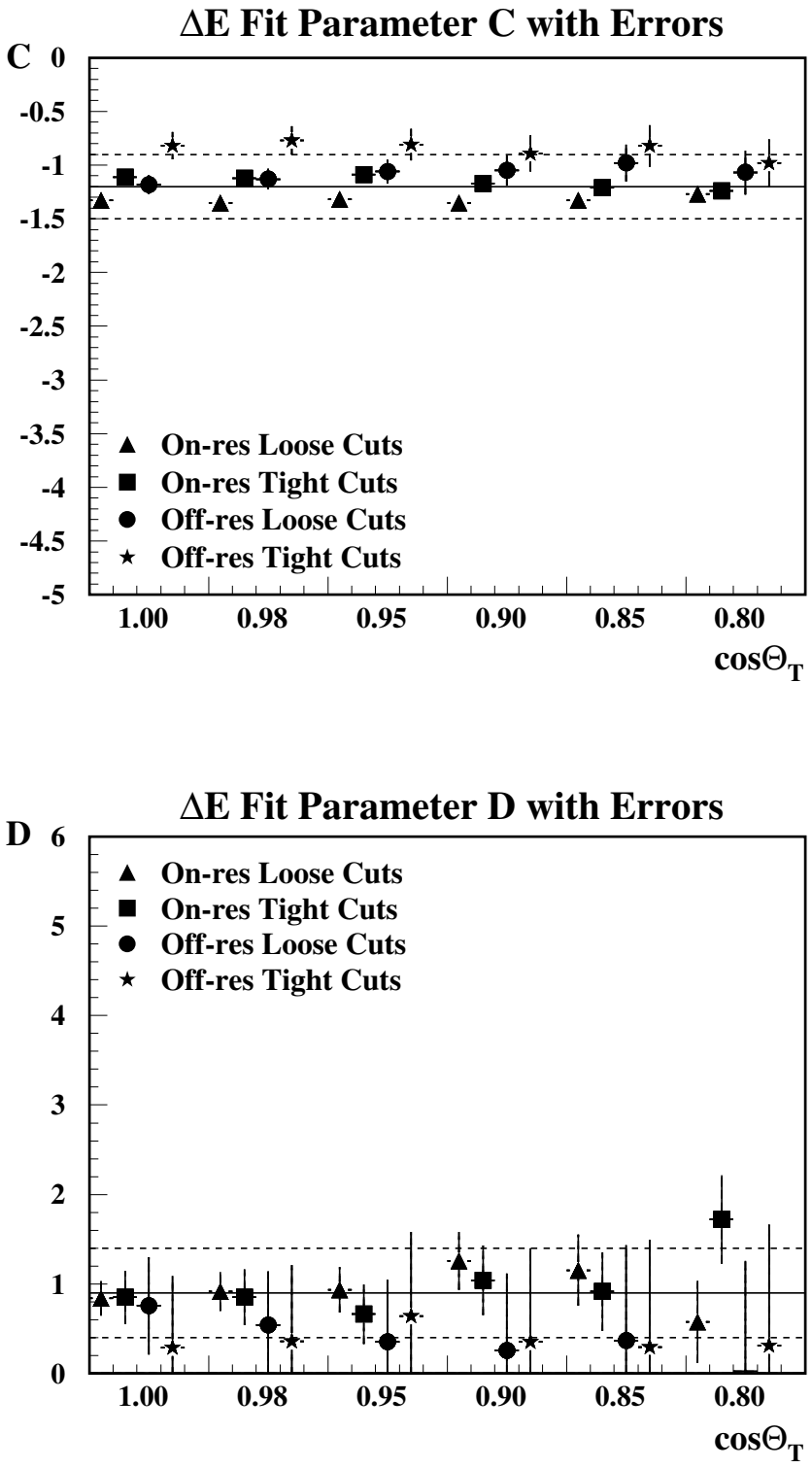

Figure 6.12: *The values of the parameters C (top) and D (bottom), of the quadratic fits to the ΔE background distributions for the $B^0 \to K^{*+}\pi^-$ analysis. On-resonance and off-resonance data were used with a loose and a tight selection cut on the Fisher discriminant.*

Table 6.14: *The selection variables used for the background characterisations of m_{ES} and ΔE for the $B^0 \to K^{*+}\pi^-$ analysis. The thrust angle $|\cos\theta_T|$ selections were applied with both the loose and the tight selection on the Fisher discriminant.*

	Selections	
Selection Variable	Loose	Tight
Fisher discriminant	< 1.5	< 0.5
K^{*+} meson resonance mass	$892\pm$ 140 MeV/c^2	
K^{*+} meson helicity angle $\lvert\cos\theta_{\rm H}\rvert$	> 0.1	
K^0_S meson flight length $c\tau/\sigma_{c\tau}$	> 0.0	
Track particle ID for pions	not `tight` kaon ID	
K^0_S meson mass	498 ± 8 MeV/c^2	
Thrust angle $\lvert\cos\theta_{\rm T}\rvert$	< 0.80, 0.85, 0.90, 0.95, 0.98, 1.00	

a fit to the values shown in Figures 6.11 and 6.12. This was because it was found that the variation of their values between the large systematic errors assigned to them, made an insignificant difference to the value of the ratio $\mathcal{A}$, and hence, the estimation of the number of background events in the signal. Figures 6.11 and 6.12 show the chosen value (solid line) for each of the characterised parameters, which is a best estimate from the values obtained, with the assigned systematic errors (dashed lines). These results are summarised in Table 6.15. The calculated value of $\mathcal{A}$ for this analysis is 0.0453 ± 0.0034. Note that, these results are consistent with the results of the background characterisations for the $B^0 \to D^-\pi^+$ and the $B^0 \to \phi K^0_S$ analyses presented in Tables 6.3 and 6.9, respectively.

Table 6.15: *Results of the background characterisations of m_{ES} and ΔE for the $B^0 \to K^{*+}\pi^-$ analysis.*

Background Distribution	Fitted Function	Fit Parameter	Value and Systematic Error
$m_{\rm ES}$	Argus	ξ	25 ± 4
ΔE	Quadratic	C	-1.2 ± 0.3
ΔE	Quadratic	D	0.9 ± 0.5

6.3.3 Cut-Optimisation for $B^0 \to K^{*+}\pi^-$

The best available branching fraction that was used in Equation 5.11 to estimate N_S was [17],

$$\begin{aligned} & \mathcal{B}_{\rm ba}((B^0 \to K^{*+}\pi^-) \times (K^{*+} \to K^0\pi^+) \times (K^0 \to K^0_S) \times (K^0_S \to \pi^+\pi^-)) \\ = \; & (22.0 \times 10^{-6}) \times 0.666 \times 0.500 \times 0.686 \\ = \; & 5.03 \times 10^{-6}\,. \end{aligned} \tag{6.5}$$

The branching fraction of $\mathcal{B}(B^0 \to K^{*+}\pi^-) = 22.0 \times 10^{-6}$ is an unpublished measurement made by the CLEO experiment [50]. The branching fraction $\mathcal{B}(K^{*+} \to K^0\pi^+) = 2/3$ is obtained using the Clebsch-Gordan coefficients.

The final set of selection variables are listed in Table 6.16.

6.3.4 Study of the Backgrounds in $B^0 \to K^{*+}\pi^-$

Using the final set of optimised selection variable cuts shown in Table 6.16, the number of reconstructed B meson candidates in the signal region, $N_{\rm sig}$, and in the sideband region, $N_{\rm sb}$, were counted for every event in off-resonance data, and in the generic

Table 6.16: *The final set of selection variable cuts used in the* $B^0 \to K^{*+}\pi^-$ *analysis.*

Selection Variable	Cut Value
Thrust angle $\lvert\cos\theta_{\rm T}\rvert$	< 0.85
Fisher discriminant	< -0.2
Track particle ID for pions	not `tight` kaon ID
K^0_S meson mass	498 ± 8 MeV/c^2
K^0_S meson flight length $c\tau/\sigma_{c\tau}$	> 5.0
K^{*+} meson resonance mass	892 ± 60 MeV/c^2
K^{*+} meson helicity angle $\lvert\cos\theta_{\rm H}\rvert$	> 0.4
Beam-energy constrained $\lvert\Delta E\rvert$	< 70 MeV
Beam-energy substituted mass, $m_{\rm ES}$	5279 ± 6 MeV/c^2

MC and charmless hadronic $B\bar{B}$ MC data introduced in Sections 4.4.2 and 4.4.3, respectively.

The results are shown in Table 6.17. A study of the MC decay trees of the six events from the charmless hadronic $B\bar{B}$ MC data sample, which are found in the signal region, shows that they all include the signal mode $B^0 \to K^{*+}\pi^-$, where $K^{*+} \to K^0_S\pi^+$ and $K^0_S \to \pi^+\pi^-$. A study of 17,000 exclusive MC events of the non-resonant decay $B^0 \to K^0_S\pi^+\pi^-$, where $K^0_S \to \pi^+\pi^-$, using the optimised selection cuts in Table 6.16, resulted in 42 reconstructed B meson candidates in the signal region. This represents a selection efficiency of 0.25 %.

Using the branching fraction of $\mathcal{B}(B^0 \to K^0\pi^+\pi^-) = 5 \times 10^{-5}$ [57], and taking into account the secondary branching fractions for $K^0 \to K^0_S$ and $K^0_S \to \pi^+\pi^-$, the number of expected background events due to $B^0 \to K^0_S\pi^+\pi^-$ is 1 event. As with the $B^0 \to$

Table 6.17: *The number of reconstructed B meson candidates in the signal region, N_{sig}, and sideband region, N_{sb}, in off-resonance data, and in the generic MC and charmless hadronic $B\bar{B}$ MC data. The number of signal events, N_{true}, are also given. $\mathcal{L}$ is the equivalent integrated luminosity for the data samples used.*

Data	$\mathcal{L}$ (fb^{-1})	$N_{\rm sig}$	$N_{\rm sb}$	$N_{\rm true}$
Charmless $B\bar{B}$ MC data	21	6	2	6
Generic $B^0\bar{B}^0$ MC data	5.0	0	1	–
Generic B^+B^- MC data	8.3	0	1	–
Generic $c\bar{c}$ MC data	5.0	4	26	–
Generic uds MC data	5.7	1	40	–
Off-resonance data	2.6	1	29	–

$D^-\pi^+$ analysis, this background adds a negligible systematic error to the measurement of $\mathcal{B}(B^0 \to K^{*+}\pi^-)$ and is not taken into account.

6.3.5 Branching Fraction of $B^0 \to K^{*+}\pi^-$

Using the final set of optimised selection variable cuts shown in Table 6.16, the number of reconstructed B meson candidates in the signal region, $N_{\rm sig}$, was counted for every event in on-resonance data. The number of background events in the signal region, N_B, was estimated using Equation 5.10 using only the odd numbered events from on-resonance data and scaling up by a factor of two. The number of signal events, N_S, was calculated using Equation 5.13. The branching fraction was calculated using Equation 5.14.

The final results are summarised in Table 6.18. The final branching fraction of $\mathcal{B}(B^0 \to K^{*+}\pi^-) = (20.8 \pm 9.3(\text{stat.}) \pm 2.1(\text{syst.})) \times 10^{-6}$ was obtained using the

Table 6.18: *The final results for the $B^0 \to K^{*+}\pi^-$ analysis. Unless otherwise stated, the first error is the statistical error and the second is the systematic error.*

Number of events in signal region, $N_{\rm sig}$	22
Number of events in sideband region, $N_{\rm sb}$	248
Ratio of sideband to signal region events, $\mathcal{A}$	0.0453±0.0034(syst.)
Number of background events in signal region, N_B	$11.2 \pm 1.0 \pm 0.8$
Number of signal events in signal region, N_S	10.8
Number of B^0 and $\bar{B}^0$ mesons, equal to $N_{B\bar{B}}$	$(22.55 \pm 0.36(\text{total})) \times 10^6$
Corrected Selection efficiency, $\epsilon_{\rm c}$	$10.1 \pm 0.2 \pm 0.6$ %
Secondary Branching Fractions, $\mathcal{B}_{\rm sec}$	$0.666 \times 0.500 \times 0.686$
Branching fraction, $\mathcal{B}(B^0 \to K^{*+}\pi^-)$	$(20.8 \pm 9.3 \pm 2.1) \times 10^{-6}$

secondary branching fractions $\mathcal{B}(K^{*+} \to K^0\pi^+) = \frac{2}{3}$, $\mathcal{B}(K^0 \to K^0_S) = 0.5$, and $\mathcal{B}(K^0_S \to \pi^+\pi^-) = 0.686 \pm 0.003$. The significance of this branching fraction measurement is 3.0σ, which was calculated as described at the end of Section 6.2.5. The calculated upper limit for this analysis is $\mathcal{B}(B^0 \to K^{*+}\pi^-) < 38.9 \times 10^{-6}$. An unpublished measurement of this branching fraction from the CLEO experiment is $\mathcal{B}(B^0 \to K^{*+}\pi^-) = (23^{+9}_{-7}(\text{stat.}) \pm 3(\text{syst.})) \times 10^{-6}$ [50], which is consistent with the measurement presented here.

Figure 6.13 shows the $m_{\rm ES}$ and ΔE distributions from on-resonance data, which were obtained using the final set of optimised selection variable cuts listed in Table 6.16.

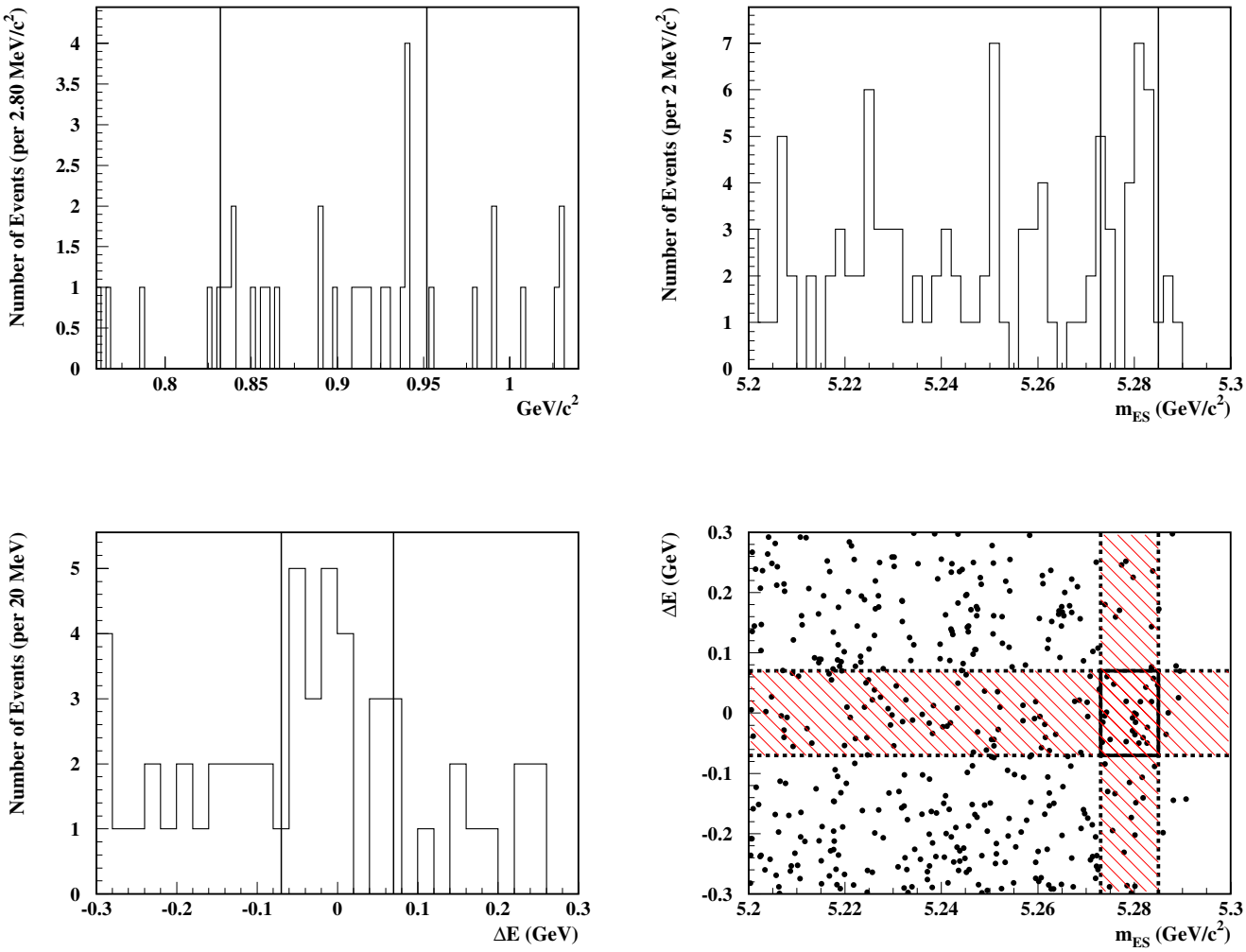

Figure 6.13: *The m_{ES} (top right) and ΔE (bottom left) distributions obtained from on-resonance data using the final set of optimised selection variable cuts listed in Table 6.16 for the $B^0 \to K^{*+}\pi^-$ analysis. Also shown is the K^{*+} meson mass distribution (top left) from the same data, for the candidates in the signal region.*

6.4 Statistical and Systematic Errors

The measured branching fractions have been calculated using Equation 5.14. The statistical error on the branching fractions, $\sigma_{\mathcal{B}(\text{stat.})}$, is due to the number of events observed in the signal and the sideband regions, N_{sig} and N_{sb}, respectively. Using Equations 5.14, 5.13, and 5.10, $\sigma_{\mathcal{B}(\text{stat.})}$ is given by,

$$\sigma_{\mathcal{B}(\text{stat.})} = \frac{(N_{\text{sig}} + \mathcal{A}\,2N_B)^{\frac{1}{2}}}{N_{B\bar{B}}\,\epsilon_{\text{c}}\,\mathcal{B}_{\text{sec}}}\,. \tag{6.6}$$

The systematic errors for the analyses presented here are due to the uncertainties in the estimation of the number of background events in the signal region N_B, and hence the signal yield N_S, and the determination of the corrected signal efficiency ϵ_{c}. In addition, there are systematic uncertainties due to the determination of the number of $B\bar{B}$ events produced, $N_{B\bar{B}}$, and the error on the product of the secondary branching fractions $\mathcal{B}_{\text{sec}}$.

The systematic error for the background estimation procedure, and hence the determination of the signal yield, is derived from the uncertainty in the determination of the ratio $\mathcal{A}$. From Equations 5.13 and 5.10, the fractional error on the signal yield is given by,

$$\frac{\Delta N_S}{N_S} = \frac{\Delta\mathcal{A}\,2N_{\text{sb}}}{N_{\text{sig}} - \mathcal{A}\,2N_{\text{sb}}}\,. \tag{6.7}$$

The error on $\mathcal{A}$ was obtained by varying the values of the fit parameters ξ, C, and D, which were introduced in Section 5.9, between their estimated errors, and calculating $\mathcal{A}$. The biggest deviation of the value of $\mathcal{A}$ from that obtained using the central values of these fit parameters, was taken as the error $\Delta\mathcal{A}$. For all three analyses presented here, $\Delta\mathcal{A} = 0.0034$.

The systematic error from the determination of the corrected signal efficiency, ϵ_{c}, which is obtained from signal MC, has two contributions. The first is from the statistical error on the number of signal MC events observed in the signal region, $N_{S_{\text{MC}}}$, and is

given by,

$$\frac{\sqrt{N_{S_{\rm MC}}}}{N_{\rm MC}} \times \text{correction factors}\,, \tag{6.8}$$

where $N_{\rm MC}$ is the total number of signal MC events used in the analyses (20,000 events).

The second contribution is a systematic effect from the errors of the efficiency correction factors listed in Table 5.6. These errors were added in quadrature to give the systematic error on $\epsilon_{\rm c}$. The systematic error and the statistical contribution given in Equation 6.8, were then added in quadrature to obtain the total error on $\epsilon_{\rm c}$,

$$\Delta\epsilon_{\rm c} = \left(\left(\frac{\sqrt{N_{S_{\rm MC}}}}{N_{\rm MC}} \prod_i i \right)^2 + \left(\epsilon_{\rm c} \sqrt{\sum_i (\Delta i)^2} \right)^2 \right)^{\frac{1}{2}}\,, \tag{6.9}$$

where Δi is the error on the efficiency correction factor i.

The overall systematic error on the branching fraction measurements, $\sigma_{\mathcal{B}(\rm syst.)}$, was calculated by adding all of the four contributions in quadrature and is given by,

$$\sigma_{\mathcal{B}(\rm syst.)} = \left(\left(\frac{\Delta N_S}{N_S} \right)^2 + \left(\frac{\Delta\epsilon_{\rm c}}{\epsilon_{\rm c}} \right)^2 + \left(\frac{\Delta N_{B\bar{B}}}{N_{B\bar{B}}} \right)^2 + \left(\frac{\Delta\mathcal{B}_{\rm sec}}{\mathcal{B}_{\rm sec}} \right)^2 \right)^{\frac{1}{2}} \mathcal{B}\,. \tag{6.10}$$

The final branching fraction measurements were obtained using Equations 5.14, 6.6 for the statistical error, and 6.10 for the systematic error. The final relation is,

$$\mathcal{B} = \frac{N_S}{N_{B\bar{B}}\,\epsilon_{\rm c}\,\mathcal{B}_{\rm sec}} \pm \sigma_{\mathcal{B}(\rm stat.)} \pm \sigma_{\mathcal{B}(\rm syst.)}\,. \tag{6.11}$$

Table 6.19: *The systematic errors on the ratio $\mathcal{A}$, the number of $B\bar{B}$ events produced, and the secondary branching fractions. The errors that contribute to the corrected efficiency ϵ_c, are given in Table 5.6.*

	Fractional Error (%)
$\mathcal{A}$	7.0
$N_{B\bar{B}}$	1.6
$\mathcal{B}(D^- \to K^0\pi^-)$	6.5
$\mathcal{B}(\phi \to K^+K^-)$	1.4
$\mathcal{B}(K^0_S \to \pi^+\pi^-)$	0.4

Table 5.6 lists the efficiency correction factors i and their errors Δi, which contribute to $\Delta\epsilon_c$ as shown in Equation 6.9. Table 6.19 lists the fractional errors for $\mathcal{A}$, $N_{B\bar{B}}$, and the secondary branching fractions $\mathcal{B}(D^- \to K^0\pi^-)$, $\mathcal{B}(\phi \to K^+K^-)$, and $\mathcal{B}(K^0_S \to \pi^+\pi^-)$. Although the fractional error on the ratio $\mathcal{A}$ was calculated independently for each analysis, the values obtained were all approximately equal to 7.0 %.

Chapter 7

Summary and Conclusions

The studies of the decays $B^0 \to \phi K^0_S$ and $B^0 \to K^{*+}\pi^-$, for the measurement of CP violation parameters, were motivated in Chapter 2.

The mode $B^0 \to \phi K^0_S$ is a CP eigenstate that can be used to study time-dependent decay rate asymmetries between B^0 and $\bar{B}^0$ mesons [27]. This will allow a measurement of the CP violation parameter $\sin 2\beta$, which can be compared to that obtained using the Golden Mode for this measurement, $B^0 \to J/\psi K^0_S$. Although the mode $B^0 \to \phi K^0_S$ is a rare decay whose branching fraction is two orders of magnitude smaller than that of $B^0 \to J/\psi K^0_S$, an initial measurement of $\sin 2\beta$ with $B^0 \to \phi K^0_S$ should be possible with a few hundred fb^{-1} of $\Upsilon(4S)$ data.

The most important difference to note between the two CP eigenstates $B^0 \to \phi K^0_S$ and $B^0 \to J/\psi K^0_S$, is that the former decay can only be described by a gluonic penguin diagram [28, 29], while the latter is described by a tree level diagram. Any difference that may be found between the measurement of $\sin 2\beta$ using these two modes, may provide an insight into hidden internal processes of the penguin loop and lead to new physics [30, 31].

Recent measurements of B meson decays to $K\pi$ and $\pi\pi$ final states [34, 35, 36], have shown considerable contributions from penguin processes to $B \to K\pi$ decays. These

Table 7.1: *The summary of the final results of the branching fraction measurements for the decays* $B^0 \to \phi K^0$ *and* $B^0 \to K^{*+}\pi^-$, *and for the calibration mode* $B^0 \to D^-\pi^+$. *Also presented are the corrected signal efficiency* ϵ_c, *the signal yield* N_S, *the significance* σ, *and the product of the secondary branching fractions* $\mathcal{B}_{sec}$, *for each measurement. For each branching fraction, the first error is the statistical error and the second is the systematic error.*

Mode	ϵ_c (%)	N_S	σ	$\mathcal{B}_{\rm sec}$	$\mathcal{B}$
$B^0 \to D^-\pi^+$	23.0	179.0	11.3	0.01	$(3.59 \pm 0.29 \pm 0.35) \times 10^{-3}$
$B^0 \to \phi K^0$	30.4	10.7	4.9	0.17	$(9.3 \pm 3.4 \pm 1.1) \times 10^{-6}$
$B^0 \to K^{*+}\pi^-$	10.1	10.8	3.0	0.23	$(20.8 \pm 9.3 \pm 2.1) \times 10^{-6}$
					$< 38.9 \times 10^{-6}$ at 90 % CL

penguin contributions could increase the possibility of interference between the phases of penguin and tree level processes and lead to possible direct CP violation. The study of the decay $B^0 \to K^{*+}\pi^-$, may provide a measurement of direct CP violation as a result of interference between the phases of the penguin and tree level contributions to its final state.

The results of the branching fraction measurements for the decays $B^0 \to \phi K^0$ and $B^0 \to K^{*+}\pi^-$, and for the calibration mode $B^0 \to D^-\pi^+$, were presented in Chapter 6 and compared to other measurements. They are summarised in Table 7.1. For the calculation of the significance of the calibration mode $B^0 \to D^-\pi^+$, the variance on the large number of observed events in the signal region, $N_{\rm sig}$, was also taken into account, so that the combined variance is given by,

$$\text{variance} = 210 + 31 + 1.6^2 + 2.4^2 \,. \tag{7.1}$$

The measurement of the branching fraction for the calibration mode $\mathcal{B}(B^0 \to D^-\pi^+)$, is in good agreement with the world-average branching fraction for this mode, $\mathcal{B}_{\rm ave}(B^0 \to$

$D^-\pi^+) = (3.0 \pm 0.4(\text{total})) \times 10^{-3}$, which is presented by the Particle Data Group [17].

The measurement of $\mathcal{B}(B^0 \to \phi K^0)$ is consistent with the published measurement from the *BABAR* experiment using a maximum likelihood fit method with the same data, $\mathcal{B}(B^0 \to \phi K^0) = (8.1^{+3.1}_{-2.5}(\text{stat.}) \pm 0.8(\text{syst.})) \times 10^{-6}$ [58]. It is also consistent with the measurement presented by the Belle experiment, $\mathcal{B}(B^0 \to \phi K^0) = (8.9^{+3.4}_{-2.7}(\text{stat.}) \pm 1.0(\text{syst.})) \times 10^{-6}$ [60]. The CLEO experiment has reported a measurement of $\mathcal{B}(B^0 \to \phi K^0) = (5.4^{+3.7}_{-2.7}(\text{stat.}) \pm 0.7(\text{syst.})) \times 10^{-6}$, and an upper limit of $\mathcal{B}(B^0 \to \phi K^0) < 12.3 \times 10^{-6}$ at 90 % confidence limit [61].

The measurement of $\mathcal{B}(B^0 \to K^{*+}\pi^-)$ is consistent with the unpublished measurements from the CLEO experiment, $\mathcal{B}(B^0 \to K^{*+}\pi^-) = (23^{+9}_{-7}(\text{stat.}) \pm 3(\text{syst.})) \times 10^{-6}$, for the secondary decay $K^{*+} \to K^0_S\pi^+$ [50], and from the Belle experiment, $\mathcal{B}(B^0 \to K^{*+}\pi^-) = (26.0 \pm 8.3(\text{stat.}) \pm 3.5(\text{syst.})) \times 10^{-6}$ [62].

The CLEO experiment has recently presented a measurement of $\mathcal{B}(B^0 \to K^{*+}\pi^-) = (16^{+6}_{-5}(\text{stat.}) \pm 2(\text{syst.})) \times 10^{-6}$, for the secondary decays $K^{*+} \to K^0_S\pi^+$ and $K^{*+} \to K^+\pi^0$ [57]. As part of the Dalitz analysis that produced this measurement, the non-resonant final state $B^0 \to K^0_S\pi^+\pi^-$ was measured with a branching fraction of $\mathcal{B}(B^0 \to K^0\pi^+\pi^-) = (50^{+10}_{-9}(\text{stat.}) \pm 7(\text{syst.})) \times 10^{-6}$ [57]. The former is consistent with the measurement of $\mathcal{B}(B^0 \to K^{*+}\pi^-)$ presented here. The branching fraction of the non-resonant decay was used in background studies, to estimate the number of non-resonant events in the $\mathcal{B}(B^0 \to D^-\pi^+)$ and $\mathcal{B}(B^0 \to K^{*+}\pi^-)$ measurements presented here.

The range of theoretical predictions for the measurement of $\mathcal{B}(B^0 \to \phi K^0)$ is 0.3–18 ($\times 10^{-6}$), and for $\mathcal{B}(B^0 \to K^{*+}\pi^-)$ is 1–19 ($\times 10^{-6}$) [25]. The measurement of $\mathcal{B}(B^0 \to \phi K^0)$ presented here is within the theoretical range, and that of $\mathcal{B}(B^0 \to K^{*+}\pi^-)$ is close to the higher end of the predicted theoretical range. For the latter, a considerable difference between experimental results and theoretical predictions would be an interesting hint at new physics, possibly from contributions in the penguin loop.

The errors on the measurements of the branching fractions $\mathcal{B}(B^0 \to \phi K^0)$ and $\mathcal{B}(B^0 \to$

Table 7.2: *The results of searches for direct CP violation in the $B \to K\pi$ decays $B^0 \to K^+\pi^-$, $B^+ \to K^+\pi^0$, and $B^+ \to K^0\pi^+$ for $K^0 \to K^0_S$, from the BABAR [34, 64], CLEO [65], and Belle [66] experiments. The asymmetry a_f, is the difference between the number of events decaying to each of the charge conjugate final states, and is given by Equation 2.31, although the sign of the asymmetry is dependent on the convention used. Also given are the average branching fractions [17] for these modes.*

Mode	a_f (*BABAR*)	a_f (CLEO)	a_f (Belle)	$\mathcal{B}_{\rm ave}$
$B^0 \to K^+\pi^-$	$-0.07 \pm 0.08 \pm 0.02$	-0.04 ± 0.16	$0.044^{+0.186+0.018}_{-0.167-0.021}$	$(17.4 \pm 1.5) \times 10^{-6}$
$B^+ \to K^+\pi^0$	$0.00 \pm 0.18 \pm 0.04$	-0.29 ± 0.23	$-0.059^{+0.222+0.055}_{-0.196-0.017}$	$(12.1 \pm 1.6) \times 10^{-6}$
$B^+ \to K^0\pi^+$	$-0.21 \pm 0.18 \pm 0.03$	0.18 ± 0.24	$0.098^{+0.430+0.020}_{-0.343-0.063}$	$(17.3\ ^{+\ 2.7}_{-\ 2.4}) \times 10^{-6}$

$K^{*+}\pi^-$) are statistically limited. The systematic errors arise as a result of several factors. The estimation of the tracking and particle ID systematic errors, in addition to that on the number of $B\bar{B}$ meson pairs produced, were high in the first run data as a result of the relative level of unfamiliarity with the detector and the PEP-II machine environment. In addition, the estimation of the systematic errors on the ratio $\mathcal{A}$ for each mode, which were obtained from the background characterisations of the $m_{\rm ES}$ and ΔE distributions, were conservative due to the poor fits obtained as a result of the low event statistics in these rare decays.

The statistical and systematic errors of these measurements will be improved with more data and with more experience with the *BABAR* detector and PEP-II machine conditions, respectively. Currently, there is over 80 fb^{-1} of on-resonance data available for analysis from the *BABAR* experiment, which would improve the statistical error on the measurements presented here by approximately a factor of two.

Increased data will also allow searches for the mentioned CP violation effects in the decays $B^0 \to \phi K^0_S$ and $B^0 \to K^{*+}\pi^-$. An initial measurement of the CP violation

parameter $\sin 2\beta$ with the decay $B^0 \to \phi K^0_S$, using approximately 80 fb^{-1} of on-resonance data, was presented in July 2002 by the *BABAR* experiment, with the result $\sin 2\beta = -0.19^{+0.52}_{-0.50}(\text{stat.}) \pm 0.09(\text{syst.})$ [63]. This result is limited by the low statistics of the decay $B^0 \to \phi K^0_S$ and will improve in accuracy with more data. The latest result with the decay $B^0 \to J/\psi K^0_S$ is $\sin 2\beta = 0.741 \pm 0.067(\text{stat.}) \pm 0.033(\text{syst.})$ [19]. A significant difference between the measurements of $\sin 2\beta$ using these two decays, may signify new physics in the penguin loop of the single penguin contribution to $B^0 \to \phi K^0_S$.

Recent charge asymmetry searches in $B \to K\pi$ decays are consistent with the existence of no direct CP violation [34, 64, 65, 66]. Table 7.2 shows the results from the *BABAR*, CLEO, and Belle experiments. With more data, similar studies may be undertaken using the $B^0 \to K^{*+}\pi^-$ mode.

References

[1] B. Aubert *et al.* The *BABAR* Detector. *Nucl. Instrum. Meth.*, A479:1–116, 2002.

[2] S. Mori (ed.) *et al.* The Belle Detector. *Nucl. Instrum. Meth.*, A479:117–232, 2002.

[3] A. D. Sakharov. Violation of CP Invariance, C Asymmetry, and Baryon Asymmetry of the Universe. *Pisma Zh. Eksp. Teor. Fiz.*, 5:32–35, 1967.

[4] J. H. Christenson, J. W. Cronin, V. L. Fitch, and R. Turlay. Evidence for the 2π Decay of the K_2^0 Meson. *Phys. Rev. Lett.*, 13:138–140, 1964.

[5] B. Aubert *et al.* A Study of Time Dependent CP-Violating Asymmetries and Flavor Oscillations in Neutral B Decays at the $\Upsilon(4S)$. *hep-ex/0201020*, 2002.

[6] Ikaros I. Y. Bigi and A. I. Sanda. CP Violation. *Cambridge Monogr. Part. Phys. Nucl. Phys. Cosmol.*, 9:1–382, 2000.

[7] M. B. Gavela, P. Hernandez, J. Orloff, and O. Pene. Standard Model CP Violation and Baryon Asymmetry. *Mod. Phys. Lett.*, A9:795–810, 1994.

[8] Patrick Huet and Eric Sather. Electroweak Baryogenesis and Standard Model CP Violation. *Phys. Rev.*, D51:379–394, 1995.

[9] M. Kobayashi and T. Maskawa. CP Violation in the Renormalizable Theory of Weak Interaction. *Prog. Theor. Phys.*, 49:652–657, 1973.

[10] Andrzej J. Buras and Robert Fleischer. Quark Mixing, CP Violation and Rare Decays After the Top Quark Discovery. *Adv. Ser. Direct. High Energy Phys.*, 15:65–238, 1998.

[11] Lincoln Wolfenstein. Parametrization of the Kobayashi-Maskawa Matrix. *Phys. Rev. Lett.*, 51:1945, 1983.

[12] N. Cabibbo. Unitary Symmetry and Leptonic Decays. *Phys. Rev. Lett.*, 10:531–532, 1963.

[13] Ling-Lie Chau and Wai-Yee Keung. Comments on the Parametrization of the Kobayashi-Maskawa Matrix. *Phys. Rev. Lett.*, 53:1802, 1984.

[14] C. Jarlskog (ed.). CP Violation. Singapore, Singapore: World Scientific, 1989, 723p. (Advanced Series on Directions in High Energy Physics, 3).

[15] Paul F. Harrison (ed.) and Helen R. Quinn (ed.). The *BABAR* Physics Book: Physics at an Asymmetric B Factory. Papers from Workshops on Physics at an Asymmetric B Factory (*BABAR* Collaboration Meetings), Rome, Italy, 11-14 November 1996; Princeton, NJ, 17-20 March 1997; Orsay, France, 16-19 June 1997; and Pasadena, CA, 22-24 September 1997.

[16] Andrzej J. Buras, Markus E. Lautenbacher, and Gaby Ostermaier. Waiting for the Top Quark Mass, $K^+ \to \pi^+ \nu\bar{\nu}$, $B_s^0 - \bar{B}_s^0$ Mixing and CP Asymmetries in B Decays. *Phys. Rev.*, D50:3433–3446, 1994.

[17] K. Hagiwara *et al.* Review of Particle Physics. *Phys. Rev.*, D66, 010001, 2002.

[18] A. Lai *et al.* A Precise Measurement of the Direct CP Violation Parameter Re (ϵ'/ϵ). *Eur. Phys. J.*, C22:231–254, 2001.

[19] B. Aubert *et al.* Measurement of the CP-Violating Asymmetry Amplitude $\sin 2\beta$. *hep-ex/0207042*, 2002.

[20] K. Abe *et al.* Observation of Mixing-induced CP Violation in the Neutral B Meson System. *hep-ex/0202027*, 2002.

[21] C. Albajar *et al.* Search for $B^0 - \bar{B}^0$ Oscillations at the CERN $p\bar{p}$ Collider. (paper 2.). *Phys. Lett.*, B186:247, 1987.

[22] H. Albrecht *et al.* Observation of $B^0 - \bar{B}^0$ Mixing. *Phys. Lett.*, B192:245, 1987.

[23] B. Aubert *et al.* Measurement of the $B^0 - \bar{B}^0$ Oscillation Frequency with Inclusive Dilepton Events. *Phys. Rev. Lett.*, 88:221803, 2002.

[24] Quang Ho-Kim (ed.) and Xuan-Yem Pham (ed.). Elementary Particles and Their Interactions. Berlin, Germany: Springer-Verlag, 1998, 661p.

[25] Karen Lingel, Tomasz Skwarnicki, and James G. Smith. Penguin Decays of B Mesons. *Ann. Rev. Nucl. Part. Sci.*, 48:253, 1998.

[26] John R. Ellis, M. K. Gaillard, D. V. Nanopoulos, and S. Rudaz. The Phenomenology of the Next Left-handed Quarks. *Nucl. Phys.*, B131:285, 1977.

[27] Isard Dunietz and Jonathan L. Rosner. Time Dependent CP Violation Effects in $B^0 - \bar{B}^0$ Systems. *Phys. Rev.*, D34:1404, 1986.

[28] N. G. Deshpande and J. Trampetic. Penguin Mediated Exclusive Hadronic Weak B Decays. *Phys. Rev.*, D41:895, 1990.

[29] N. G. Deshpande and Xiao-Gang He. Gluonic Penguin B Decays in Standard and two Higgs Doublet Models. *Phys. Lett.*, B336:471–476, 1994.

[30] Yuval Grossman and Mihir P. Worah. CP Asymmetries in B Decays with New Physics in Decay Amplitudes. *Phys. Lett.*, B395:241–249, 1997.

[31] Robert Fleischer. CP Violation and the Role of Electroweak Penguins in Non-leptonic B Decays. *Int. J. Mod. Phys.*, A12:2459–2522, 1997.

[32] Myron Bander, D. Silverman, and A. Soni. CP Non-invariance in the Decays of Heavy Charged Quark Systems. *Phys. Rev. Lett.*, 43:242, 1979.

[33] Ahmed Ali, G. Kramer, and Cai-Dian Lu. CP-violating Asymmetries in Charmless Non-leptonic Decays $B \to PP$, PV, VV in the Factorization Approach. *Phys. Rev.*, D59:014005, 1999.

[34] B. Aubert *et al.* Measurement of Branching Fractions and Search for CP-violating Charge Asymmetries in Charmless Two-body B Decays into Pions and Kaons. *Phys. Rev. Lett.*, 87:151802, 2001.

[35] D. Cronin-Hennessy *et al.* Observation of $B \to K^{\pm}\pi^0$ and $B \to K^0\pi^0$, and Evidence for $B \to \pi^+\pi^-$. *Phys. Rev. Lett.*, 85:515–519, 2000.

[36] K. Abe *et al.* Measurement of Branching Fractions for $B \to \pi\pi$, $K\pi$ and KK Decays. *Phys. Rev. Lett.*, 87:101801, 2001.

[37] Stanford Linear Accelerator Center. PEP-II, an Asymmetric B Factory - Conceptual Design Report. Technical Report SLAC-418, Stanford Linear Accelerator Center, June 1993.

[38] J. Seeman *et al.* The PEP-II Storage Rings. *SLAC-PUB-8786, submitted to Nucl. Instr. Methods*, 2001.

[39] J. Seeman *et al.* Status Report on PEP-II Performance. In *Proceedings of the 7th European Particle Accelerator Conference*, Vienna, Austria, 2000. EPAC 2000.

[40] D. Boutigny *et al.* *BABAR* Technical Design Report. *SLAC-R-0457*, 1995.

[41] L. R. Dalesio *et al.* The Experimental Physics and Industrial Control System Architecture: Past, Present, and Future. *Nucl. Instrum. Meth.*, A352:179–184, 1994.

[42] A. S. Johnson. Java Analysis Studio. In *Proceedings of the International Conference on Computing in High Energy Physics*, Padova, Italy, 2000. CHEP 2000.

[43] R. Brun, F. Rademakers, and S. Panacek. ROOT, an Object-Oriented Data Analysis Framework. Prepared for CERN School of Computing (CSC 2000), Marathon, Greece, 17-30 September 2000.

[44] R. Brun, O. Couet, N. Cremel-Somon, and P. Zanarini. PAW: Physics Analysis Workstation: User's Guide. *CERN Program Library*, 1999. *CERN-Q-121.*

[45] D. J. Lange. The EvtGen Particle Decay Simulation Package. *Nucl. Instrum. Meth.*, A462:152–155, 2001.

[46] Torbjorn Sjostrand. Pythia 5.7 and Jetset 7.4: Physics and Manual. 1995. *CERN-TH-7112-93.*

[47] R. Brun, R. Hagelberg, M. Hansroul, and J. C. Lassalle. Geant: Simulation Program for Particle Physics Experiments. User Guide and Reference Manual. *CERN-DD-78-2-REV.*

[48] Pierre Billoir. Track Fitting with Multiple Scattering: A New Method. *Nucl. Instr. Meth.*, A225:352, 1984.

[49] B. Aubert *et al.* Direct CP Violation Searches in Charmless Hadronic B Meson Decays. *Phys. Rev.*, D65:051101, 2002.

[50] Yongsheng Gao and Frank Wurthwein. Charmless Hadronic B Decays at CLEO. *hep-ex/9904008*, 1999.

[51] D. M. Asner *et al.* Search for Exclusive Charmless Hadronic B Decays. *Phys. Rev.*, D53:1039–1050, 1996.

[52] K. Abe *et al.* Study of Three-body Charmless B Decays at Belle. *hep-ex/0107051*, 2001.

[53] A. Bozek. Charmless B Decays Involving Vector Mesons in Belle. *hep-ex/0104041*, 2001.

[54] G. Mancinelli and S. Spanier. Kaon Selection at the *BABAR* Experiment (`PidKaonSMSSelector`, `PidKaonMicroSelector`). 2001. Internal *BABAR* Analysis Document, BAD-116.

[55] H. Albrecht *et al.* Exclusive Hadronic Decays of B Mesons. *Z. Phys.*, C48:543–552, 1990.

[56] H. Albrecht *et al.* Search for $b \to s x^+ x^-$ in Exclusive Decays of B Mesons. *Phys. Lett.*, B262:148–154, 1991.

[57] E. Eckhart *et al.* Observation of $B \to K^0_s \pi^+ \pi^-$ and $B \to K^{*\pm} \pi^\mp$. *hep-ex/0206024*, 2002.

[58] B. Aubert *et al.* Measurement of the Decays $B \to \phi K$ and $B \to \phi K^*$. *Phys. Rev. Lett.*, 87:151801, 2001.

[59] R. J. Barlow. Statistics: A Guide to the Use of Statistical Methods in the Physical Sciences. Chichester, England: John Wiley & Sons Ltd., 1989, 204p.

[60] K. Abe *et al.* Observation of Charmless Decays $B \to \phi K$ and $B \to \phi K^*$ at Belle. *KEK-PREPRINT-2001-74.*

[61] R. A. Briere *et al.* Observation of $B \to \phi K$ and $B \to \phi K^*$. *Phys. Rev. Lett.*, 86:3718–3721, 2001.

[62] K. Abe *et al.* A Study of Charmless B Meson Decays to Pseudoscalar-Vector Final States at Belle. *KEK-PREPRINT-2001-76.*

[63] B. Aubert. Measurement of $\sin 2\beta$ in $B^0 \to \phi K^0_S$. *hep-ex/0207070*, 2002.

[64] B. Aubert *et al.* Study of CP-violating Asymmetries in $B^0 \to \pi^+\pi^-$, $K^+\pi^-$ Decays. *Phys. Rev.*, D65:051502, 2002.

[65] S. Chen *et al.* Measurement of Charge Asymmetries in Charmless Hadronic B Meson Decays. *Phys. Rev. Lett.*, 85:525–529, 2000.

[66] K. Abe *et al.* Search for Direct CP Violation in $B \to K\pi$ Decays. *Phys. Rev.*, D64:071101, 2001.